Copyright

by

Nanzhu Zhao

2017

**The Dissertation Committee for Nanzhu Zhao Certifies that this is the approved version of the following dissertation:**

# MICRO SELECTIVE LASER SINTERING OF SILICON CARBIDE

**Committee:**

Joseph J. Beaman, Supervisor

David L. Bourell

Scott Fish

Desiderio Kovar

Joseph H. Koo

# MICRO SELECTIVE LASER SINTERING OF SILICON CARBIDE

**by**

**Nanzhu Zhao**

**Dissertation**

Presented to the Faculty of the Graduate School of

The University of Texas at Austin

in Partial Fulfillment

of the Requirements

for the Degree of

**DOCTOR OF PHILOSOPHY**

**The University of Texas at Austin**

**December 2017**

# Acknowledgements

This work is based upon work supported primarily by the National Science Foundation under Cooperative Agreement No. EEC-1160494.

I wish to extend gratitude towards my advisor, Professor Joseph J. Beaman for his unwavering support, thoughtful guidance and valuable criticisms along the course of this research. I am indebted to Prof. Beaman for introducing me to the world of additive manufacturing, for guiding me to approach research with maturity and for providing me freedom to explore new ideas and solutions. It was a great privilege working with him.

I am extremely thankful to my committee members, Prof. Bourell, Prof. Kovar, Prof. Fish, and Prof. Koo, for providing crucial feedback.

Many thanks to the NASCENT Center, Dr. S.V. Sreenivasan, Dr. Roger Bonnecaze, and other professors and colleagues for their valuable advice and generous support.

I would like to thank my parents for their consistent support and encouragement throughout my college life. I am sincerely grateful for all their sacrifices for me.

Finally, a person who makes my work, and everything else, an enjoyable experience; my wife Yingxue. It is to her that I dedicate this dissertation.

# MICRON SELECTIVE LASER SINTERING OF SILICON CARBIDE

Nanzhu Zhao, Ph.D.

The University of Texas at Austin, 2017

Supervisor: Joseph J. Beaman

Silicon carbide (SiC) is of high importance in modern industry due to its superior properties including low bulk density, high hardness, high thermal conductivity, and excellent thermal shock and corrosion resistance. However, the strong Si – C covalent bond, lack of liquid phase, and low self-diffusivity of SiC make it very difficult for the production of fully dense parts without sintering aids or external pressure. These difficulties can be bypassed with the implementation of selective laser sintering, which enables the generation of complex-shape, high-resolution SiC parts with structural integrity. Current sintering process normally involves a powder mixture of silicon carbide as a structural material and polymer as a binder material for the generation of the preforms. It is then further sintered in high-temperature furnace to achieve full densification. In general, liquid silicon infiltration process is accompanied during the furnace sintering in order to minimize porosity and thus, maintain structural stability and enhance material

properties. However, excessive infiltration may lead to overfill of the structure, deteriorating the surface and small features.

The goal of the proposed research is to apply selective laser sintering technology to achieve additive manufacturing of SiC parts with micro scale resolution. The proposed work is focused on the development of a micro SLS system as well as the investigation of different methods for the freeform fabrication of SiC. More specifically, the objectives of this research are threefold. Firstly, a simulation model is developed to analyze the interaction between laser radiation and micron-sized powders. Ideal system and processing parameters are estimated from the model and analyzed with experimental results. Secondly, the design of a new micro selective laser sintering system that is capable of micro scale featuring resolution is proposed. Improvements in laser scanning system and powder coating and compaction processes are studied. Finally, a material-specific micro SLS process is developed for the generation of SiC parts with complex geometry, micro scale resolution, and structural integrity. Different binding mechanisms and sintering additives are studied to facilitate the process and enhance the porosity control.

# Table of Contents

# List of Tables

# List of Figures

# Chapter 1: Introduction

## 1.1 Silicon Carbide

Silicon carbide (SiC) has become a more and more important material during the last decade for high-temperature, high-frequency, and high-power device applications due to its superior mechanical, electrical, and chemical properties. For conventional applications, SiC shows low density (2 – 2.5 times less), high elastic modulus (1.5 – 2.5 times more), and low thermal expansion (3 – 4 times less) compared to stainless steel. For electrical applications, SiC also exhibits high operation temperature (2 – 3 times), high thermal conductivity (6 – 8 times), high breakdown electric field (4 – 20 times), wide bandgap (2 – 2.5 times), and high saturated electron drift velocity (2 – 3 times) compared to the most commonly used semiconductor materials such as silicon and gallium arsenide. At present, these favorable properties of SiC have made it an ideal material for micro- and nanoelectromechanical system (MEMS and NEMS) applications in aerospace, automotive, and semiconductor industries [1-3].

### 1.1.1 Properties of Silicon Carbide

SiC exists in around 250 crystalline structures with several stable crystal structures [4]. The most common types are 3C, 4H, 6H, 15R and 9T. The cubic 3C is commonly called β-SiC with a zincblended structure formed at temperatures below 1700 °C while others are generally referred to as α-SiC, which is the most widely occurred polymorph

with hexagonal crystal structure formed at temperatures higher than 1700 °C. Figure 1 illustrates the structural difference between these two major SiC phases [5]. Phase transformation from β-SiC to α-SiC is possible via extensive heating above 2000 °C. Boron doped β-SiC can transform to 4H polytype α-SiC at lower temperature while nitrogen doped β-SiC can stabilize the transformation to 6H polytype α-SiC without the formation of 4H polytype. This transformation is reversible under pure nitrogen atmosphere and form stable β-SiC phase up to 2500 °C by applying nitrogen pressure. SiC does not melt under atmospheric pressure but sublimes and dissociates into silicon and carbon [6-8].

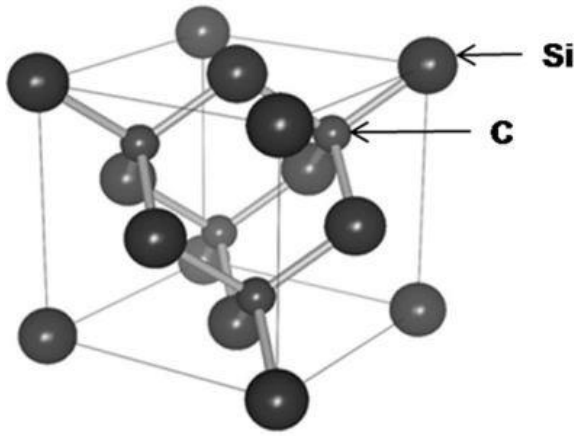


Figure 1.1. Chemical structure of β-SiC.

Pure SiC is colorless but the dark gray, brown, or black color of commercial SiC is from impurities such as iron. The theoretical density of pure β-SiC is 3.210 g/cm$^3$ and that of pure α-SiC is 3.208 g/cm$^3$, which is one of the light-weight covalently bonded ceramics. Experimental measurements reported the density of SiC in the range of from 3.166 to 3.249

g/cm$^3$ depending on the polytype [7]. SiC possesses high hardness (HV10 > 2200 GPa), high Young's modulus (> 400 GPa), high thermal conductivity (120 – 200 W/mK), very low thermal expansion (3.6 – 4.1 x $10^{-6}$/K at 20 to 400 °C), high thermal stability, high resistance to corrosion, abrasion and erosion, and also toxicologically safe [8]. SiC is resistant to any acids or alkalis or molten salts up to 800 °C. In air, SiC forms a protective silicon oxide film at 1200 °C and is capable of being used up to 1600 °C. The high thermal conductivity coupled with low thermal expansion and high strength make this material excellent thermal shock resistance. Table 1.1 listed some of the properties of α-SiC compared to the most commonly used materials: aluminum 6061 and stainless steel 316. Similar to all other ceramics, SiC is brittle. However, many efforts have been made to produce fiber-reinforced SiC composites that have shown promising impact strength for wide applications.

Table 1.1 Comparison of material properties

| **Material** | **Density (kg/m3)** | **Tensile Modulus (GPa)** | **Flexural Strength (MPa)** | **Melting Temp. (°C)** | **Thermal Cond. (W/m·K)** | **Linear Thermal Expansion Coefficient (10-6 K-1)** |
|---|---|---|---|---|---|---|
| **α-SiC** | 3.1 | >400 | 550 | 2830 | 120 | 2.77 |
| **Al 6061** | 2.7 | 65 – 70 | 240 | 550 – 650 | 150 – 210 | 23.1 |
| **Stainless Steel 316** | 8.0 | 193 | >750 | 1400 | 16.3 | 15 – 18 |

The optical absorption of SiC can be characterized by intraband and interband absorption components. There have been numerous attempts by researchers to measure the optical absorption bands for different types of SiC. The absorption coefficient of SiC was reported to range from 10 – 5.5 × $10^4$ $cm^{-1}$ in the energy range between 2.42 and 4.4 eV. The bandgap of β-SiC is in the range of from 2.13 to 2.32 eV. The transmission and reflectance rate of β-SiC as a function of wavelength are shown in Figure 1.2. It can be observed that β-SiC becomes almost transparent to the light with wavelength of above 500 nm [9-12].

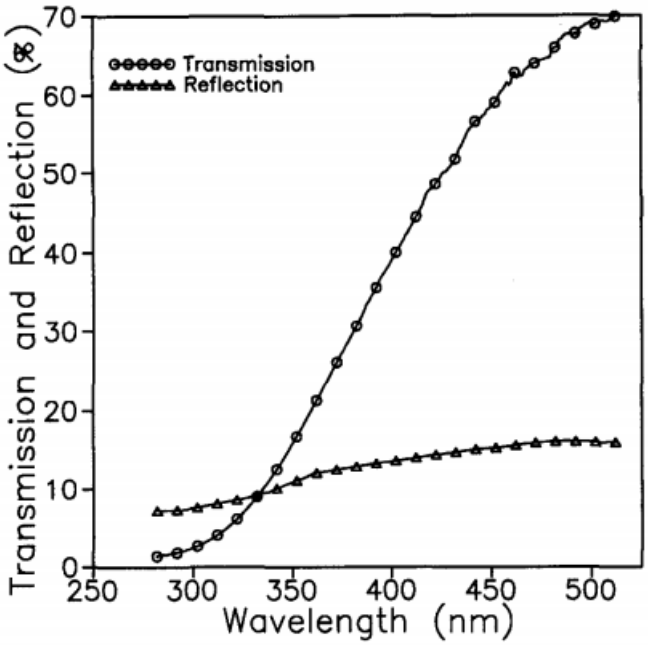


Figure 1.2. Transmission and reflection rate of β-SiC film.

### 1.1.2 Chemistry of Silicon Carbide Formation

SiC can be produced from a mixture of $SiO_2$ and some form of carbon low in ash. The chemical reaction can be expressed as [5-8]:

$$SiO_2 + 3C = SiC + 2CO \quad (1.1)$$

β-SiC is synthesized through the gaseous intermediate SiO with the following series of reactions being the most important:

$$SiO_2 + C = SiO + CO \quad (1.2)$$

$$SiO_2 + CO = SiO + CO_2 \quad (1.3)$$

$$SiO_2 + CO = SiO + CO_2 \quad (1.4)$$

$$C + CO_2 = 2CO \quad (1.5)$$

$$2C + SiO = SiC + CO \quad (1.6)$$

SiO is initially formed at the contact points of the carbon and $SiO_2$ according to the reaction in equation (1.2). But high portion of SiO indicates that the gas/solid mechanism through the reactions in equations (1.3) and (1.4) is the one, which render the reaction in equation (1.5) possible once the C and $SiO_2$ contact points are consumed. The starting carbon source has a substantial influence on the product SiC morphology and the rate of the reaction: finer carbon crystallites react faster than larger ones. $SiO_2$ crystallite size has little effect on the reaction rate. SiC can be sintered with several crystallographic

orientations: low temperature leads to the formation of beta-silicon, with a cubic crystal structure while higher temperature result in one or more hexagonal structures. These modifications, which differ only by the position of the atomic layers, are referred as α-SiC.

The fabrication of SiC with specified shape was in the form of Si-SiC composite made by the reaction-sintering or reaction-bonding process. During the process, SiC powders are mixed with carbon in various forms and the mixture heated in contact with molten silicon. The term reaction sintering is from the reaction between carbon and silicon to form SiC. The carbon used in the process in converted into the new SiC bonds to the original particles [13]. Ruff concluded that this reaction begins above 1500 ºC and under the condition of his experiment, is complete at 1800 ºC [14]. Recently, numerous experiments have been conducted involving a different reaction:

$$\mathrm{Si} + \mathrm{C} = \mathrm{SiC} \tag{1.7}$$

When using pure silicon and carbon to form SiC based on the equation above, SiC cannot be formed until the melting point of silicon (1430 ºC) is reached. The reaction temperature can be as low as 1000 ºC if using nickel-silicon or aluminum-silicon alloys instead of pure silicon. Taylor and Laidlor reported the formation of SiC at 1150 ºC when some alloying agent reduces the liquefying point of silicon below 1400 ºC [7,8]. Antipin and Ivanson reported beta-SiC can be obtained from the electrolytic production of a silicon-aluminum alloy liquid at 1000 ºC in graphite crucibles [17].

## 1.2 Sintering of Silicon Carbide

Similar to most materials in which the atomic bonding is predominantly covalent, SiC is considered to be unsinterable in the absence of additives [16,17]. The conventional fabrication of ceramics commonly includes a heat treatment process called sintering, during which the powder material is bonded and formed into a desired shape and then, is converted into a dense solid. There are four categories applicable for sintering of SiC: (1) solid-state sintering; (2) liquid-phase sintering; (3) vitrification; (4) viscous sintering. In some cases where high density and fine grain size are required, a process called pressure sintering can achieve full densification by applying external pressure during heating.

### 1.2.1 Solid State Sintering

In solid state sintering, the pre-shaped body is heated to a temperature that is typically 0.5 – 0.9 of the melting temperature of the ceramic material. No liquid phase exists during the process and atomic diffusion in the solid state leads to joining of the particles and reduction of the porosity. Coble identified three stages occurring sequentially during solid state sintering [18]. The initial stage is characterized by neck growth among particles as well as shrinkage of several percent. Due to densification mechanisms being dominant, no grain growth occurs during this stage. In intermediate stage, grain starts to grow and the pore surfaces are intersected by grain boundaries. The pore phase continues to shrink until the end of the intermediate stage. During the final stage, discontinued grain growth moves the grain boundaries away from the pores and thus, further enhance the grain

boundary diffusion [19-21]. Numerous models have been introduced to understand these mechanisms during solid state sintering, including the neck growth, surface and grain boundary diffusion, pore phase, transport mechanism, etc. [22-27].

### 1.2.2 Liquid Phase Sintering

In liquid phase sintering, only a few volume percent of the powder mixture is converted into liquid at the specified sintering temperature. Then, the liquid flows and fills the pores under the influence of capillary forces. Even though the liquid volume is insufficient to fill all the pore space to achieve full densification, it can enhance the rate of interparticle bonding during sintering. Consequently, significant improvements are usually accompanied with liquid phase sintering, which include increased densification rate, accelerated grain growth, or producing specific grain boundary properties. The distribution of the liquid and the resulting heterophases after densification plays a crucial role to the properties of the sintered body. However, due to extremely small amount of liquid volume, it is very difficult to precisely control the proper composition of the liquid during sintering [28-31].

Vitrification sintering is similar to liquid phase sintering. In this process, a relatively larger volume of liquid, typically more than 25% of the volume is formed, which is sufficient to fill the pore space for complete densification. Crystallization or vitrification of the liquid upon cooling can be expected. For viscous sintering, when ceramic particles

are heated near to, or above its softening temperature, viscous flow by surface tension leads to densification of the powders [5].

### 1.2.3 Sintering Additives

Densification of SiC without hot pressing cannot be achieved in the absence of sintering aids [32]. Sintering additives such as boron, aluminum, carbon, etc. are commonly used in the amounts of a few tenths of a percent. Boron and carbon additives are known to promote sintering by a solid state process. SiC powders doped with boron and carbon show considerable shrinkage in the early stages, suggesting that the densification occurs by grain boundary diffusion. Boron is known to activate the sintering process by facilitating the formation of a liquid phase of Si-B-C system eliminating porosity among particles. Doping with boron without carbon yields a fine microstructure with small shrinkage. [17,34]. Using carbon without boron does not lead to densification of SiC and it normally undergoes a large scale of coarsening. However, the role of carbon is to obstruct the mass transport processes and prevent massive grain growth of SiC during sintering [33]. Also, the presence of excessive carbon can prevent oxidation of SiC by removing the native $SiO_2$ layer during sintering, which can dramatically increase the self-diffusion rate. Carbon can also react with any excessive silicon present or formed during sintering, which subsequently yields densification of SiC [35,36]. Aluminum and boron both act as acceptors in SiC. Aluminum may inhibit matter transport along the boundary. In addition, aluminum is known to promote the transition from β-SiC to α-SiC, stabilizing the 4H

polytype and enhancing basal growth. This indicates that aluminum may promote the evolution of a more homogeneous microstructure than that of SiC sintered with boron and carbon only. Also, if aluminum is combined with boron and carbon, it can restrict excessive grain growth of α-SiC, lower the sintering temperature, and increase the final density of the sintered part.

Metal oxides such as yttrium and aluminum oxides have also been successfully used as additives for SiC sintering. Their presence is assumed to be mainly promoting liquid phase sintering. Therefore, liquid phase sintering of SiC can further reduce the sintering temperature by the use of metal oxides and the most promising additives are $Al_2O_3$, $Y_2O_3$, and MgO, which can accelerate the formation of melt and sintering without reacting with SiC. Long sintering time of typically a few hours allows the diffustion of Y, Al, and Mg from the oxide melt into SiC grains. These metal oxides are known to have no effect to the thickness of the boundary layer on the grains. Under the surface tension and capillary force, the formed liquid spreads over the surface, wetting and filling the pores among SiC particles. Consequently, the microstructure of liquid-phase sintered SiC part usually consists of SiC grains bonded by oxide phase.

Various combinations of these sintering additives such as silicon, boron, carbon, aluminum, metal oxides, etc. have been tested and compared by numerous researchers for the purpose of producing near full-density SiC parts and Table 1.2 shows a list of commonly used sintering additives, sintering methods and conditions, and resulting

densities. Note that some processes require hot-press sintering mainly due to lack of liquid phase [32-50].

Table 1.2 List of common sintering additives and resulting densities

| Sintering Additives | Added Amount | Sintering Conditions | Achieved Density |
|---|---|---|---|
| Si | **25 vol.%** | **Hot Press, 1900 °C, 30 MPa, 30 minutes** | **99%** |
| $Al_4SiC_4$ | **10 wt.%** | **Hot Press, 1700 °C, 60 Mpa, 2 hours** | **99%** |
| B-C | **0.9 wt.%** | **Presureless, 2100 °C** | **96%** |
| $B_4C$-C | **1.5wt.%** | **Pressureless, 1950°C, 15 minutes** | **99%** |
| $Al_2O_3$-$Y_2O_3$ | **10 wt.%** | **Pressureless, 1950 °C, 1 hour** | **97%** |
| $Al_2O_3$-$Y_2O_3$ | **10 wt.%** | **Pressureless, 2100 °C, 30 minutes** | **99%** |
| $Al_2O_3$-$Y_2O_3$ | **10 wt.%** | **Hot Press, 1800 °C, 20 MPa, 2 hours** | **94%** |
| $ZrB_2$-$Al_2O_3$-$Y_2O_3$ | **15 wt.%** | **Pressureless, 1950 °C, 15 minutes** | **98.3%** |
| Al-B-C | **8 wt.%** | **Hot Press, 1750 °C, 50 MPa, 30 minutes** | **98%** |
| $Al_4C_3$-$B_4C$-C | **2.7 wt.%** | **Pressureless, 2000 °C, 30 minutes** | **99%** |
| $Al_2O_3$-$Y_2O_3$-CaO | **10 wt.%** | **Hot Press, 1800 °C, 25 MPa, 1 hour** | **97%** |
| $Al_2O_3$-$Y_2O_3$-MgO | **12 wt.%** | **Hot Press, 1750 °C, 30 MPa, 3 hours** | **98%** |
| $Al_2O_3$-$Y_2O_3$-MgO | **9 wt. %** | **Hot Press, 1800 °C, 25 MPa, 30 minutes** | **98%** |
| $Al_2O_3$-$Y_2O_3$-MgO | **10 wt. %** | **Pressureless, 1930 °C, 1 hour** | **98.4%** |

### 1.2.4 Reaction Sintering

Reaction sintering is another type of sintering process where new phases or crystals are formed during heating. Many ceramic sintering processes involve a certain degree of reaction. Sacks developed a transient viscous sintering process for SiC, which involves rapid viscous densification of powders due to viscous flow of the amorphous $SiO_2$ layer on the particles. A subsequent reaction produces fully densified mullites ($Al_6Si_2O_{13}$) – SiC composite [51]. As mentioned above, SiC can also be formed from the reaction between pure silicon and carbon as low as at the melting temperature of silicon at 1430 °C. Liquid silicon is driven by capillary force into pores of the solid carbon matrix, and then reacts with the pore walls to form SiC. [52-54]. This process has also been used to produce reaction bonded silicon carbide (RBSiC), where liquid silicon rises to wet and fill the pores while reacting with carbonized binders to form additional β-SiC [55].

## 1.3 SELECTIVE LASER SINTERING

Selective laser sintering (SLS) is an additive manufacturing technique that uses laser to selectively sinter powder materials layer by layer to create a solid, three-dimensional structure. It was developed and patented by Dr. Joseph Beaman and Dr. Carl Deckard at the University of Texas at Austin in 1980s [56-58]. SLS technology has been widely used in industry because of its capability to produce 3D complex-structure parts directly from the CAD model. In addition, compared to other additive manufacturing techniques, such as stereolithography (SLA) and fused deposition modeling (FDM), SLS process does not require supporting materials because the sintered part is surrounded and supported by unsintered powder at all times, which allows the construction of more

complex 3D structures. SLS process is capable of producing parts made from a wide variety of materials, including polymers, glasses, ceramics, and metals for rapid prototyping, and even rapid manufacturing of final products.

Many efforts have been made to produce 3D SiC parts using SLS process during the past decade. Nelson et al. used polymer-coated SiC powder to produce 3D "green" shapes, which can be post-processed into SiC composites [59]. It allows the creation of complex geometries of SiC parts, which have been very difficult, or sometimes impossible with conventional machining. Evans et al. also used indirect SLS methods to create SiC preforms from a powder mixture of SiC as structural material and thermosetting polymers as binder material. These parts can be further processed at elevated temperature to carbonize the polymer binders followed by reactive infiltration of silicon to yield near-net shape parts [60,61]. Stevinson et al. also introduced the application of transient binders to infiltrate SLS-process polymer-SiC preforms in order to prevent shrinkage and collapse of the structure between softening and cross-linking of the initial polymer binders. This allows for support-free infiltration of SiC preforms with minimal deformation and shrinkage of the parts during the furnace sintering [62,63]. In terms of improving feature resolution, Regenfuss and Exner introduced laser micro sintering (LMS) in 2002, which is a modification of SLS process, has been successfully employed to create metallic micro parts. It involves the application of high-frequency pulsed laser, new powder and slurry coating system, and the proprietary CAD software [64,65]. This technology has also been used to process non-metal materials, including oxide and non-oxide ceramics [66-71].

### 1.3.1 Powder Flowability and Compactability

In the SLS process, a powder spreading roller or a coating bladed is commonly used to spread a thin layer of powder onto the center probe or the preceding layer. The resolution of the final part in vertical direction is consequently determined by the powder layer thickness. Powder spreading system requires powder with good flowability to form a thin, uniformly distributed layer. It has been proved in some applications that improvement of the flowability leads to the sintered parts with both cellular and fully dense structures by SLM [86]. Material properties that affect the powder flowability include the particle surface condition, particle size and morphology, range of particle size, and van der Waals force. Various methods have been developed to measure the flowability of powder material, including angle of repose, Carr's index, and Hausner ratio. Each method is targeted at a specific process or application. Powders with nearly uniform particle size normally exhibit very poor packing densities of only about 20% of the bulk material density. Powders with larger particle size of 50 – 100 μm offer packing densities of around 50% of the bulk density. The packing density is also dependent upon the distribution of particle sizes as well as the shapes of the particles in the powder. Therefore, a material-specific powder coating and compaction system is needed for the delivery of fine powder layers with micro scale layer thickness.

## 1.4 Research Objectives and Methodology

Overall, the goal of the proposed research is to apply selective laser sintering technology to achieve freeform fabrication of complex-shape, high-resolution SiC parts with structural integrity. This research also seeks to investigate the feasibility and potential applications of the new micro SLS system for the generation of high-precision polymer, metallic, and ceramic parts. More specifically, the objectives of this research are threefold:

1. Development of a preliminary 3D simulation model is proposed to understand the interaction between laser radiation and the powder bed during the SLS process. Processing parameters such as laser spot size and layer thickness will be estimated based on the simulation results.
2. Design of a micro SLS system that is capable of micro scale featuring is proposed. Some of the proposed design changes include high-frequency pulsed laser with micro scale beam spot size, synchronized laser-scanning system, powder/slurry-compatible coating and compaction system, etc.
3. Development of material-specific, cost-effective processes for the micro SLS of SiC for the generation of complex-shape, micro scale resolution SiC parts while maintaining structural integrity. Application of polymer and metallic binder materials and impregnation and infiltration of different transient binders are proposed.

# Chapter 2: Modeling of Micro SLS Process

This chapter describes the development of a simulation model to better understand the micro SLS process in a microscopic scale. It is based on the Monte Carlo algorithm associated with particle dynamics, ray-tracing method, and inter-particle heat conduction. This model provides preliminary evaluation of the sintering process such as laser penetration depth and heat-affected zone in all three directions. System parameters such as laser power, repetition rate, wavelength, packing density, and scan speed can be optimized accordingly.

## 2.1 Simulation Approach

In order to develop a comprehensive model for the thermal interaction among particles, all three heat transfer modes, including conduction, convection, and radiation were compared in terms of their significance.

### 2.1.1 Conduction and Convection

Conduction heat transfer is apparent as the particles are in contact and the high temperature difference between laser-heated particles and non-heated ones will drive the heat conduction among them. With regard to free convection among the particles, the micro SLS process is commonly conducted in high vacuum environment in order to prevent oxidation of the particles and thus, no free air convection would occur. Even if inert gas or processing gas is used during the sintering process, the heat transfer by convection is more

than one order of magnitude less than the heat transfer by conduction with the given particle sizes and the time scale. For instance, the thermal conductivity **K** of SiC is 120 $W \cdot K^{-1} \cdot m^{-1}$ and the maximum convection coefficient **h** of free-convection gas is about 2 $W \cdot K^{-1} \cdot m^{-2}$. Assuming a SiC particle with the diameter of 10 μm, contact distance of 10 μm, and the contact area assumed to be as small as one thousandth of the surface area, the ratio of heat transfer rate between conduction and convection is:

$$\frac{\frac{\partial Q_{conv}}{\partial t}}{\frac{\partial Q_{cond}}{\partial t}} = \frac{hA_s}{\frac{KA_c}{d}} = \frac{hA_s}{\frac{KA_s}{10^3 d}} \approx 10^{-4} \tag{2.1}$$

Note that even if the convection rate is calculated using the highest possible parameters expected to be used only during boiling or condensation, this ratio is still less than $10^{-2}$. Therefore, the free-convection heat transfer is negligible compared to the heat transfer by conduction.

### 2.1.2 Radiation Heat Transfer

Due to extremely high laser power intensity and the high melting temperature of ceramic materials, the radiation heat transfer among particles also needs to be considered and compared with conduction for its relative significance. As a comparison between the radiation and conduction with the average emissivity **ε** = 0.6 for silicon [83], and the Stefan-Boltzmann constant **σ** =5.67 x $10^{-8}$ $W \cdot K^{-4} \cdot m^{-2}$ for radiative heat transfer, and under the same assumption of very small contact area of one thousandth of the surface area, the ratio of heat transfer rate can be estimated as follows.

$$\frac{\frac{\partial Q_{rad}}{\partial t}}{\frac{\partial Q_{cond}}{\partial t}} = \frac{\varepsilon\sigma A_s(T_o^4 - T_e^4)}{\frac{KA_c}{d}(T_o - T_e)} = \frac{\varepsilon\sigma A_s(T_o^4 - T_e^4)}{\frac{KA_s}{10^3 d}(T_o - T_e)} \approx 10^{-2} \quad (2.2)$$

where the laser-heated particle temperature $T_o$ is assumed to reach the melting point of silicon (1700 K) and non-heated particle is at room temperature ($T_e \approx 300$ K). It indicates that heat conduction is about two magnitudes greater than the rate of radiation heat transfer. Therefore, heat transfer by convection and radiation is almost negligible compared to the rate of heat transfer by conduction, and thus was eliminated from the thermal model.

## 2.2 THERMAL MODEL

In order to select a proper model for the micron-sized powders, the Biot number can be used as a simple index of the ratio of the heat transfer resistance inside and at the surface of a body. A thermal body with very small Biot numbers (< 0.1) can be understood as the heat conduction inside the body being much faster than the heat convection away from the surface and thus, the temperature gradient inside the body is negligible. For a spherical silicon particle with the diameter of 10 μm, the Biot number can be calculated as follows.

$$Bi = \frac{hL_c}{K} \ll 0.1 \quad (2.3)$$

where **h** is the convective heat transfer coefficient, $\mathbf{L_c}$ is the characteristic length defined as the ratio of the volume to the surface area of the body, and **K** is the thermal

conductivity of the body. Therefore, it is reasonable to model each particle as a lumped-capacitance model, where the temperature field is uniform throughout the particle. The heat equation of the particle **i** with absorbed laser power of $P_{laser}$ is:

$$\sum_{j=1}^{N} KA_{ij} \frac{T_j - T_i}{\|r_i - r_j\|} + P_{laser} = m_i C_i \frac{dT_i}{dt} \tag{2.4}$$

where $A_{ij}$ represents the contact area between particles **i** and **j**, $A_{ij}$ represents the radiation heat transfer area between particles **i** and **j**, $m_i$ is the mass of particle **i**, and $C_i$ is the heat capacitance. For Hertzian's fully elastic model as shown in Figure 2.1, the contact area between two spherical particles $A_{ij}$ can be expressed as:

$$A_{ij} = \pi a^2 = \pi \left[\frac{3F_{con}R}{4E'}\right]^{\frac{2}{3}} \tag{2.5}$$

where $F_{con}$ is the static contact force between the two particles, $E'$ and R are the combined Young's modulus and radius of curvature of the two materials with the expression as follows:

$$E' = \left(\frac{1-\nu_i^2}{E_i} + \frac{1-\nu_j^2}{E_j}\right)^{-1} \text{ and } R = \left(\frac{1}{R_i} + \frac{1}{R_j}\right)^{-1} \tag{2.6}$$

where $\boldsymbol{\nu_i}$ and $\boldsymbol{\nu_j}$ are the Poisson's ratio of the material. The contact force between two particles were calculated after all particles were in rest and formed a powder bed. It is

different to the dynamic contact force modeled during the particle dynamics. If the mechanical properties of powders are uniform, $E'$ can be simplified to:

$$E' = \frac{E}{2(1-\nu^2)} \tag{2.7}$$

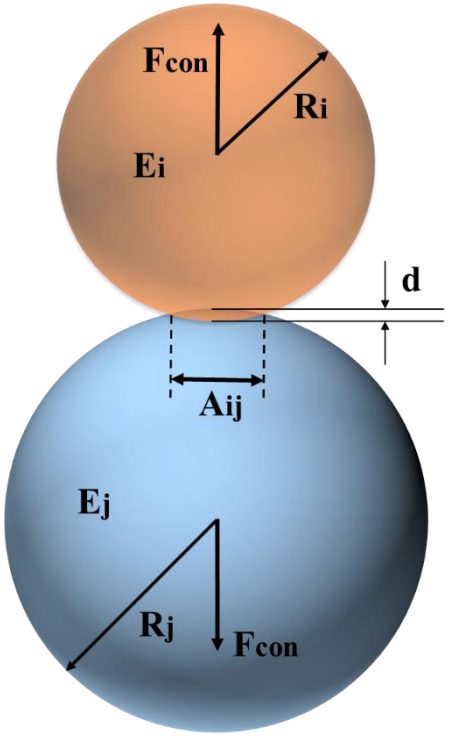


Figure 2.1. Contact of two fully elastic spheres.

## 2.3 PARTICLE DYNAMICS

Powder layer deposition process was modeled based on particle dynamics. In the 3D model, each particle is dropped into a predefined, constrained volume one by one. The equation of motion of the i-th particle can be expressed as follows:

$$m_i \ddot{\vec{r}}_i = \vec{F}_{con} + \vec{F}_{fric} + \vec{F}_{damp} + \vec{F}_{grav} \tag{2.8}$$

where $m_i$ is the mass, $r_i$ is the position of the i-th particle. According to the Hertzian contact theory, the contact force $\vec{F}_{con}$ is

$$F_{con} = \frac{4}{3} E' R^{\frac{1}{2}} d^{\frac{3}{2}} \tag{2.9}$$

where d is the displacement of the two particles in contact. Note that this contact force is different to the above-mentioned static contact force and the purpose of this dynamic contact force is merely to provide the compelling force between particles before the particles are in rest. The static contact forces among particles can be obtained after all particles are in rest. The contact force between particles and the walls was obtained by the contact displacement between a sphere and a plane surface with the modulus of elasticity of the wall much greater than that of powders. Therefore, the contact force on the i-th particle is equal to the vector sum of all the contact forces acting on it from overlapped particles and the walls.

The friction force $\vec{F}_{fric}$ was assumed to be a continuous sliding model as:

$$F_{fric} = \mu \left\| \vec{F}_{con} \right\| \vec{t}_{ij} \tag{2.10}$$

where $\mathbf{t_{ij}}$ is the unit tangential vector between the two particles **i** and **j**, given by

$$\vec{t}_{ij} = \frac{\vec{v}_{tj} - \vec{v}_{ti}}{\left\| v_{ti} - v_{tj} \right\|} \tag{2.11}$$

$\mathbf{v_t}$ is the tangential velocity:

$$\vec{v}_t = \vec{v} - (\vec{v} \cdot \vec{n})\vec{n} \tag{2.12}$$

The friction between particles and the walls was modeled the same way except that the velocity of the wall is always equal to zero. The damping force $F_{damp}$ was added into the model as the damping force by air. A simple model for this force is

$$\vec{F}_{damp} = -\mu_d \vec{v}_1 \tag{2.13}$$

Gravitational force only exists in vertical direction and is given by

$$F_{grav} = -m_i g r_z \tag{2.14}$$

During the simulation of powder deposition, one spherical particle with random diameter ranging from 1 to 10 μm was generated at random X/Y position but the Z position of slightly higher than the height of the volume. The motion of the particle was governed by the above-mentioned particle dynamics. As shown in Figure 2.2, the velocity of the particle was tracked in all three directions and was considered to be in rest when all the three values were less than 0.01 μm for 10 seconds.

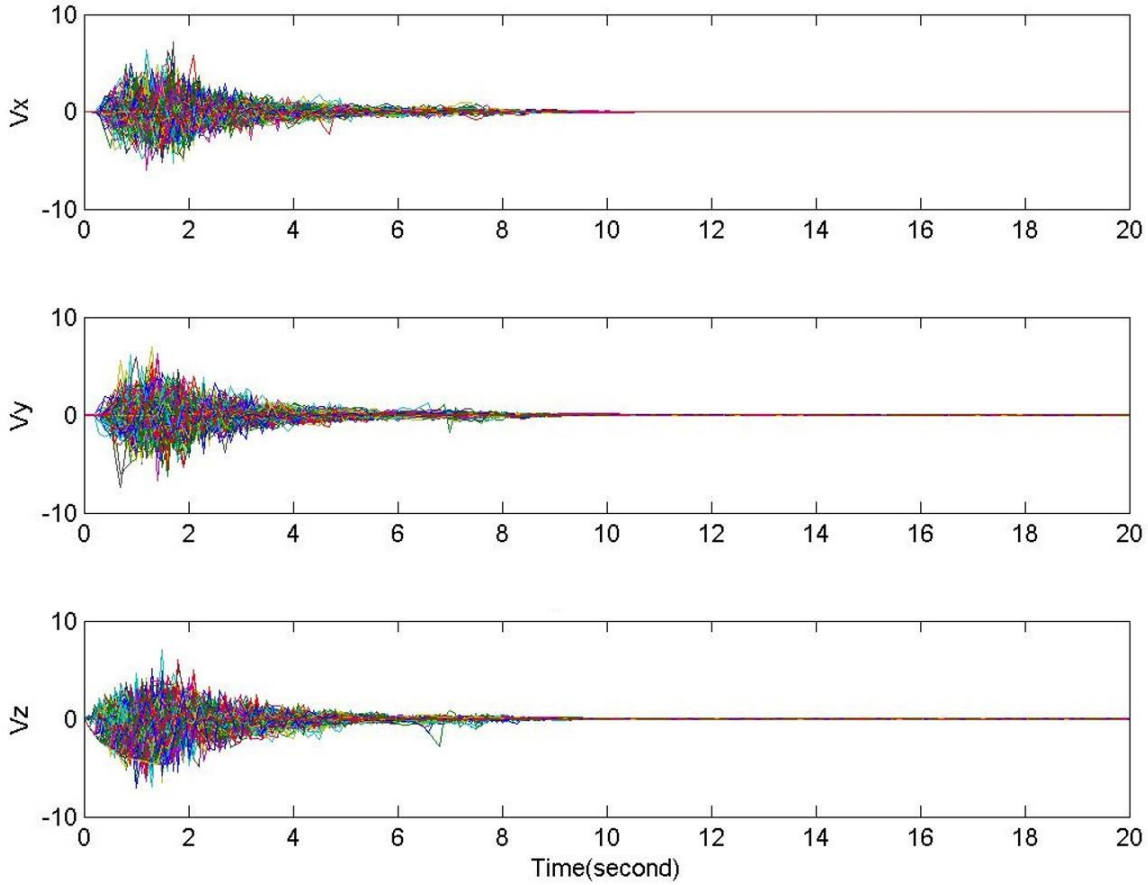


Figure 2.2. Velocity profile of the particles in all three directions.

Once the particle was considered to be in rest, its position was fixed and a successive particle was dropped into the volume. This process was repeated until the specified number of particles were all deposited and settled. Examples of generated 2D and 3D models of the deposited powders in a constrained volume are shown in Figure 2.3. Once all the particles are in rest, the static contact force between any two adjacent particles can be calculated, based on which, the contact area can be calculated based on Equation 2.5.

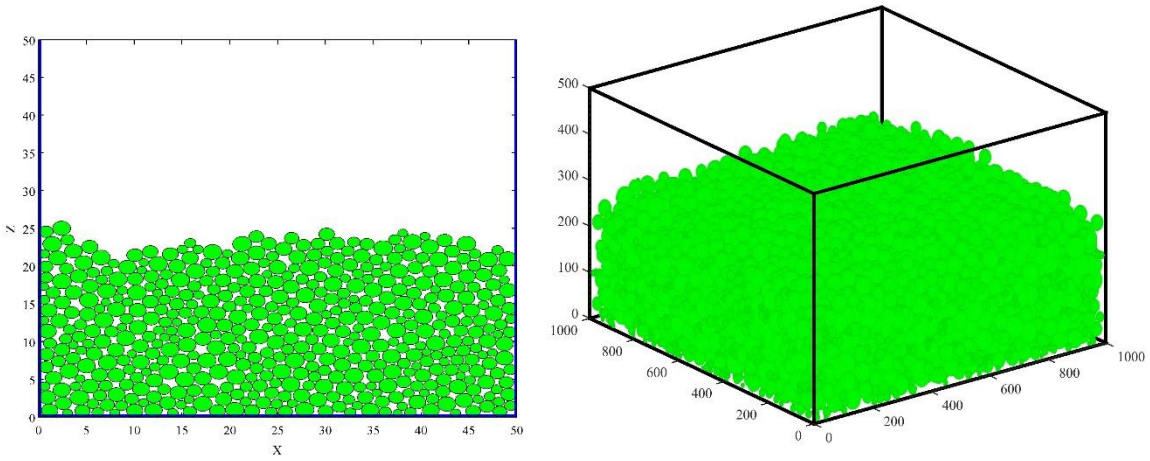


Figure 2.3. 2D and 3D models of deposited powders in a constrained volume.

## 2.4 Ray Tracing Method

In general, $TEM_{00}$ laser beams follow Gaussian beam profile with maximum power intensity at the center and a square exponential decrease toward the outer radius. A simplified model of the power intensity distribution can be expressed as:

$$\mathrm{I(r)} = I_o e^{-\frac{2r^2}{\omega_0^2}} \tag{2.15}$$

where r is the distance from the center of the beam, $\omega_o$ is the radius at which the intensity has decreased to $1/e^2$ or 0.135 of its peak value $I_o$. Figure 2.4 illustrates a model of the power level of a Gaussian beam along the radius.

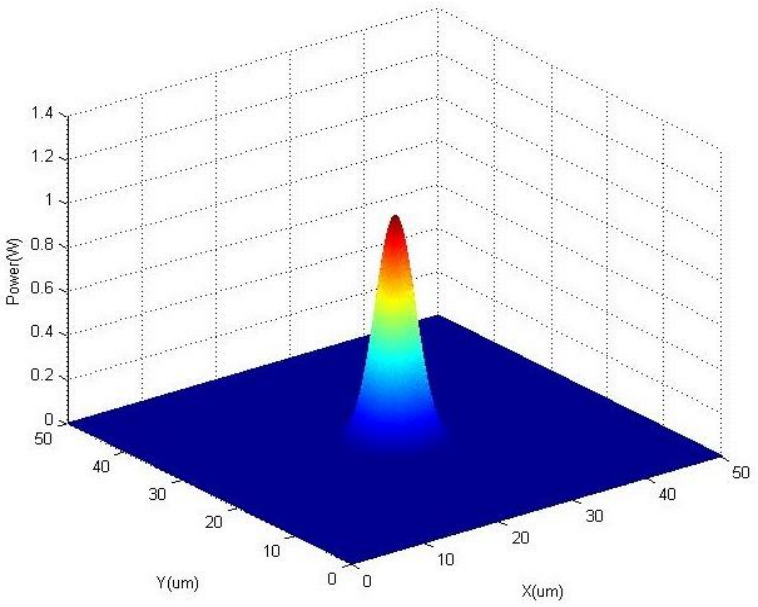


Figure 2.4. Power intensity distribution of Gaussian beams.

In order to apply the ray-tracing method to model laser-power interaction, the laser beam was modeled as a defined number of parallel rays guided towards the powder bed. Each ray was modeled to carry the same amount of energy but the number of rays at a specific radius varies based on the Gaussian profile, which means larger number of rays towards the center. Figure 2.5 demonstrates the distribution of the rays of a laser beam with the diameter of 10 μm.

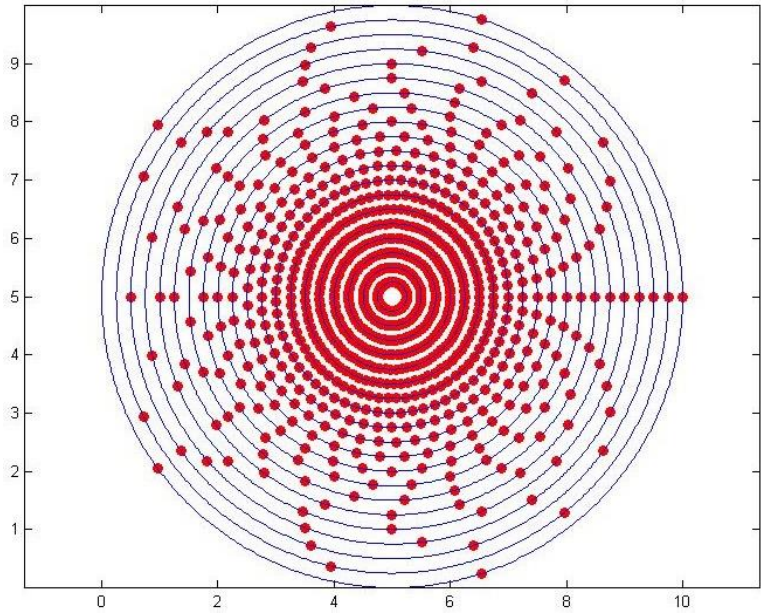


Figure 2.5. X/Y position of the rays distributed by Gaussian profile.

The absorption rate of the particle is estimated to be 70% since the absorption rates of SiC and silicon are around 80% and 60% respectively. An average laser power of 5 W and lasing period of 0.1 second were applied to the created powder bed. When the parallel ray that carries a predefined amount of energy hit a particle, 70% of the energy was absorbed by that particle and the rest was reflected in the direction according to the geometries and locations of the particles as shown in Figure 2.6. The energy of the ray was reduced by 70% after each reflection, and after the fifth reflection, the remaining energy was almost negligible (~0.24%). Therefore, each ray was traced until the fifth reflection. For demonstration purpose, the beam ray was modeled to get thinner after each reflection until it became a dashed line after the fourth reflection, and then disappeared after the fifth

reflection. Any laser rays that are reflected out of the constrained volume were eliminated from the ray-tracing model.

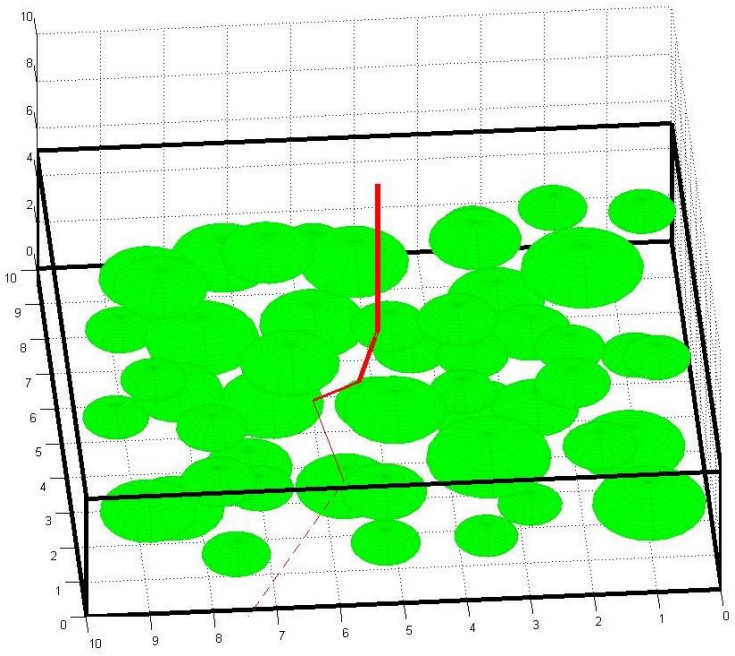

Figure 2.6. Illustration of the ray path after multiple reflections.

## 2.5 Simulation Results

A total number of 10,000 particles randomly generated with the size in the range of 1 – 10 μm were deposited in a constrained volume of 1 × 1 × 0.5 mm after applying the particle dynamics model. The modeled powder bed showed a packing density of around 70%, which is similar to the actual packing density of the powder bed in the micro SLS system. Then, the laser beam, composed of 1000 parallel rays was guided toward the center of the powder bed. As shown in Figure 2.7, after a series of absorption and reflection of the rays among particles, heat conduction among the particles was calculated based on the

temperature differences between adjacent particles. During the process, if a particle reached its melting temperature, it was considered to be molten and marked in the powder bed.

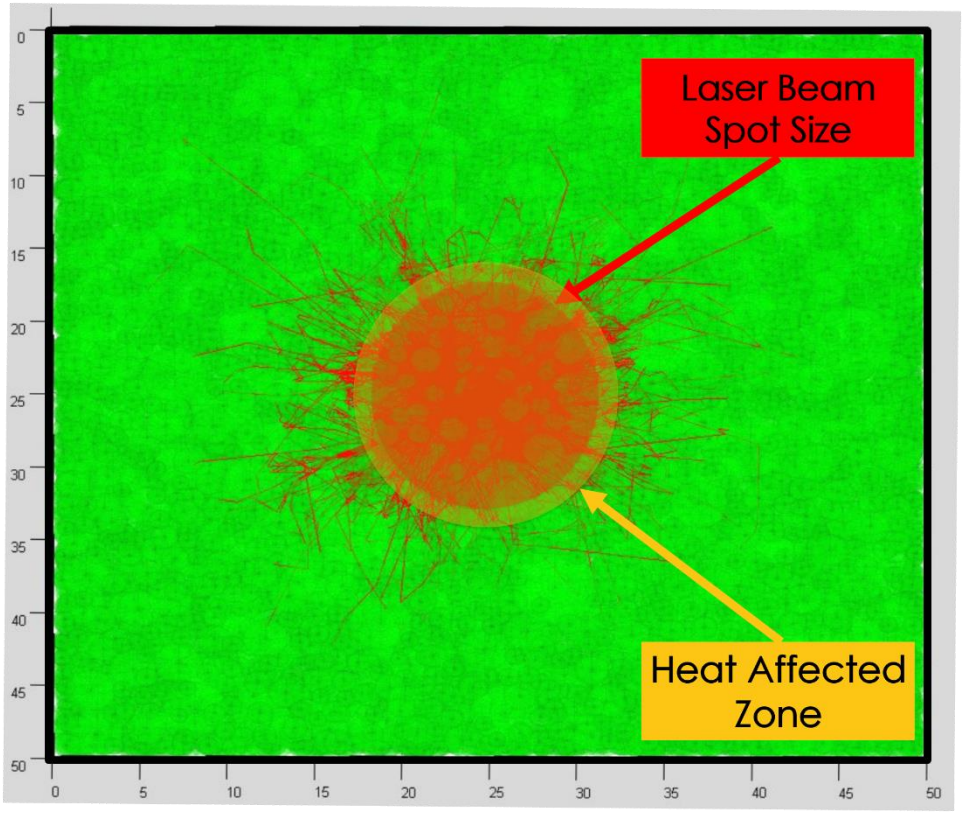


Figure 2.7. Heat-affected zone versus laser beam spot size.

Figure 2.8 presents the energy levels of the particles in all three directions. Blue region indicates the energy threshold for melting, and the red particles above it show particles that have absorbed sufficient energy to melt. Therefore, the heat-affected zone in XY plane was estimated to be around 13 µm for the beam spot size of 10 µm according to

the chart in Figure 2.8. The laser beam penetration depth was estimated to be around 14 μm according to the particle energy level in Z direction.

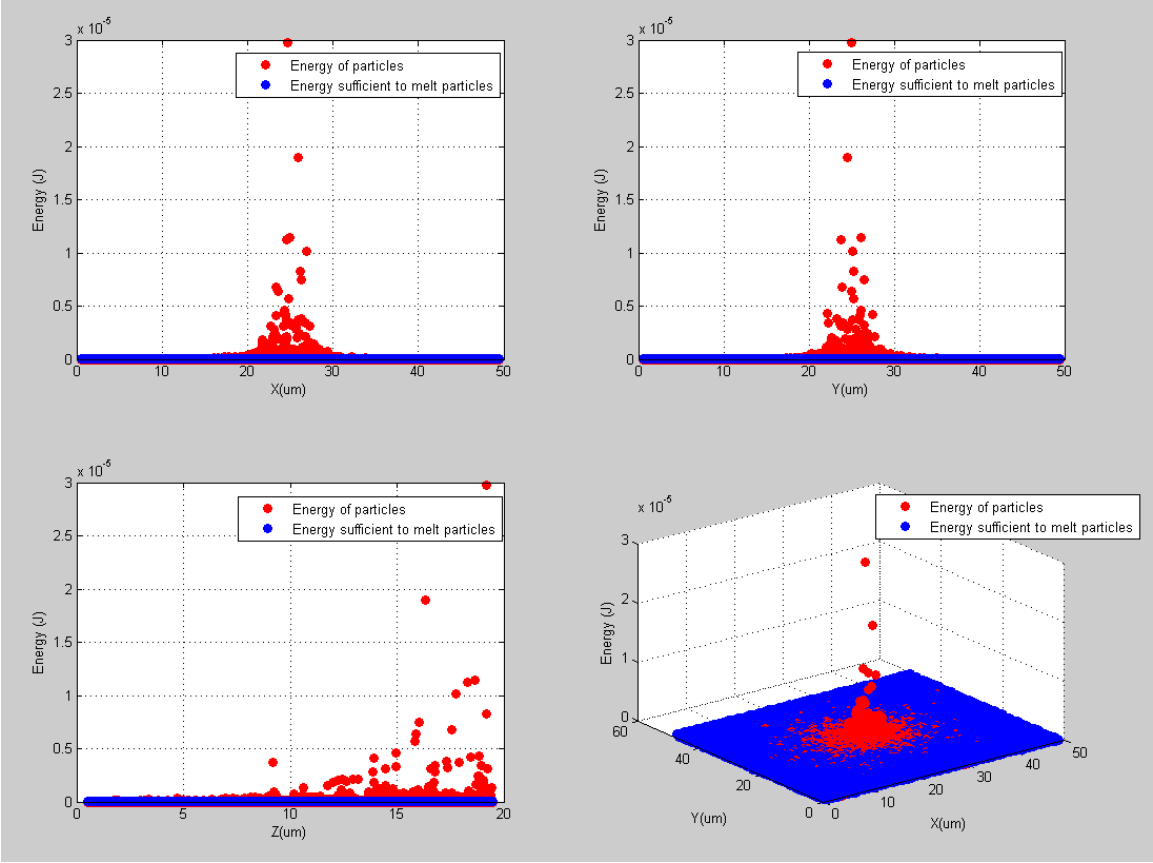


Figure 2.8. Resulting energy level of particles.

Due to the uncertainty of the configuration of the powder bed due to various particle sizes and deposition locations, Monte Carlo algorithm was used by creating a new powder bed with newly generated particles randomly deposited in the same constrained volume. After the absorption of laser radiation and heat conduction among particles, the heat-affected zones and beam penetration depths for a total of five powder beds were calculated,

which showed an average heat-affected zone of 13.4 μm in X and Y direction and an average beam penetration depth of 14.4 μm for particles with the size in the range of 1 – 10 μm. Four types of powder beds that are composed of particles with the size in the range of 1 – 5 μm, 1 – 10 μm, 1 – 15 μm, 1 – 20 μm were created and modeled under laser radiation with average laser power of 5 W and scan period of 0.1 second. As shown in Figure 2.9, the heat-affected zone in X/Y direction and laser penetration depth both show nearly linear increase with the increase in particle size in the powder bed. Thus, for a predefined powder bed with known particle size range, the optimal laser power and scan speed can be estimated to achieve the desired featuring resolution in X/Y direction. Optimal layer thickness can also be obtained from the model by estimating the laser penetration depth in Z-direction.

Consequently, this simulation model can be used to estimate the featuring resolution in X/Y direction as well as the optimal layer thickness for a predefined particle size and processing parameters. It has been used during the subsequent experimental study to estimate the ideal laser parameters such as average laser power, scan speed, and layer deposition thickness based on the particle size and resulting heat-affected zone and penetration depth that were acquired from the modeling results.

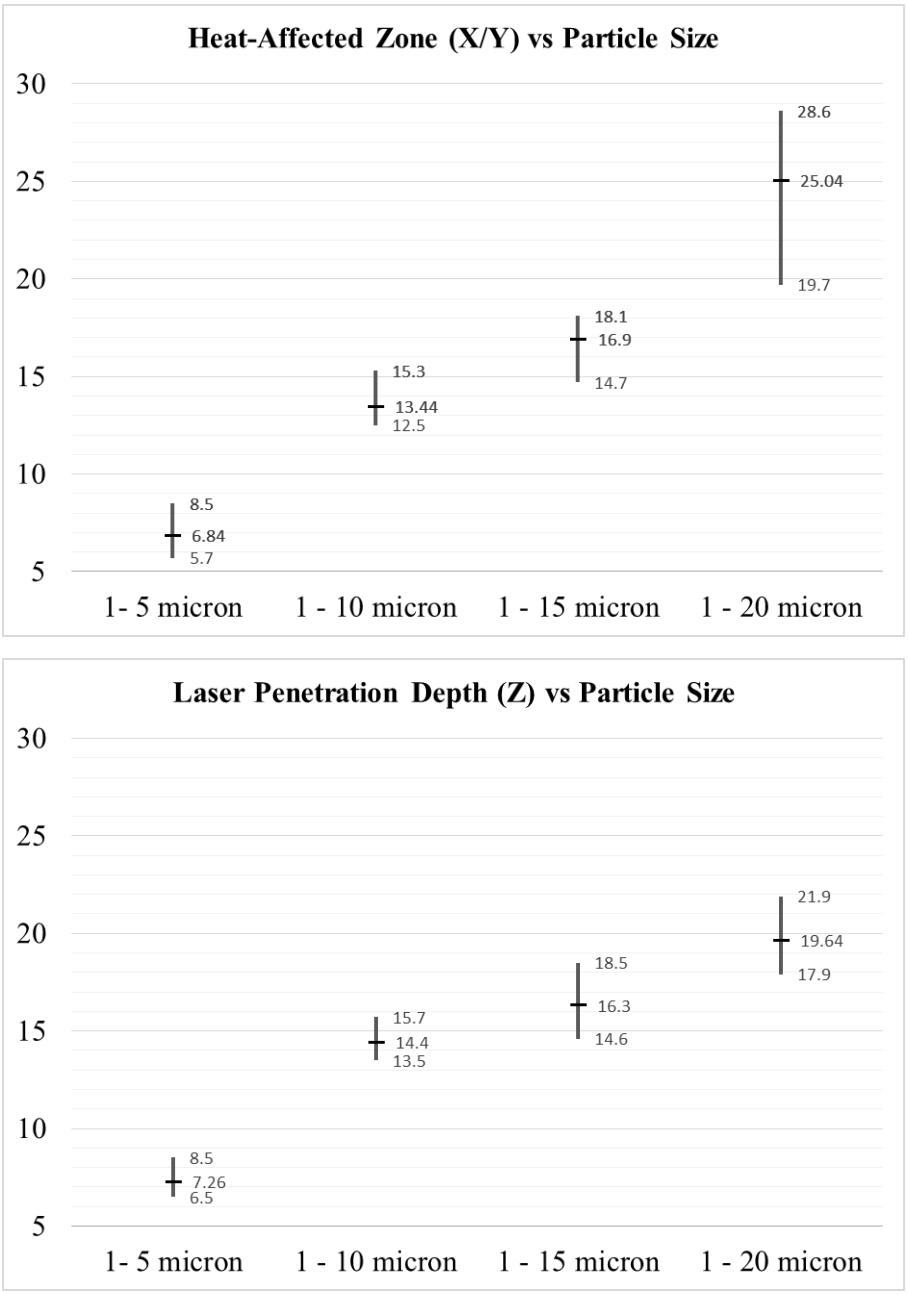


Figure 2.9. Heat-affected zone (X/Y) and penetration depth (Z) for powder beds with particles in different particle sizes.

## 2.6 Simulation of Laser Sintering of Silicon Powder

Single-line laser sintering of silicon powder was conducted in order to investigate the feasibility of the simulation model. Crystalline/amorphous silicon powder with particle size of 1 – 20 μm and purity of 99.9985% (metal basis impurities) from Alfa Aesar (PN: 38715) was used for the experiment. In order to confirm the size and shape of the particles, a small amount of the silicon powder was dispersed in ethanol and then dried to be tested under SEM. As shown in Figure 2.10, most particles were less than 20 μm in size and also exhibited near-spherical shapes. It is ideal for comparison with the simulation because the particles are all modeled in spherical shapes in the powder bed.

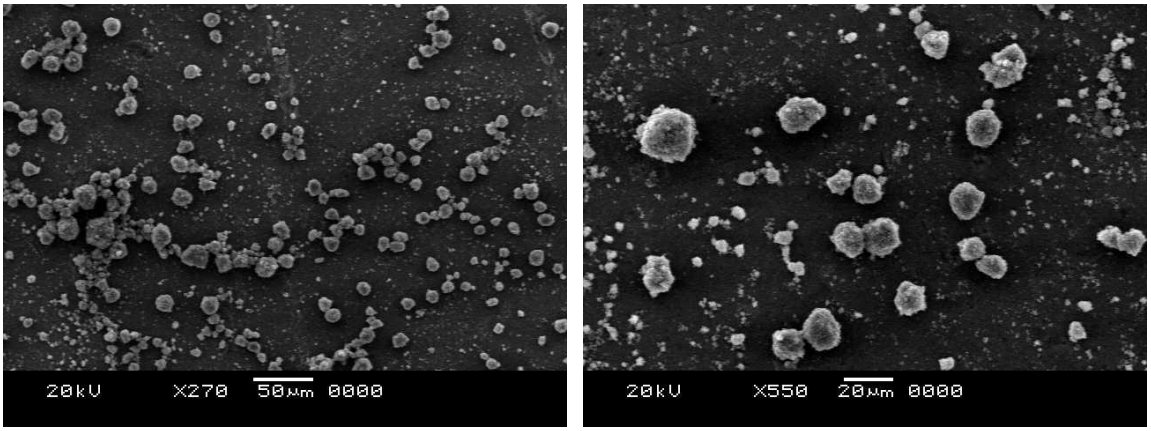


Figure 2.10. SEM views of the silicon particles.

Laser sintering of a single spot was conducted with the laser power of 5 W and lasing time of 0.1 second, which was the same as in the model in order to compare with the simulation results. The sintered spot was then dispersed in ethanol to remove all residual

powders around it, and then was observed under SEM. As the particle size varies in the powderbed, some sintered spots showed bonding of dozens or hundreds of small particles whereas others showed bonding of a few large particles with small particles among them as shown in Figure 2.11. Although it was very difficult to identify the heat-affected zone in X/Y-direction and the beam penetration in Z-direction from the SEM views, the average melt volume was measured to be in the range of 20 – 40 μm in all three directions. Consequently, the experimental results were close to the estimations acquired from the simulation model that predicted the heat-affected zone of 25 μm in X/Y-direction and heat penetration depth of 20 μm in Z-direction. The actual size of the sintered spot was larger than the estimated results possibly due to the existence of the sub-micron sized particles in the powderbed, which can melt at temperatures lower than the melting temperature of bulk silicon. In addition, the absorption rate of the particles also varies depending on the temperature and phase of the particles.

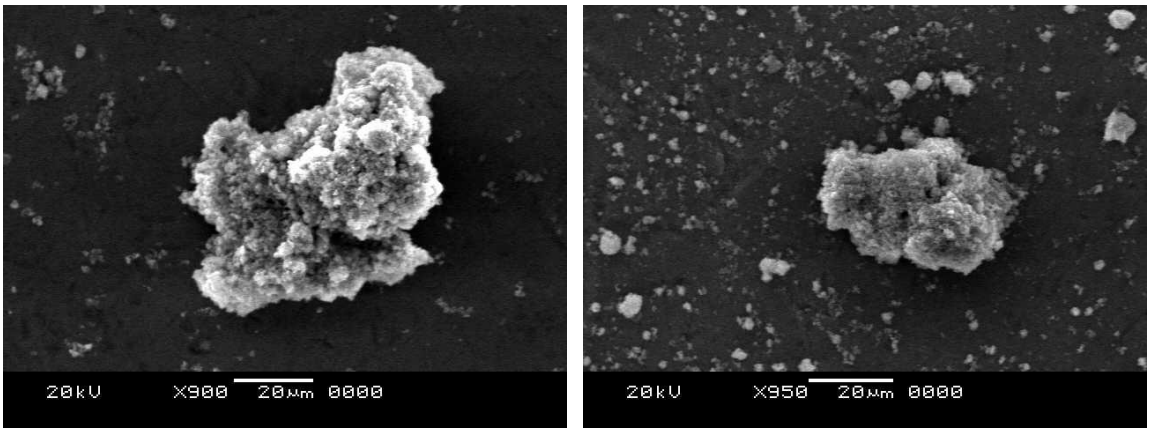


Figure 2.11. SEM image of a laser-sintered single spot.

In summary, the simulation model was able to estimate the size of the melt volume in all three directions based on the ray-tracing method for the laser beam coupled with the thermal modeling of the particles. Featuring resolution at specific processing parameters can be estimated accordingly. The laser scanning process can be modeled by applying a certain velocity to the beam rays in horizontal direction. As the particles melt to liquid phase, the properties of the material would change and may affect the sintering results. This phenomenon may also be included in the simulation model to improve accuracy in estimation. The melting temperature of a sub-micron sized particle varies depending on the size of the particle. Therefore, the melting temperature can be modeled as a function of the particle size, which can help to identify all the sub-micron-sized, molten particles that were observed in the experimental results but not from the simulation models. In addition, the generation of the powderbed in a constrained volume takes unnecessarily long time of typically a few hours. Thus, a more simplified method other than the application of particle dynamics is needed to reduce the simulation time.

# Chapter 3: Micro SLS System Design

This chapter is focused on the design of a micro SLS system that is capable of direct sintering or melting of metallic and ceramic powder materials with micro scale featuring. The schematics of the SLS system is shown in Figure 3.1. Major components of a typical SLS system include laser, scanner, focus lens, control unit, sintering chamber, vacuum pump, and powder bed with coating system. Modifications and improvements of the system are discussed in detail.

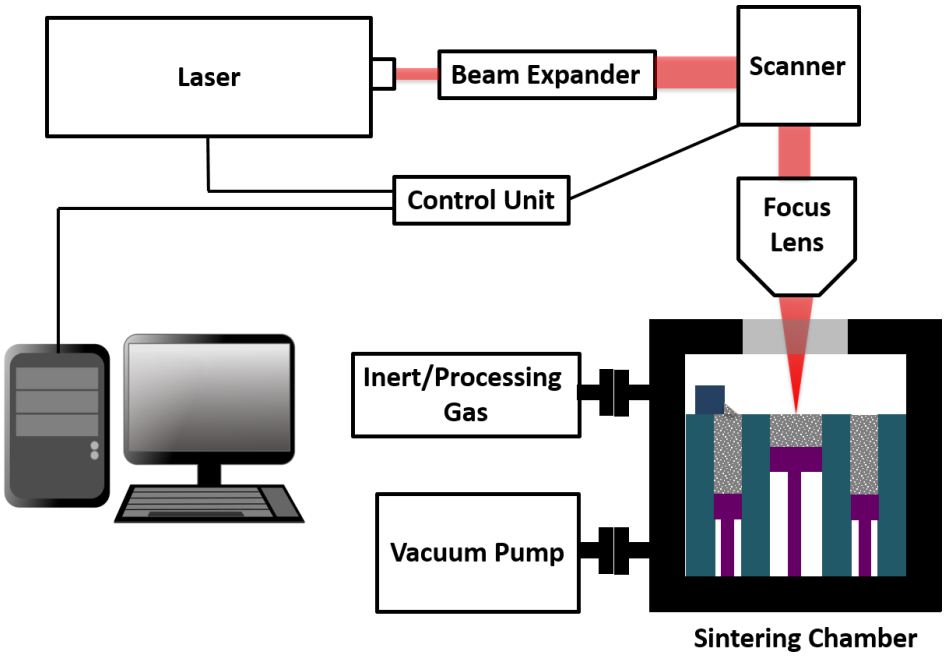


Figure 3.1. Schematics of typical SLS system.

## 3.1 LASER SYSTEM

The choice of a proper laser for the proposed micro SLS system is mainly dependent on the material to be processed. Most importantly, the laser wavelength should be adapted to the powder material to be sintered or melted as laser absorption rate varies significantly with the material. In addition, high beam quality with focusable beam spot down to a few microns is critical for the current system since it aims for micro-scale featuring resolution. Other laser characteristics such as emission beam type, energy density, repetition rate, pulse duration, ease of operation, and maintenance requirement need to be taken into account for the micro SLS system with material-specific applications.

### 3.1.1 Laser Comparison

Different types of laser have been applied in SLS including continuous wave $CO_2$ laser, continuous wave Nd:YAG lasers, q-switched Nd:YAG laser, short-pulse Cu-vapor laser, diode laser, etc. depending on the specified applications [67]. $CO_2$ lasers with wavelength of 10.6 μm are suitable for sintering polymer and oxide ceramic powders, which exhibit high absorption at far infrared or long wavelength. However, metals and carbide ceramics show better absorption rate at short wavelength of 1064 nm. Absorption rate of single-component powders at 1064 nm and 10.6 μm wavelengths are listed on Table 2.1 [68]. Experimental results also suggest that for the same amount of energy input, Nd:YAG laser outperforms $CO_2$ laser in terms of sintering depth, part density, and energy efficiency. As the current research is focused on metal and carbide ceramic powders, a

pulsed laser with 1064 nm wavelength is definitely a better choice over 10.6 μm wavelength in terms of the absorption rate.

Table 3.1 Absorption rate of single-component powders at two wavelengths

| Powder materials | λ = 1064 nm | λ = 10.6 μm |
|---|---|---|
| **Cu** | 59% | 26% |
| **Fe** | 64% | 45% |
| **Sn** | 66% | 23% |
| **Ti** | 77% | 59% |
| **Pb** | 79% | N/A |
| **ZnO** | 2% | 94% |
| **$Al_2O_3$** | 3% | 96% |
| **$SiO_2$** | 4% | 96% |
| **SnO** | 5% | 95% |
| **CuO** | 11% | 76% |
| **SiC** | 78% | 66% |
| **$Cr_3C_2$** | 81% | 70% |
| **TiC** | 82% | 46% |
| **WC** | 82% | 48% |
| **Polytetrafluoroethylene** | 5% | 73% |
| **Polymethylacrylate** | 6% | 75% |
| **Epoxypolyether-based polymer** | 9% | 94% |

With the development of the fiber laser, which is a special type of solid-state laser, latest SLS systems like EOS M 100, EOS M 290 from EOS® normally uses Yb-fiber lasers to replace Nd:YAG lasers due to the enhanced beam quality, smaller laser spot size, and stable performance. Compared to Nd:YAG lasers, advantages of the fiber laser includes collimated beam delivery with flexible fiber, high optical gain, high precision and accuracy with high-efficiency, fast and localized energy deposition, short pulse widths, wide wavelength tuning range, maintenance-free operation, compact size, and lower cost.

### 3.1.2 Laser Power Intensity and Spot Size

For a Gaussian beam propagating in free space, the beam waist or the spot size (radius) $w_z$ is a function of wavelength and distance z along the beam direction:

$$w_z = w_0 \sqrt{1 + \left(\frac{z}{z_R}\right)^2} \tag{3.1}$$

where $z_R$ is the Rayleigh range defined as:

$$z_R = \frac{\pi w_0^2}{\lambda} \tag{3.2}$$

The power intensity (I) can be calculated as:

$$I = \frac{P_{max}}{A} = \frac{P_{AV}}{\tau_H f_p A} = \frac{P_{AV}}{\tau_H f_p \pi w_z^2} \tag{3.3}$$

where $P_{AV}$, $\tau_H$, $f_p$, and $w_z$ are the average power of the laser, half width of pulse duration, repetition frequency, and beam waist radius respectively. It means that for a predefined power intensity, the average laser power required is proportional to the square of $w_z$. Commercial high-power SLS machines like EOS M series are equipped with Yb-fiber lasers with power ratings of 200 – 400 W and focus diameter of 100 – 200 μm. Therefore, the average laser power in the range of 2 – 10 W is sufficient for the proposed micro SLS system that aims for the minimum spot size of 10 μm, assuming the same repetition frequency and pulse width. Also, Streek and Exner suggested laser beam intensity in the range of 30 – 70 MW/cm$^2$ for SLS of carbide ceramics [64-66], which is equivalent to the average laser power of 2 – 5 W under the same frequency and pulse width. Therefore, a fiber laser with tunable power of up to 20 W should be sufficient for processing most metallic and carbide ceramic materials with high absorptance.

### 3.1.3 Laser Selection

Based on these considerations, Ytterbium pulsed fiber laser (YLP-1-100-20-20-HC-RG) from IPG® was selected for the micro SLS system. Specifications of the laser and the tested results are presented on Table 3.2. Main features of the selected laser includes:

- Collimated output beam focusable down to a few microns
- Tunable output laser power and repetition rate ( 2 – 20 W)
- Over 10% wall-plug efficiency
- Fiber delivery of laser beam

- Maintenance-free operation
- Compact rugged air-cooled package
- High resistance to shock, vibration, dust, and humidity

Table 3.2 Specification of the YLP fiber laser for micro SLS system

| Characteristic | Typical Value | Test Conditions | Test Results | Unit |
|---|---|---|---|---|
| Mode of operation | Pulsed | | Pulsed | |
| Nominal average output power | 20 | RR = 20 kHz | 20.5 | W |
| | | RR = 200 kHz | 20.7 | |
| Output power adjusting range | 10 – 100 | | 10 – 100 | % |
| Emission wavelength | 1064 | $P_{out} = P_{nom}$ | 1064.5 | nm |
| Emission bandwidth | 5 | FWHM | 4.1 | nm |
| Pulse repetition rate (RR) | 20 – 200 | | 20 – 200 | kHz |
| Pulse duration | 100 ns | FWHM<br>$P_{out} = P_{nom}$<br>RR = 20 kHz | 107.8 | ns |
| Laser switching ON time | 170 | 0% - 90% $P_{nom}$ | 160 | µs |
| Laser switching OFF time | 2 | | 1.1 | µs |
| Pulse energy | 1 | $P_{out} = P_{nom}$<br>RR = 20 kHz | 1.03 | mJ |
| Long-term average power instability | 5 | $P_{out} = P_{nom}$<br>Over 5 hours | < 3 | % |
| Output beam diameter | 7.5 | 86% level | 7.2 | mm |
| Nominal current consumption | 7 | $P_{out} = P_{nom}$ | 4.09 | A |

## 3.2 SCANNING SYSTEM

In order to focus the laser beam spot down to 10 μm, the collimated beam from the laser head needs to be expanded at first. The variable beam expander from Edmund Optics® for 1064 nm wavelength was applied between the laser head and the scanner input. For the current system, the beam expander was tuend to the magnification of 3X. The telecentric F-theta lens for 1064 nm wavelength from Sill Optics® was used to focus the beam onto the powder bed. The specifications of the lens is presented in Table 3.3.

Table 3.3. Specifications of the telecentric F-theta lens

| Characteristics | Value |
|---|---|
| Design wavelength (nm) | 1064 |
| Effective focal length (mm) | 79.9 |
| Max. entrance beam diameter (mm) | 10 – 100% |
| Optical scan angle (±°) | 21.5 |
| Scan length (mm) | 58.5 |
| Aperture stop distance (mm) | 27.2 |
| Working distance (mm) | 79.5 |
| Scan area for a 2 mirror scan system with mirror distance from lens housing for mirror 2 / mirror 1 | 39 × 39<br>12.2 / 42.2 |
| Max. telecentricity error (°) | 3.8 |
| Total transmission (%) | > 96 |
| Damage threshold | 5.0 J/cm$^2$ per 1 ns pulse at 50 Hz<br>5.0 GW/cm$^2$ for continuous wave |

## 3.3 SINTERING CHAMBER

The sintering chamber is composed of the sintering bed inside and the vacuum chamber that is connected to the vacuum pump. The PZS-90 elevation stage from MicronixUSA® was used to drive the center piston. It is capable of operation in high vacuum environment ($10^{-6}$ mbar) with key features including vertical travel range of 35

mm, 0.1 µm closed loop resolution, load capacity up to 15 kg, and integrated mechanical limit switches. 2-phase stepper motor from Phytron® was used to drive the powder coating blade on the sintering bed. This motor is also capable of high-vacuum operation with step accuracy of 5% for 1.8°. The assembly of the sintering platform is shown in Figure 3.2 (left). Then, the sintering bed was housed in the stainless steel vacuum chamber custom-designed by Kurt Lesker® as shown in Figure 3.2 (right). During the operation, the sintering chamber is closed for vacuum operation with the laser window on the top lid to allow laser to pass through.

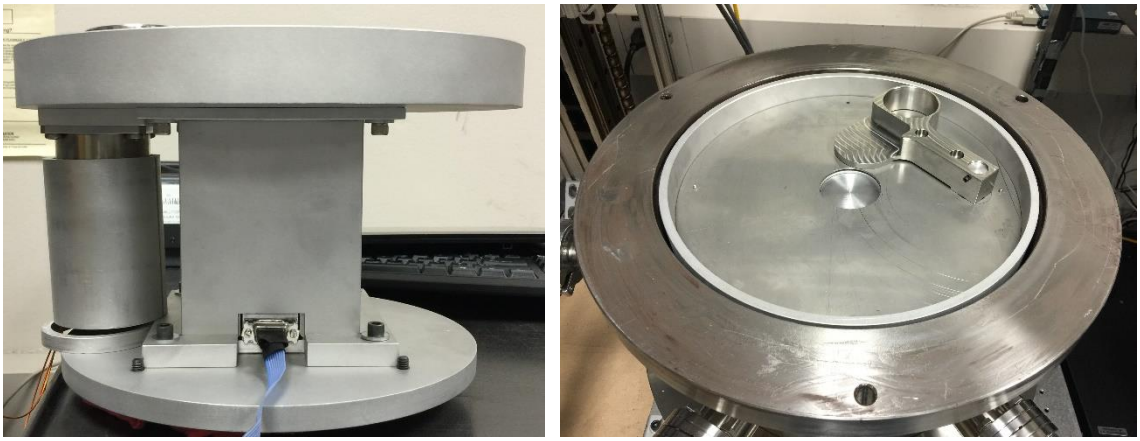

Figure 3.2. Sintering platform assembly.

### 3.4 Powder Coating and Compression System

The powder coating system was designed with the addition of powder compression functionality as shown in Figure 3.3. As the particle size gets smaller, low-density powders like SiC tend to pack loosely. A powder compression system can increase the packing density of the powder bed, and thus reduce the porosity and enhance the heat conduction

among particles. After the center piston is lowered, a stainless steel blade with attached powder reservoir moves across the center powder bed to deposit one layer of powder as shown in Figure 3.3 (a). If powder compaction is desired, the closed cap of the blade aligns with the center piston followed by compression of the powder by moving center piston upward as shown in Figure 3.3 (b). This compression process becomes more important for micron-size, light-weight powders such as oxide and carbide ceramic powders. Then, the powder blade moves away from the center probe, waiting for the completion of laser sintering as shown in Figure 3.3 (c). Finally, when the center piston is lowered again, the coating blade rotates back to the original position as shown in Figure 3.3 (d). This process is repeated for continuous layer deposition and laser sintering. Compared to the conventional roller system, powder blade mechanism combined with the compaction process enables delivery of more coherent and compact powder layer as well as much finer powder surface, which can significantly reduce porosity as well as increase heat conduction among particles.

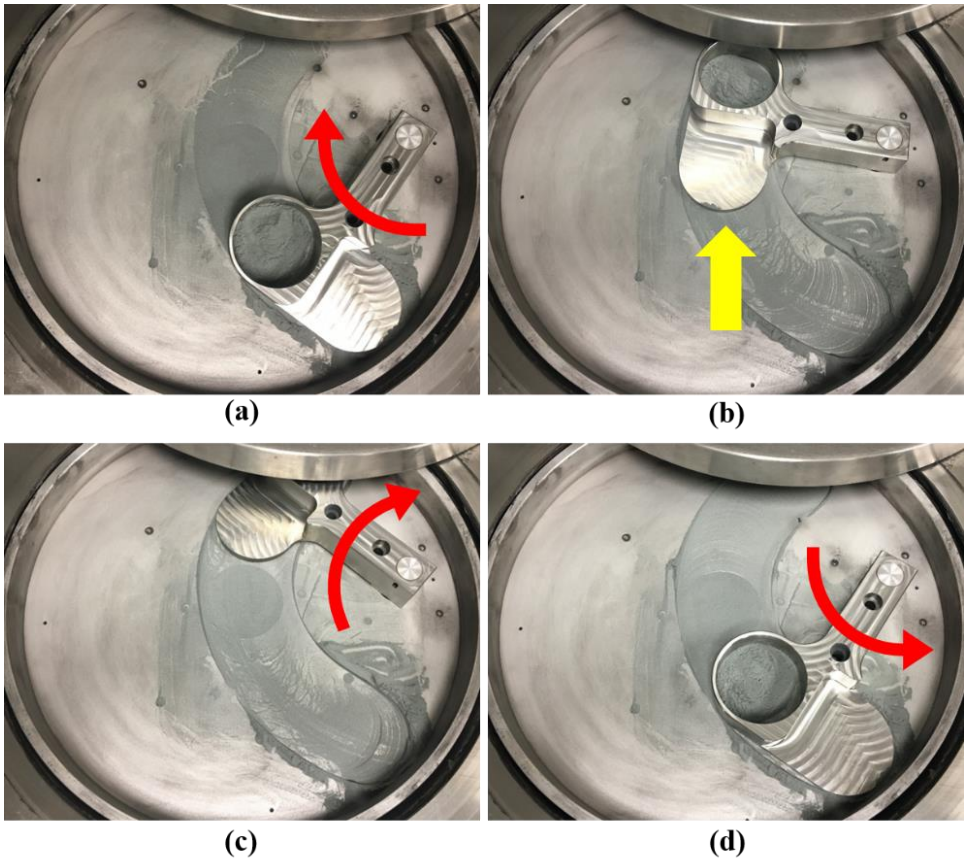


Figure 3.3. Powder coating and compaction mechanism.

### 3.5 MICRO SLS SYSTEM ASSEMBLY

The assembly of the micro SLS system is shown in Figure 3.4. It includes several modifications and improvements based on traditional SLS machines. First, a continuous-wave $CO_2$ laser was replaced by ytterbium pulsed fiber laser with adjustable power in the range of 2 – 20 W and repetition rate in the range of 20 – 200 kHz as mentioned previously. The collimated laser beam is guided through the beam expander and then into the galvo

scanner. The output beam from the scanner is then focused by an F-theta lens with a focal length of 80 mm. For a wavelength of 1064 nm operated in $TEM_{00}$ mode, the laser beam can be focused onto a spot with a diameter as small as 10 μm, depending on the diameter of the unfocused beam and the beam quality factor $M^2$ of the laser as follows:

$$D_{focused} \approx \frac{4\lambda\left(\frac{f}{D}\right)M^2}{\pi} \tag{3.4}$$

A traditional powder feeding roller was replaced by cylindrical blade design. The galvo scanner was mounted on an elevation stage so that the laser spot size can be controlled by adjusting the stage in vertical direction. A high-vacuum stainless steel chamber was used for SLS processes that require a vacuum or inert gas environment. ScanMaster Designer® software was used to import and slice CAD files for laser processing. The sintering platform was placed in a stainless steel chamber that is capable of high-vacuum and inert gas operations. Build area is 50 mm in diameter and 30 mm in depth.

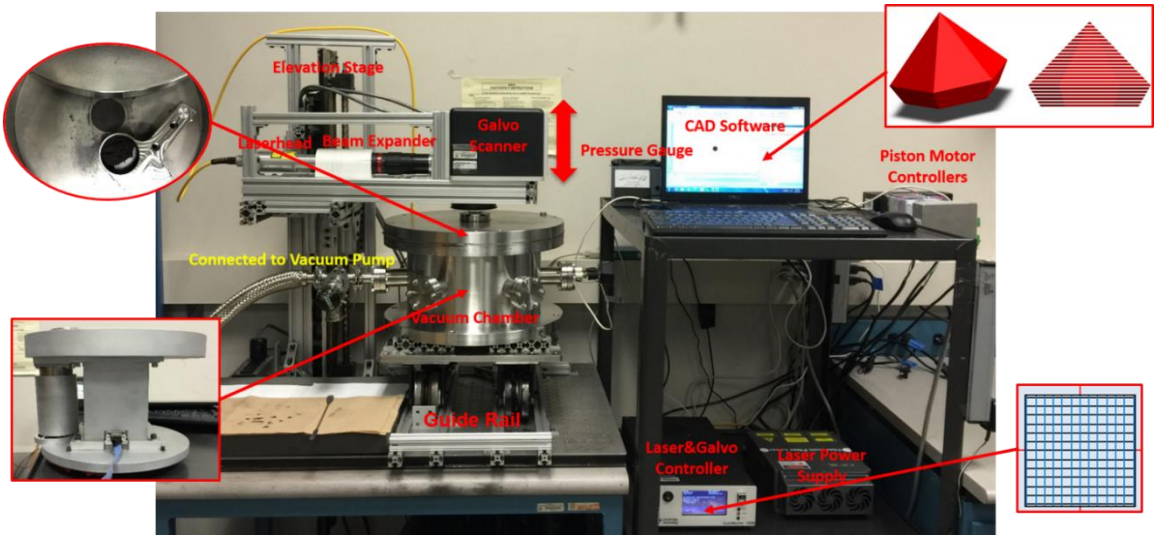


Figure 3.4. Assembly of the micro SLS system.

# Chapter 4 : Micro Selective Laser Sintering for SiC Preforms

Selective Laser Sintering (SLS) coupled with high-temperature furnace sintering provides a versatile, cost-effective tool for the additive manufacturing of metallic or ceramic composites with full density [59]. The processing powder for ceramics is normally composed of a structural material and a binder material. Resolution of the part is limited by the particle size of the structural material whereas the processing parameters, such as laser power and scan speed mainly depend on the properties of binder material [69]. An SLS-processed green part is fabricated in the system, which consists of the ceramic powders selectively bound by a binder material and have a continuous porosity network due to the inherent porosity in the powder packing and the partial decomposition of the polymer binders under laser radiation. Parts are then infiltrated during a post-processing step to achieve full density with improved material properties. Infiltrated SLS composites that are commonly used include polymer-infiltrated polymers, polymer-infiltrated metals, polymer-infiltrated ceramics, metal-infiltrated metals, and metal-infiltrated ceramics [62,63].

Various attempts have been made for the additive manufacturing of SiC parts in terms of improving resolution. Complex shapes and features were achieved by Stierlen and Eyerer when smaller particle size of 15 μm was used, but structural resolution below 200 μm was not successful and further reduction of particle size was limited by the decrease of the optical absorption depth at the wavelength of the $CO_2$ laser radiation [64]. Both

Streek and Meyers attempted direct laser sintering of pure SiC and Si-SiC with the application of pulsed laser and redesigned powder coating system, generating parts with high resolution but only simple geometries. Also, the mechanical properties of the directly laser-sintered parts are not comparable to that of traditional SiC due to high porosity and loose bonding among SiC particles [65,70].

In this chapter, a material-specific micro SLS process is described in terms of producing SiC preforms with complex geometry, micro scale resolution and high structural integrity that can turn into functional parts after post-processing infiltration during furnace sintering. It also seeks to investigate the feasibility and potential applications of the newly developed micro SLS system for the generation of high-resolution ceramic preforms.

## 4.1 EXPERIMENTAL

### 4.1.1 Powder Preparation

Commercial grade α-phase SiC powders (120, 320, and 600 grit) provided by Alfa Aesar, Inc., were used to prepare three types of powders with average particle sizes (APS) of 100, 30, and 15 μm respectively. In terms of the specification of the powders, these SiC powders have >98.5% purity with impurity content of free carbon (< 0.4%), free silicon (< 0.6%), iron (III) oxide $Fe_2O_3$ (<0.2%), silica $SiO_2$. The reported particle size conforms to FEPA-Standard 42-1:2006. Additional 5 wt.% of α-phase SiC powder with APS of 2 μm and purity of 99.8% (metal basis) was added in order to make the powder packing uniform

for better heat conduction and lower porosity as shown in Figure 4.1. GP-5546 phenolic resin provided by Georgia Pacific Resins, Inc., was further milled down to APS of 11 μm, which was then mixed with SiC powder at 10:100 weight ratio in a cement mixer for 5 hours. At elevated temperature of 300 – 1000 °C, these phenolic resins would convert to structural carbon, which behaves similar to ceramics and may contribute to the structural integrity of the SiC parts.

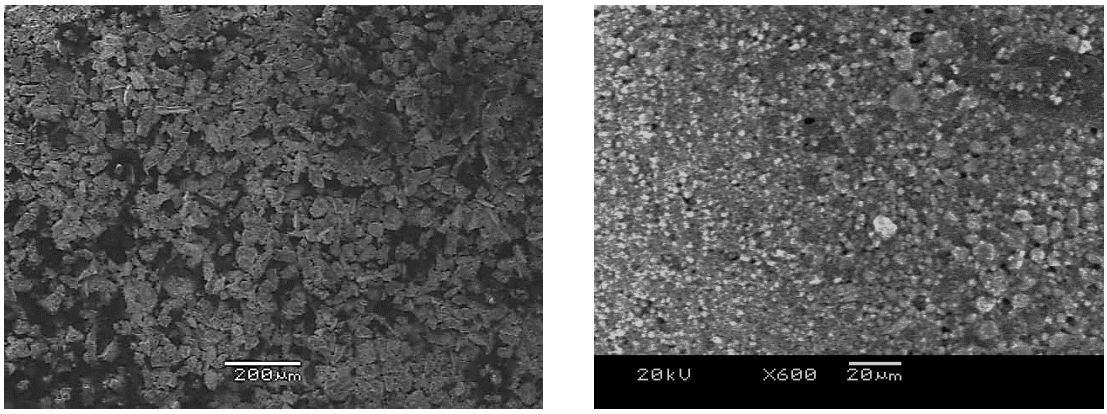


(a) (b)

Figure 4.1. Examples of poor (a) and compact (b) powder packing of SiC.

### 4.1.2 Micro SLS of Phenolic-SiC Powder

Three main parameters, including average laser power, scan speed, and scan spacing were investigated respectively. Other operating parameters were as follows: laser spot size, 50 – 200 μm; layer thickness, 50 – 200 μm; laser repetition rate, 100 kHz; laser pulse width, 100 ns; powder bed temperature, 25 °C; Inert gas or vacuum was not used since the applied laser power was not sufficient to cause decomposition or oxidation of SiC

particles. Preliminary testing was focused on laser sintering of SiC powders with APS of 30 μm. Laser pulses with average power from 2 – 20 W and scan speed of 1 – 1000 mm/s were tested in order to find the acceptable ranges that yield solid, non-oxidized layer with minimal heat-affected zone.

### 4.1.3 Infiltration of Silicone as Transient Binder

After SLS processing, the SiC preforms were infiltrated with silicone resin that was dissolved in xylene in 1:1 ratio to reduce viscosity. The silicone functions as a transient binder to maintain structural stability between phenolic softening at 70 °C and crosslinking at 150 °C. Compared to the mostly commonly used transient binder, epoxy, which requires additional post-curing in furnace, silicone does not require any post-processing and can well maintain the structure. The liquid xylene remaining in the infiltrated parts were dried off with forced air at room temperature for 5 hours.

## 4.2 Results and Discussion

SLS of phenolic-SiC powder with APS of 30 μm was conducted starting from high laser power and high scan speed. Figure 4.2 (a) illustrates the sublimation of SiC particles by high-energy laser pulses when the average laser power is above 10 W. When the laser power is between 5 – 10 W, vapor and plasma plume produced by q-switch pulses forms a "cloud" above the powder bed. Successive laser pulses passing through the cloud results in a recoil onto the powder bed, condensing it and suppressing it towards the sintered layer below. Controllable recoil effect is beneficial for SLS of light and loosely packed powders

to suppress the balling effect of small particles. However, excessive recoil force can easily interrupts the binding or sintering among particles, causing rougher surface and higher porosity as shown in Figure 4.2 (b).

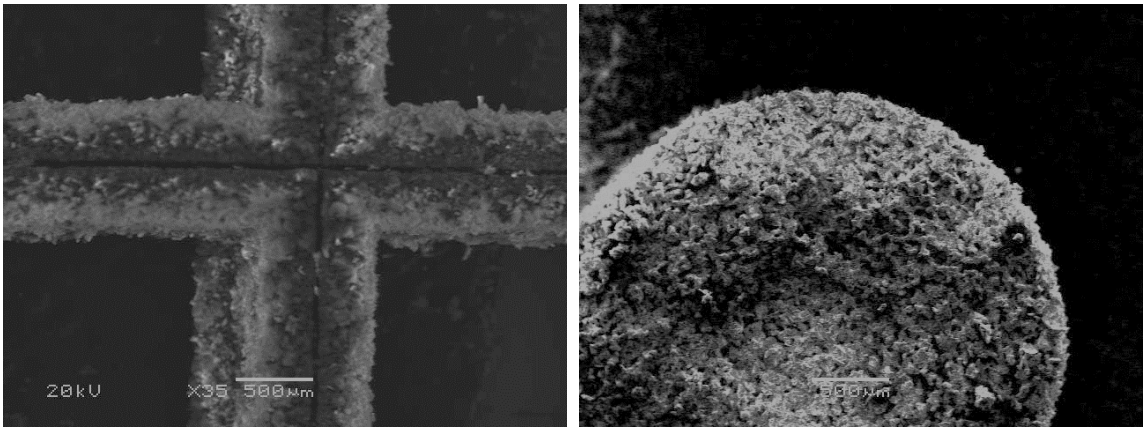


(a) (b)

Figure 4.2. Sublimation of SiC powder along radiation (a) and rough surface caused by excessive recoil force (b).

A total of 16 rectangular prisms (2 × 2 mm) sintered at different laser power and scan speed are shown in Figure 4.3. For instance, cube **m** shows that high laser power and scan speed cause excessive growth of heat-affected zone as expected, whereas cube **d** shows insufficient laser power at high scan speed.

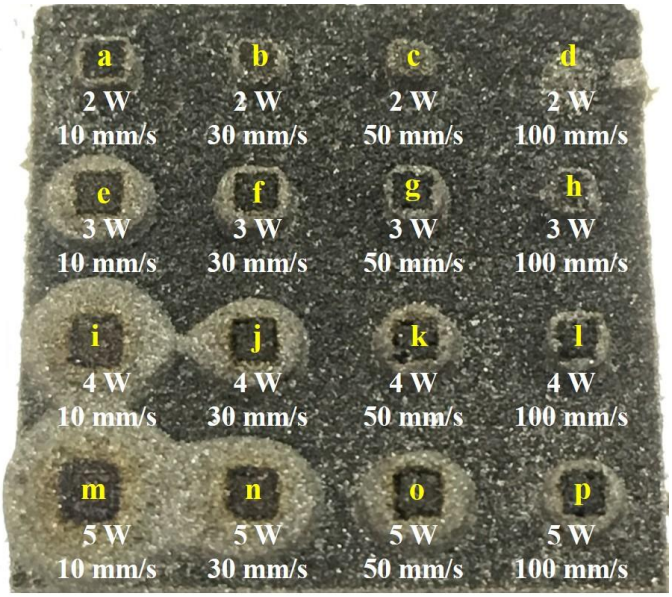


Figure 4.3. Comparison of 16 sintered cubes at different laser power and scan speed.

Once the range of laser power was narrowed down to 2 – 3 W and the range of scan speed was narrowed down to 10 – 50 mm/s based on Figure 4.3, smaller rectangular prisms with the size of 1 × 1 mm were created using the parameters within this range in order to find out the ideal values for solid bonding and minimum heat-affected zone. In terms of the scan speed, since the SLS prefers faster scan speed to enhance the production time, the scan speed was fixed to be 50 mm/s and different values of laser power were tested. After a detailed comparison, the ideal set of parameters were found to be at laser power of 2.5 W at the scan speed of 50 mm/s, which provided sufficient power for structural integrity while minimizing heat-affected zone around the edge as shown in Figure 4.4.

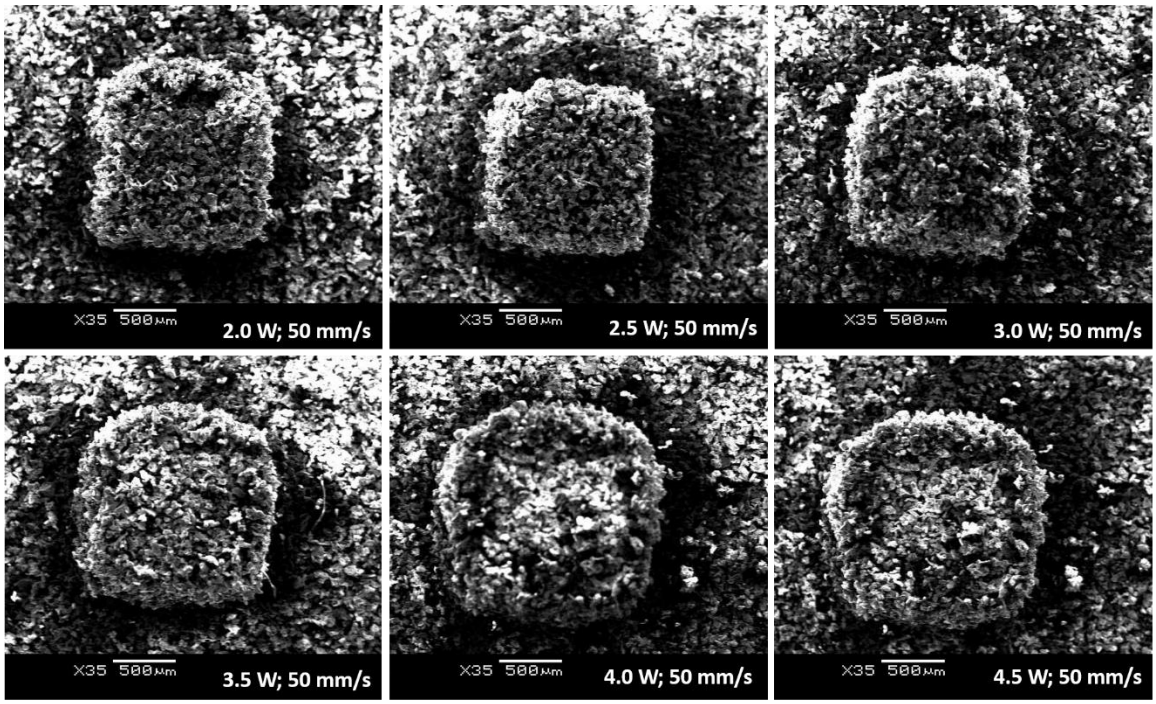


Figure 4.4. SEM images of 1 × 1 mm cubes sintered at different laser power.

The acquired parameters with scan spacing of 50 µm were applied to print small parts with micro size features. Although a certain degree of porosity was inevitable due to volume loss by thermosetting and carbonization of the phenolic binders under laser radiation, small features such as thin bridges with the width of 100 µm were achievable when printing the structural pattern of compliant pin chucks as shown in Figure 4.5 (a). SLS of rectangular prisms and cylinders also showed high degree of structural integrity as shown in Fig. 4.5 (b). When the feature size was further reduced to 50 µm, cleaning off residual powders after sintering became the major challenge and brushes and air blowers could easily break the micro features while removing unsintered particles. Therefore, for

SiC powders with APS of 30 μm, achievable featuring resolution seem to be around 100 μm.

Same procedures were applied to the other two SiC powders with APS of 100 μm and 20 μm, which showed best sintering results with structural resolution of 200 μm and 50 μm at laser power of 2.7 W and 2.5 W; scan speed of 50 mm/s and 60 mm/s respectively. Upon comparison, it was found that the featuring resolution of the SLS-processed parts is closely related to the particle size of SiC due to its role as structural material. Thus, structural resolution was found to be at least 2 – 3 times of the average particle size of the structural material according to the test results. On the other hand, system parameters such as laser power, scan speed, and scan spacing were mainly dependent on the properties of the phenolic binder such as particle size, melting and crosslinking temperature, bonding strength, etc. because it is the only material that melts and bond particles whereas the role of SiC is merely a heat conductor during laser radiation.

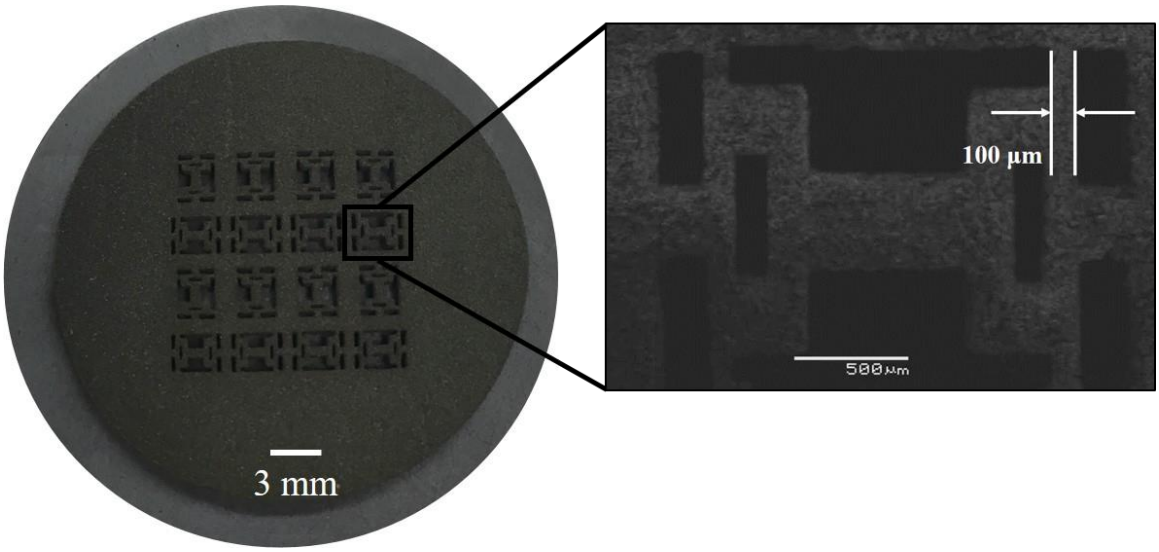


**(a)**

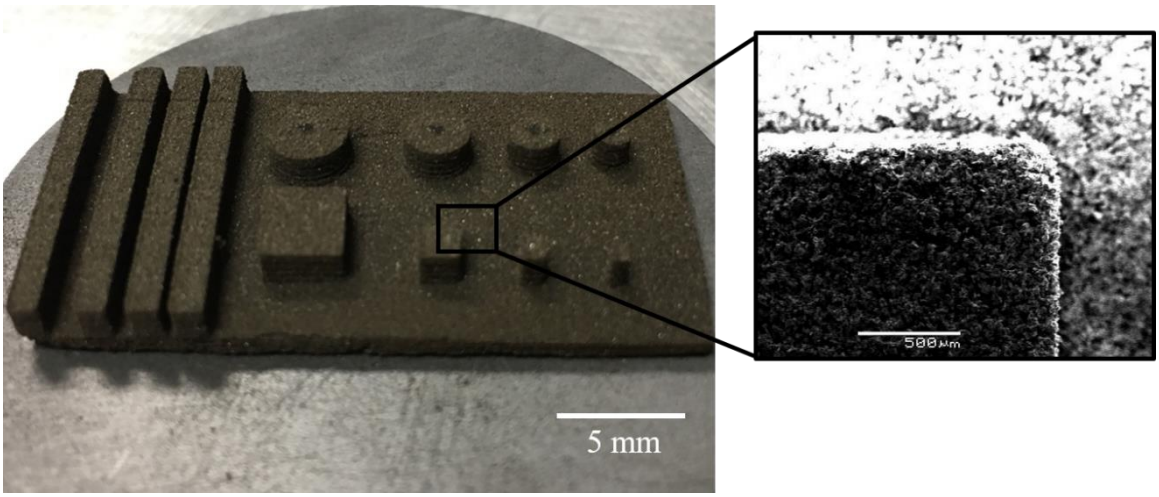


**(b)**

Figure 4.5. Printed test parts using acquired system parameters.

SLS-processed SiC preforms normally show high degree of porosity after post-curing. Therefore in order to further reduce porosity and enhance structural integrity, these SLS-processed parts were infiltrated with silicone dissolved in xylene. After drying out the xylene, the silicone-infiltrated parts showed much higher degree of bonding with very low porosity as shown in Figure 4.6 due to high adhesion strength of silicone. Decomposition of Si-O-C bond in silicone above 1400 °C in an inert atmosphere leads to the formation of SiO and $SiO_2$, which can further react with carbonized binder to form secondary SiC during high-temperature furnace sintering. Therefore, silicone resin was found to be useful for creating thick coatings, micro parts and precision ceramics, which may be difficult to obtain from pyrolysis of simple organic precursors without additives. Pre-infiltration of silicone can eliminate the liquid silicon infiltration process so that the final part can maintain the structural resolution achieved from micro SLS process. More study will be conducted on the feasibility of silicone as a transient binder for SLS-processed SiC preforms.

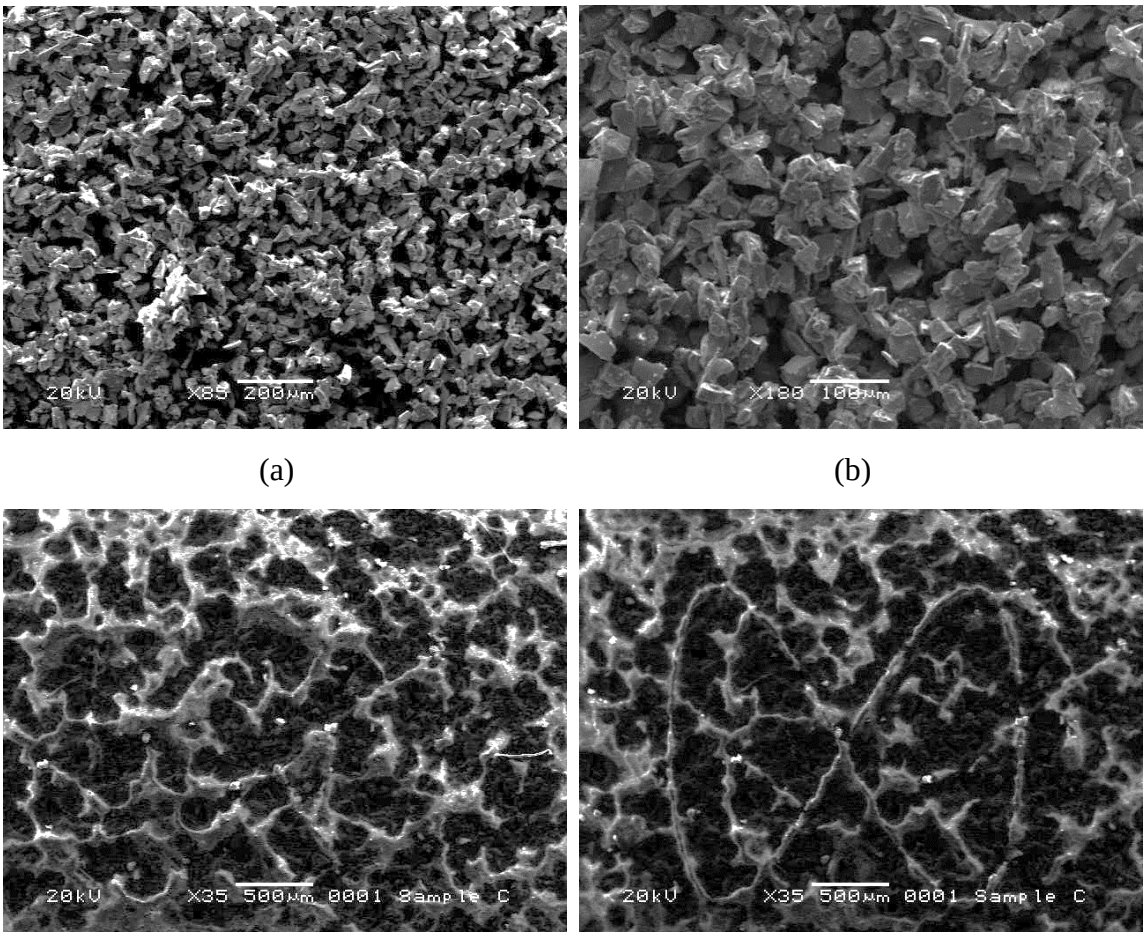


Figure 4.6. SEM views of SiC preforms before and after silicone infiltration.

SEM surface images taken of the SiC preforms in Figure 4.6 (a) and (b) also confirm that the phenolic binders between the SiC particles have been converted to carbonized ligaments. Porosity of the sintered parts was estimated using the SEM images incorporated with image processing in Matlab® (Appendix – B). The SEM images taken from the polished surface of the sintered parts were enhanced with pixel-classification to

generate a porosity threshold image, which separates the porosity voids from the rest of the sintered particles as shown in Figure 4.7. The resulting porosity of the sintered parts was measured to be around 20% with average pore size of 10 – 20 μm according to the processed images in different resolutions.

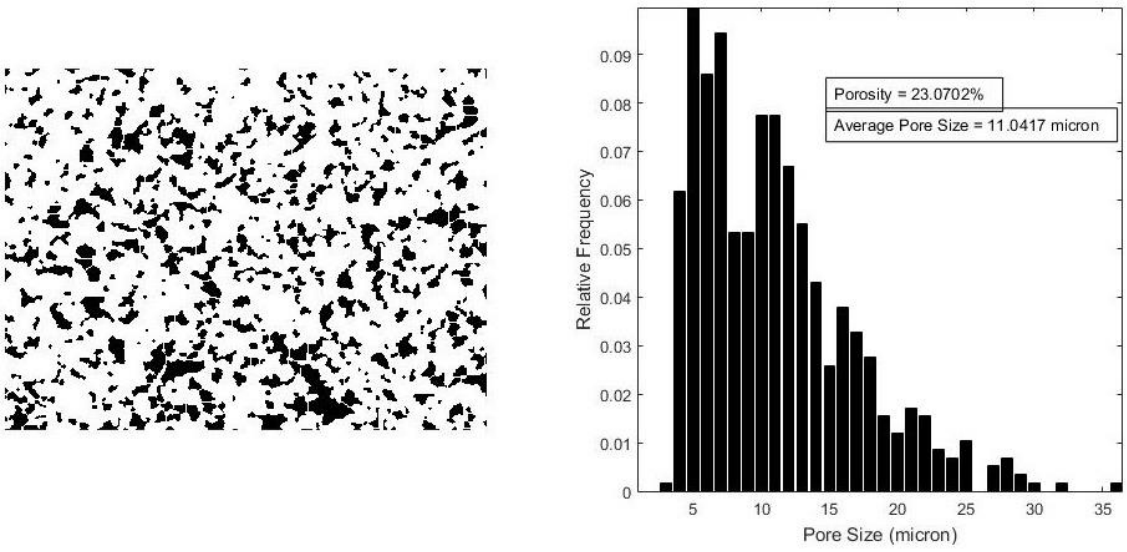


(a)

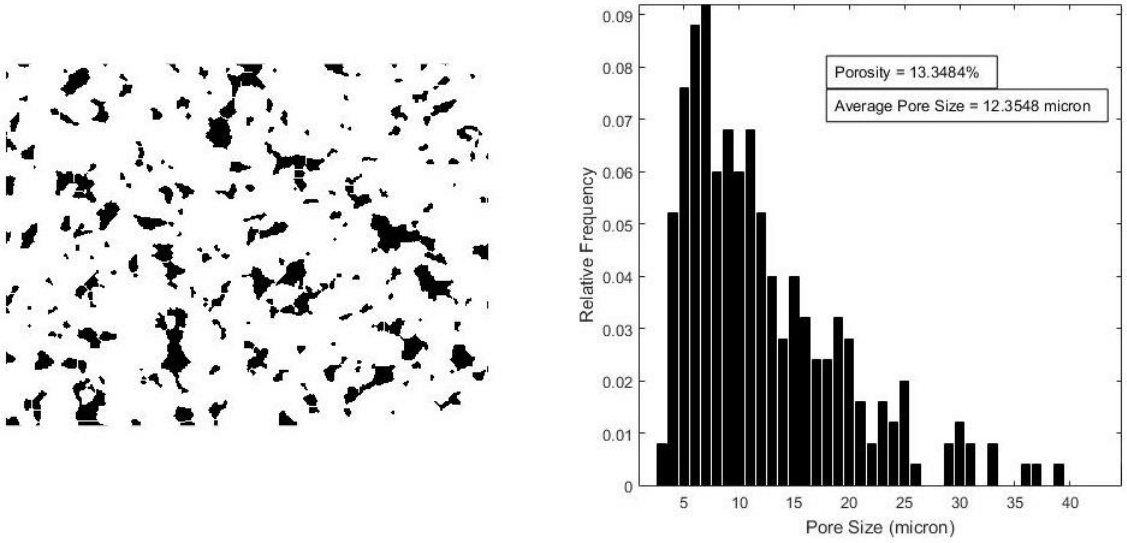


(b)

Figure 4.7. Pixel-classified SEM images to estimate the porosity of the SiC preforms.

### 4.3 Furnace Sintering and Post-Processing Infiltration

Furnace sintering with silicon infiltration was conducted in a high-temperature graphite vacuum furnace with the following temperature profile: 180 °C/h from room temperature to 200 °C, 30 °C/h to 500 °C during which the phenolic binder decomposes and is carbonized, 300 °C/h to 1400 °C, 500 °C/h to 1650 °C during which silicon infiltration occurs, and the furnace is cooled immediately. Cooling time was about 7 – 10 hours. The furnace was filled with argon gas and then to vacuum before heat treatment started. Small amount of feeding of argon can sweep away the gasified byproducts from decomposition and carbonization of the binder materials and other chemical reactions during the process.

SEM images taken of the surface of the silicon infiltrated parts confirm that the resulting parts are Si-SiC composites with full density as shown in Figure 4.8. Around the α-SiC, the starting powder, a dark grey border of SiC can be seen. The secondary SiC is a result of the reaction between the liquid silicon and the carbon from decomposed binders during post-processing infiltration.

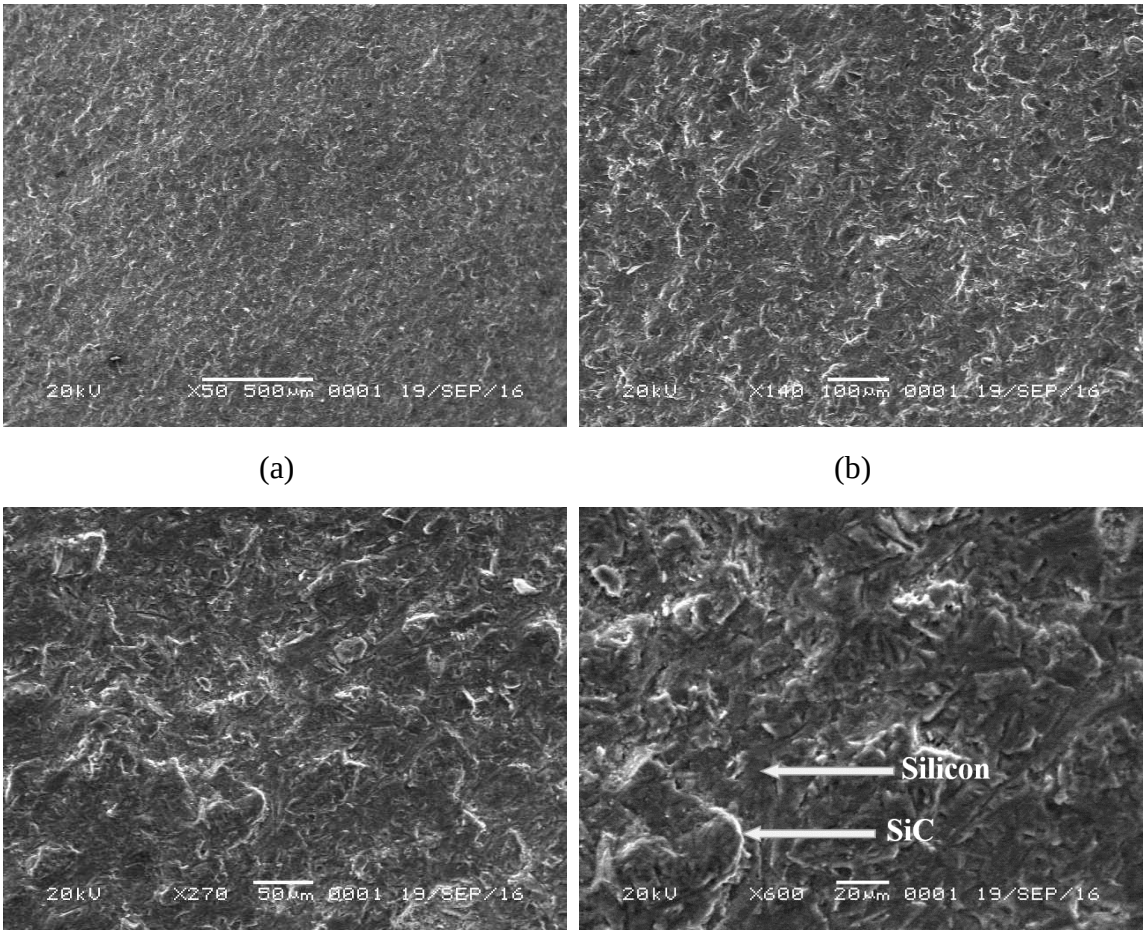


Figure 4.8. SEM views of silicon-infiltrated parts.

Micro SLS process was developed specifically for the generation of SiC preforms in order to achieve complex geometry and micro-scale resolution while maintaining structural integrity. Moderate laser power with low scanning speed leads to melting and partial crosslinking of polymer binders, which eliminates the need for heated powder bed, inert gas or vacuum environment, and post-curing processes for binder materials. For

current system settings, average laser power in the range of 2.5 – 2.7 W and scan speed in the range of 50 – 60 mm/s produced the best results in terms of bonding strength and structural resolution. For SiC powders with APS of 100, 30, and 20 μm, structural resolutions as small as 200, 100, and 50 μm have been achieved although removing unsintered powders after SLS processing still poses a big challenge. Smallest featuring resolution was found to be at least 2 – 3 times larger than average particle size of the structural material. Silicone has been successfully used as a transient binder, which could maintain structural integrity during phenolic softening as well as provide additional silicon for the formation of secondary SiC during high-temperature furnace sintering.

# Chapter 5: Laser Reaction Sintering of SiC from Si-C Composite

In this chapter, laser reaction sintering of SiC from a slurry mixture of silicon and carbon is investigated. Slurry-based coating is also introduced, which is capable of creating more coherent and compact, micro-size layers compared to the powder-based coating.

Liquid silicon infiltration (LSI) of porous carbon preform leads to the formation of SiC without additional sintering aids. It has become a low-cost and reliable method to produce SiC components of complex structure and high density. Empirical study shows that the LSI process starts with molten silicon driven by the capillary force to fill the pores of the carbon preform, and then the liquid silicon encases the carbon followed by reactive wetting to form SiC due to the reduction in surface energies of both the liquid silicon and solid carbon [72,73]. Similar liquid-solid reactions occur when the solid carbon is dissolved into the liquid silicon [74]. This exothermic reaction can be formulated as follows:

$$\mathrm{Si\ (l)} + \mathrm{C(s)} \xrightarrow{T \geq T_M} \mathrm{SiC(s)} \tag{5.1}$$

where $T_M$ is equal to 1414 °C, which is actually the melting temperature of silicon.

It is imperative to precisely control reaction parameters such as carbon microstructure and pore size, silicon infiltration temperature, and the structure and geometry of the carbon preforms. Experimental studies on the reaction mechanism at the liquid silicon and solid carbon interface show that an interfacial SiC layer can be formed within 1 minute, which can grow to a maximum layer thickness of 10 μm within 30

minutes. The SiC layer then acts as a diffusion barrier preventing further reaction as the process transforms from reaction driven to carbon diffusion limited [75,76]. Based on the phase distribution and structural changes, the reaction can be described with six stages including (I) liquid silicon infiltration through the carbon preform, (II) dissolution of carbon, (III) formation of SiC at the liquid-silicon interface, (IV) continuous growth of the layer to about 10 μm, (V) carbon diffusion through this layer, (VI) development of long, thin silicon-filled cracks within the continuous SiC matrix. Therefore, the reaction is expected to be completed in stage (V), which takes about 120 minutes in total [77]. It is also shown that liquid silicon readily wets solid carbon, which can be further accelerated by the presence of the reaction product SiC at the interface and triple line region [78,79].

Various simulation models describing the formation of SiC by LSI process have been developed in order to further understand the wetting reaction dynamics. Nelson and Colella developed a two-dimensional model to examine the effects of initial porosities, pore size, and reaction rates on silicon infiltration dynamics [80]. More sophisticated models using Darcy's law and Poiseuille's law, etc. have also been developed, which showed excellent agreement with the experimental results that liquid silicon flux declines exponentially with increasing infiltration depth. Consequently, newly formed SiC at the interface works as a diffusion barrier effectively halting further reaction between liquid silicon and solid carbon [75,81].

## 5.1 EXPERIMENTAL

### 5.1.1 Slurry-Based Coating

Commercial crystalline, amorphous silicon powder with average particle size of 1 – 20 μm and purity of 99.9985% (metal basis), and natural, microcrystal grade graphite powder with average particle size of 2 – 15 μm and purity of 99.9995% (metal basis) from Alfa Aesar® were used as the processing powder. The density of silicon powder was 2.33 $g/cm^3$ and the density of carbon powder was approximately 2 $g/cm^3$. These two powders were mixed in weight ratio of 1.16:1 and then were blended in ethanol to form slurry. Compared to the powder mixing process, which typically takes a few hours, slurry mixing only took a few minutes due to the high efficiency of liquid-based blending. Then, the slurry was coated on top of a graphite plate where all dispersant evaporated quickly in atmosphere, leaving a powder layer of 20 μm in thickness. As shown in Figure 5.1, slurry-based coating formed more compact and coherent powder packing compared to the powder-based coating used in conventional SLS systems.

Figure 5.1. Powder-based coated layer versus slurry-based coated layer.

## 5.2 Results and Discussion

When a focused, pulsed laser beam was guided to the powder bed, silicon melts into liquid followed by the wetting reaction with adjacent carbon particles to form SiC. As the reaction time is much shorter than that of furnace sintering, incomplete reaction leads to formation of Si-SiC-C matrix bonded by solidified silicon and SiC. A range of 2 – 10 W laser power was tested on the slurry-coated layer and the results are shown in Figure 5.2. Laser power of below 3 W seems insufficient to melt silicon at any scan speed in the range of 5 – 100 mm/s. On the other hand, when the laser power is higher than 8 W, the sintered lines tend to break apart as shown in Figure 5.2 (c) and increasing scanning speed seems not enough to inhibit the cracks. It is possibly due to the recoil effect of the laser beam that when the first laser pulse hits the powder, it creates a cloud above the powder bed consisting of evaporated particles and formed plasma. When the subsequent laser pulse passes through this cloud, it carries along some of them, which becomes a force momentum towards the powder bed. This effect has actually been used to suppress the balling effect

of individual particles during laser melting or sintering of powder materials whereas excessive laser power can cause cracks in the layer.

When the scanning speed is below 5 mm/s, the sintered layer tends to bend and warp as shown in Figure 5.2 (d) and (e). It is mainly due to the temperature gradient between the top and bottom surface of the layer. This effect was further aggravated at slow scanning speed and low laser power because high laser power can suppress the bending and warping in some degree while fast scanning speed is minimizing formation of temperature gradient during sintering as mentioned above. As most metal and ceramic laser sintering process involves very high temperature, this phenomenon has been well studied and currently, the best solution in industry is the replacement of baseplate made of a compatible material so that the sintered layer would bond to the baseplate to inhibit distortion in all degrees. However, it can also be suppressed by proper selection of system parameters such as laser power , repetition rate, beam spot size, scanning speed, etc. as shown in Figure 5.2 (b).

For the next step, laser sintering of multiple layers were attempted in order to investigate the possibility of additive manufacturing of SiC via this process. The range of laser system parameters were selected based on the previous experiments that produced a fine, solid single layer. The center piston was lowered by 50 μm and then the slurry feeder delivers another layer of slurry on top. Since a very small bending or warping of the first layer can cause disruption in delivery of succeeding layer, some were carried out manually

by depositing a few drops of slurry on to the first layer. When more than two layers were attempted to be sintered, the layers all tend to crack as shown in Figure 5.2 (f). It is mainly because the newly formed Si-SiC-C matrix layer is not strong enough to overcome residual stresses by temperature gradient during laser sintering. In addition, accumulated distortion of multiple layers would accelerate cracking of the layers. Therefore, in order to accomplish sintering of multiple layers, it is imperative to create stronger bonding among particles and layers during laser sintering and also to use a compatible baseplate so that sintered layers would stick to the baseplate, preventing distortion of layers.

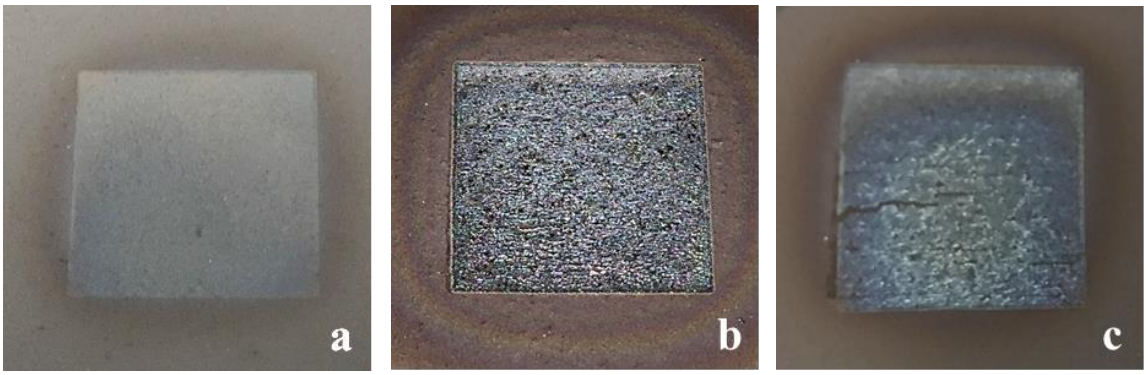


Laser Power = 2 W
Scan Speed = 50 mm/s

Laser Power = 5 W
Scan Speed = 50 mm/s

Laser Power = 10 W
Scan Speed = 50 mm/s

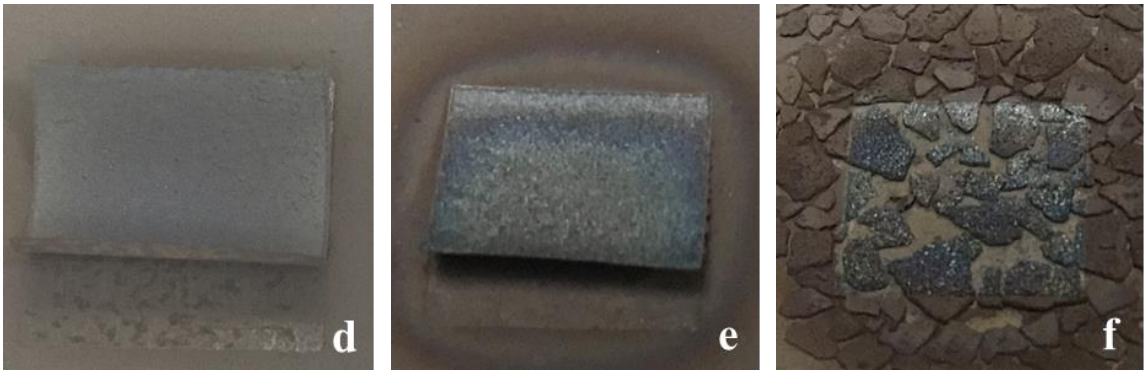


Laser Power = 2 W
Scan Speed = 5 mm/s

Laser Power = 5 W
Scan Speed = 10 mm/s

Laser Power = 5 W
Scan Speed = 50 mm/s

Figure 5.2 Sintered layers of Si -C mixture at different laser power and scan speed.

Figure 5.3 shows the SEM images of sintered layers of Si-SiC-C matrix composite. Overall, the sintered layer shows a fine surface with some abnormally large particles embedded in it. As shown in Figure 5.3 (a), some regions exhibit a certain degree of cracks due to the high residual stresses among particles as mentioned above. Figure 5.3 (b) and (c) present formation of SiC from molten silicon encasing adjacent carbon particles.

However, as wetting reaction creates new particles, they tend to form individual clumps and are bonded loosely to each other as shown in Figure 5.3 (d). Since silicon and carbon powder are mixed in 1:1 volumetric ratio, the wetting reaction may consume more silicon as it needs to encase carbon particles, which can cause lack of liquid silicon to create a melt pool in laser-scanned region. Therefore, a further study needs to be conducted in order to find the ideal ratio of silicon and carbon to not only complete the wetting reaction but also consolidate the Si-SiC-C matrix.

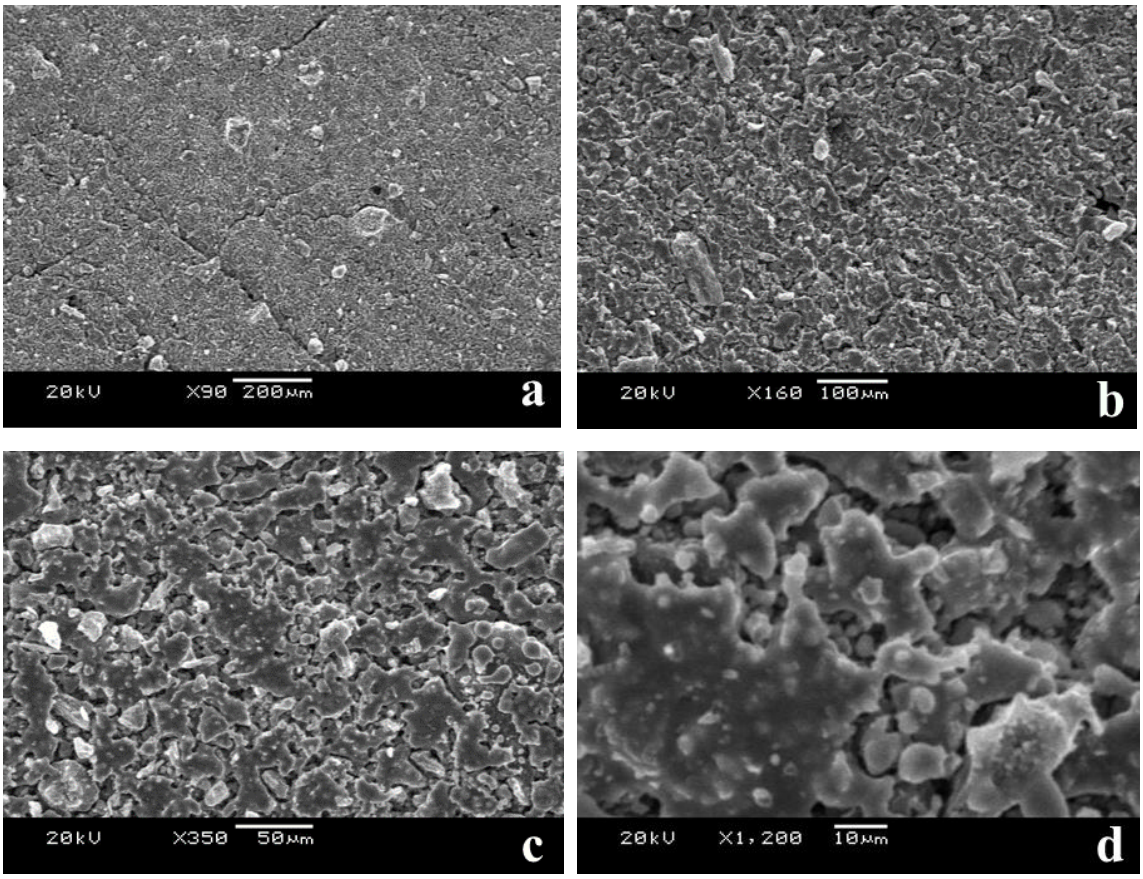


Figure 5.3. SEM images of laser-sintered layer of Si-SiC-C matrix.

In summary, generation of SiC from a slurry-based mixture of silicon and carbon was attempted by using high-frequency, pulsed laser as heat source. Slurry-based coating exhibits advantages over powder-based coating in terms of layer thickness, powder coherence and compactness. Wetting reaction between liquid silicon and carbon occurred when liquid silicon encases adjacent carbon particles to form β-SiC as expected. As silicon consolidates, formation of Si-SiC-C matrix composite was observed but the inter-particle bonding was not strong enough to hold the structure or to support successive layers.

Sintering of multiple layers has not been successful due to the accumulated residual stresses by temperature gradient that eventually crack the layers. Therefore, although laser reaction sintering of Si-C composite is able to generate a single-layer Si-SiC-C matrix composite, some improvements such as design of compatible baseplate, enhancement of production time, porosity control are needed to enable the fabrication of multi-layer composites from Si-C system.

# Chapter 6: Selective Laser Sintering of Si-SiC-C Matrix Composite

This chapter describes the material-specific SLS process applied to a Si-SiC-C matrix composite, where silicon and carbon work as sintering aids. Due to the large energy input of the laser radiation and the interaction with micro size particles, problems like balling, sublimation, residual stresses, recoil effect, and layer deformation occur. These phenomena and resulting effects are discussed and the process optimization is described.

## 6.1 Balling Effect

As the particle size of processing powder gets smaller down to micro scale, balling effect, which is an undesirable defect associated with direct laser sintering or melting, becomes more severe due to the increased surface tension against gravity. Note that this balling effect is different to the technical term “balling” used in additive manufacturing that involves large scale balling among multiple particles. Low laser power coupled with low scan speed results in the formation of highly coarsened balls as shown in Figure 6.1 (a), which is described as the “balling” effect in conventional SLS processes. It is mainly caused by the limited formation of liquid and delayed cooling of the melt at a low laser power input. A new type of balling is characterized by a large amount of micro-scale balling on the sintered surface as shown in Figure 6.2 (b). This formation is ascribed to insufficient time for bonding and necking among particles at a high scan speed. Increasing input of energy density by increasing laser power and lowering scan speed can decrease the tendency of balling. In addition, application of a q-switched laser instead of a

continuous wave laser can further reduce the balling by the recoil force generated from the laser pulses with high energy density.

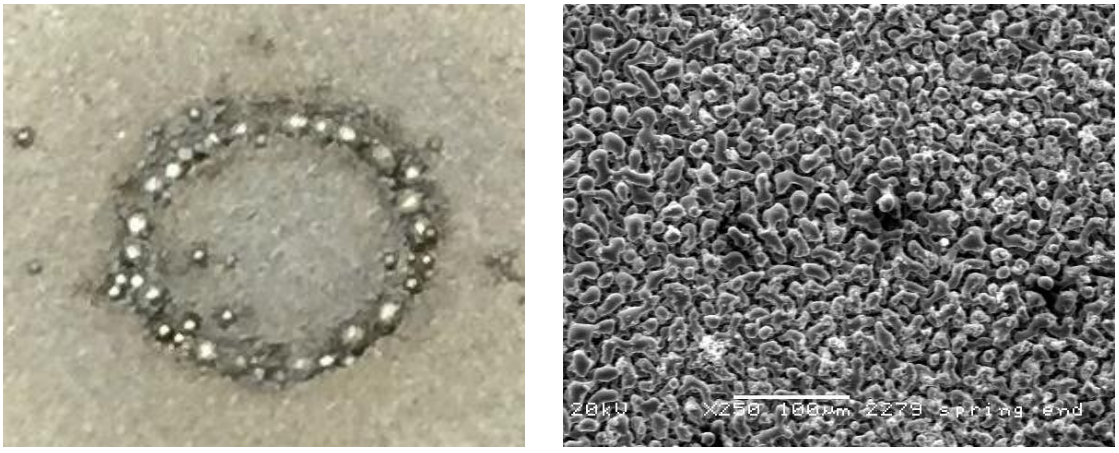


(a) (b)

Figure 6.1. Demonstration of highly coarsened balling (a) due to a low laser power and micro-scale balling (b) occurred at a high scan speed.

In order to better understand the behavior of micro-size silicon particle in liquid phase, a numerical model of a spherical droplet on a wetting or non-wetting substrate was developed based on the following equation by Bashforth and Adams [82].

$$\frac{\frac{\partial^2 z}{\partial x^2}}{\left[1+\left(\frac{\partial z}{\partial x}\right)^2\right]^{\frac{3}{2}}}+\frac{\frac{\partial z}{\partial x}}{x\left[1+\left(\frac{\partial z}{\partial x}\right)^2\right]^{\frac{1}{2}}}=\frac{2}{b}+\frac{\rho g z}{\gamma} \tag{6.1}$$

In this equation, a Cartesian formulation of the Young-Laplace equation was applied to a appoint A(x,z) on the droplet profile where x is the horizontal coordinate at A,

z is the vertical coordinate at A, $\frac{\partial z}{\partial x}$ and $\frac{\partial^2 z}{\partial x^2}$ are the first and second derivatives of z with respect to x at point A. ρ is the density of the liquid, g is the gravitational acceleration, γ is the surface tension of the liquid, and b is the radius of curvature at the origin, which is located at the apex of the droplet.

The density of liquid silicon is 2329 kg/m$^3$ and the surface tension of silicon is assumed to be a constant value of 0.732 N/m based on the measurement by Millot and Shishkin [83,84]. By numerically solving the above-mentioned second order differential equation, x and z coordinates of the particle can be obtained (Appendix – C). The deformation of the molten particle due to the combined effects of surface tension and gravity is shown in Figure 6.2. As the particle size gets smaller, the effect of surface tension becomes more significant and the particle tends to maintain its spherical shape. When the particle size is in micron scale, gravitational effect becomes almost negligible and loose packing of the powder can easily cause individual balling instead of inter-particle wetting and bonding.

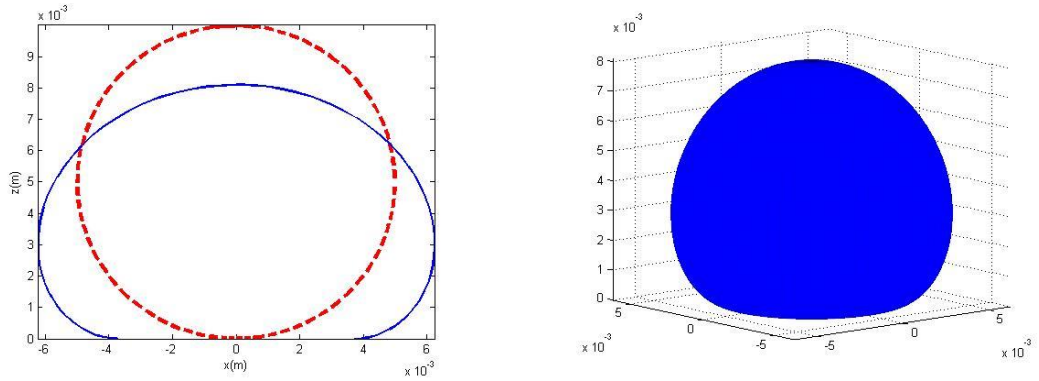


(a)

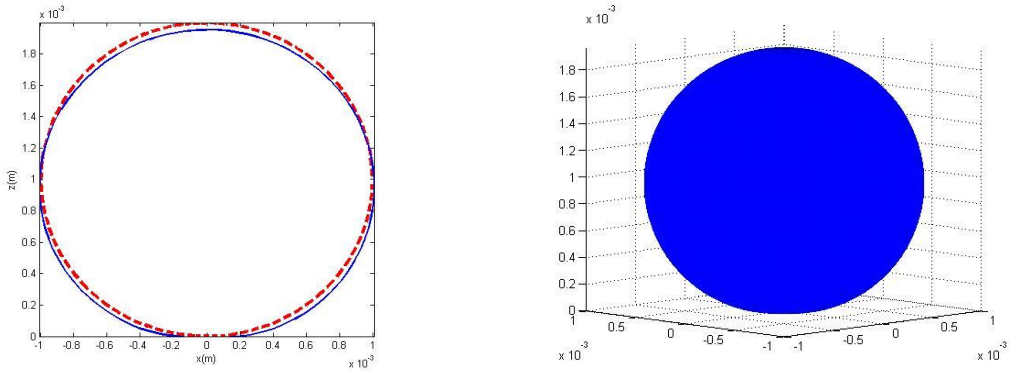


(b)

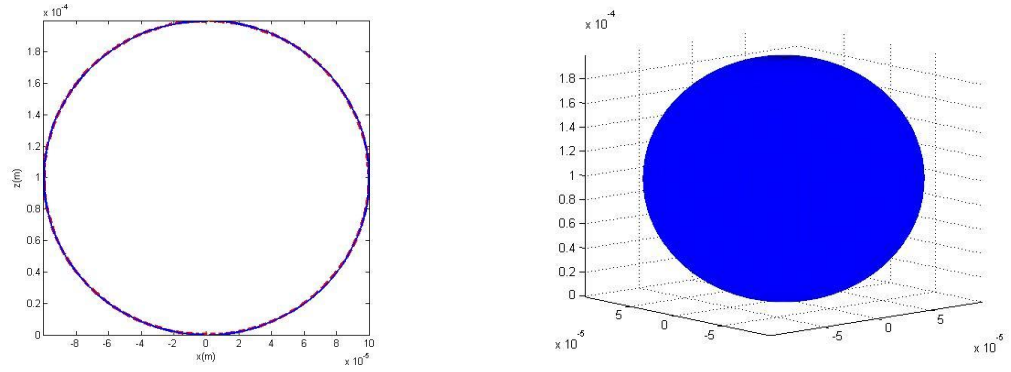


(c)

Figure 6.2. Deformation of liquid silicon particle due to surface tension and gravity. The radii of the droplets are 5 mm (a), 1 mm (b), and 100 µm (c) respectively.

## 6.2 EXPERIMENTAL

### 6.2.1 Powder Preparation

Commercially available α-SiC, silicon and graphite powder (Alfa Aesar® A16601, 38715, 14736, MA, USA) were used as the processing powder. Selected properties of these powder materials are listed in Table 6.1.

Table 6.1. Comparison of properties of the powdered materials

| | **SiC** | **Si** | **C (graphite)** |
|---|---|---|---|
| *Particle size* | Mean 29.2 ± 1.5 µm | 1 – 20 µm | 2 – 15 µm |
| *Density* | 3.16 g/cm$^3$ | 2.33 g/cm$^3$ | 2 g/cm$^3$ (approx.) |
| *Melting point* | 2700 °C (decomposes) | 1423 °C | >2760 °C |
| *Boiling point* | N/A | 2355 °C | N/A |
| *Purity* | 99.8% | 99.9985% | 99.9995% |

These three materials were mixed in different volumetric ratios in order to understand the effect of silicon and carbon during SiC sintering as well as to find ideal compositional ratio that yield best results in terms of bonding strength and minimum porosity for structural integrity. The powder compositional ratio is listed on Table 6.2. These powders were blended with alumina grinding media to break agglomerated particles and facilitate the process.

Table 6.2. Si-SiC-C powder composition used for SLS processing

| *Composition* | ***SiC*** | ***Si*** | ***C*** |
|---|---|---|---|
| ***Composition 1*** | 100 wt.% | - | - |
| ***Composition 2*** | 86 wt.% | 6.5 wt.% | 7.5 wt.% |
| ***Composition 3*** | 73 wt.% | 12.5 wt.% | 14.5 wt.% |
| ***Composition 4*** | 61 wt.% | 18 wt.% | 21 wt.% |
| ***Composition 5*** | 50 wt.% | 23 wt.% | 27 wt.% |

### 6.2.2 Selective Laser Sintering of Si-SiC-C

Direct selective laser sintering was carried out at high vacuum environment. Layer thickness of 100 μm was used for the sintering experiments and powder compaction process was applied during the powder coating. Since the ceramic sintering is typically a long process, moderate laser power in the range of 2 – 20 W and low scan speed of 1 – 100 mm/s were tested. Assuming Gaussian beam profile ($TEM_{00}$), the final laser beam spot size can be calculated as follows:

$$D = \left(\frac{4\lambda}{\pi}\right)\left(\frac{F}{D}\right) \tag{5.1}$$

where $\lambda$ = 1064 nm is the wavelength, F = 80 mm is the focal length of the F-theta lens, D is the output diameter of the laser beam. Taking into account of the beam quality factor $M^2$ = 2.0 of the current laser, and the unfocused beam waist diameter of 22.5 mm, the laser beam can be focused down to 10 μm. Laser spot size can be adjusted by moving

the galvo scanner in vertical direction via elevation stage. Considering the primary particle size of the Si-SiC-C powder, the laser beam spot size on to the probe was adjusted to 100 μm. Scan spacing was set to be the same as the beam spot size. For this study, pulse repetition frequency was fixed at 100 kHz and the study was focused on the effects of laser power and scanning speed.

### 6.3 Results and Discussion

For initial sintering tests, technically pure SiC powder was sintered in vacuum with the q-switched laser. The only recognizable effect was the decomposition and oxidation of the material. When the laser power and scanning speed were lower, oxidation became more severe. Therefore, without a binder material in the powder or some sintering aid to activate liquid phase sintering, laser radiation is fully absorbed by SiC, resulting in dissociation into silicon and carbon. Free silicon would be oxidized and subsequently work as a binder material to loosely bond adjacent SiC particles. However, the bonding mechanism seems to be not strong enough to hold the structure as reported by various articles. Therefore, presence of binder material or sintering aids seems essential for direct laser sintering of SiC.

Average laser power in the range of 2 – 20 W and scan speed in the range of 1 – 100 mm/s were investigated in order to find the ideal power intensity and scan speed at fixed beam spot size and repetition frequency. When the laser power is too high (>10 W), “recoil effect” became dominant and the laser pulses tend to ablate the powder instead of

sintering or melting it. On the other hand, low laser power (<4 W) associated with low scan speed results in balling and incomplete bonding among particles. When the scanning speed is below 5 mm/s, highly coarsened balling coupled with severe oxidation were observed. For the current system, average laser power of 5 W coupled with scan speed of 10 mm/s delivered the best results in terms of bonding strength and minimal oxidation and porosity.

Laser sintering of the other four ingredients of Si-SiC-C powder composite systems were also conducted in high vacuum. Particle bonding was formed by direct SLS of the deposited powder layer as shown in Figure 6.3. All four of the powder mixtures showed a certain degree of bonding, but when the content of silicon and carbon is very low (composition 2), the necking among particles were not strong enough for inter-particle bonding. On the other hand, presence of excessive amount of silicon and carbon (composition 5) results in higher porosity of the layer as shown in Figure 6.3 (left). Among the four ingredients of powder mixture, the powder composition 3 with 12.5 wt.% of silicon and 14.5 wt.% of carbon showed highest degree of bonding with minimal porosity as shown in Figure 6.3 (right).

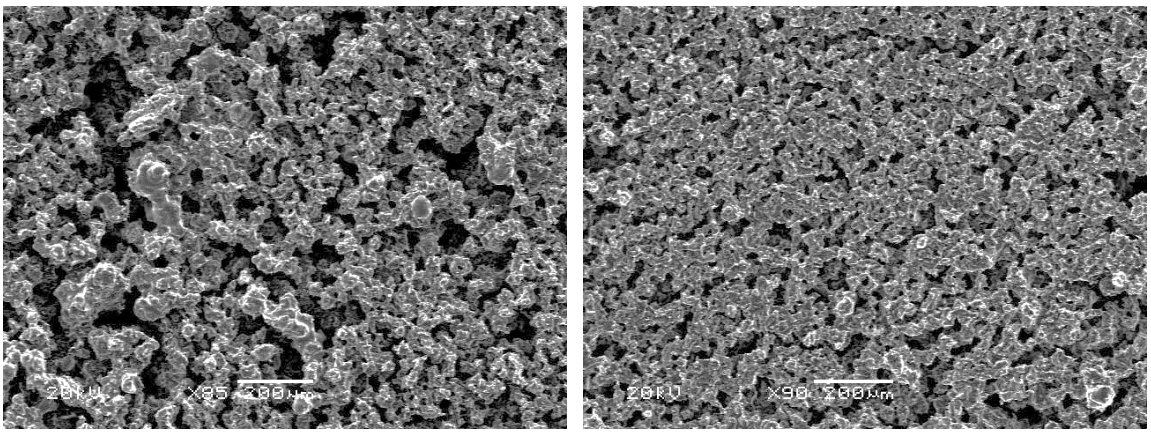

Figure 6.3. SEM views of SLS-processed Si(20 vol.%)-SiC(60 vol.%)-C(20 vol.%) mixture on the left and Si(10 vol.%)-SiC(80 vol.%)-C(10 vol.%) mixture on the right.

SEM views of the sample sintered at average laser power of 5 W and scan speed of 10 mm/s are presented in Figure 6.4. Metallographic observations confirmed the wetting by silicon between SiC particles all-through the samples. The sintered layer exhibited increased porosity due to oxidation and subsequent gasification of carbon particles, which actually prevents oxidation of silicon and SiC particles in return. Therefore, well-controlled amount of silicon and carbon may facilitate the liquid-phase sintering, prevent oxidation and dissociation of SiC, and reduce porosity.

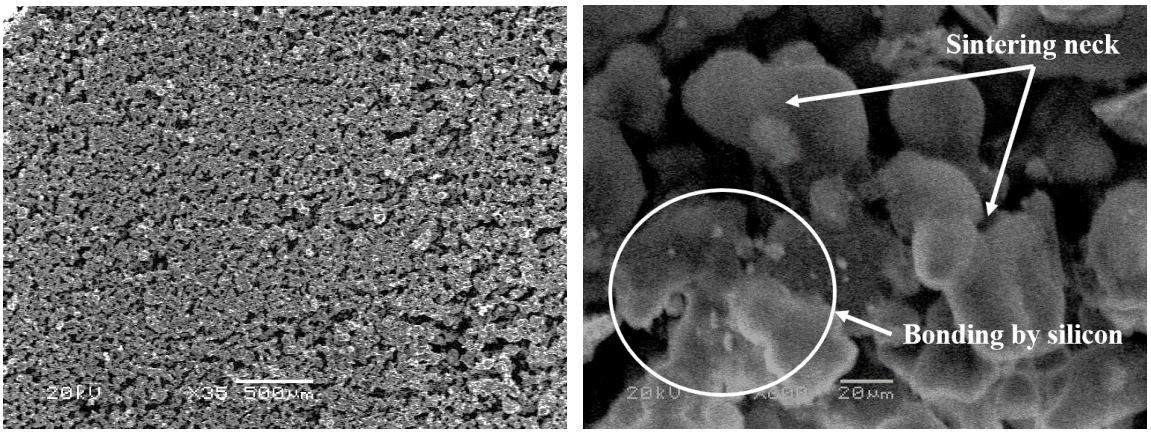


Figure 6.4. SEM views of sintered Si-SiC-C surface using laser power of 5 W and scanning speed of 10 mm/s.

SLS of multiple layers has been attempted in order to investigate the layer-to-layer bonding mechanism of the Si-SiC-C composite. Powder mixture of SiC (80 vol.%) + Si (10 vol. %) + C (10 vol.%) was used for the sintering tests. Laser sintering or melting of metallic and ceramic powders involve extremely high temperature, resulting in severe bending and warping of layers due to high residual stresses. Therefore, a net-shaped structure was used as the scanning pattern in order to prevent severe cracking of the final part due to the deformation of the layers. Since the primary particle size of current powder is in the range of 1 – 30 μm, the powder layer thickness was selected to be 100 μm and powder compaction ratio of 10 vol.% was applied to reduce porosity. Consecutive SLS of up to 50 layers were attempted for different shapes as shown in Figure 6.5. As expected, layer-to-layer bonding by pulsed laser radiation was observed after the unsintered powder was washed away by alcohol. No cracking occurred in the sintered sample, but

accumulated bending of each layer results in a certain degree of deformation of the final parts.

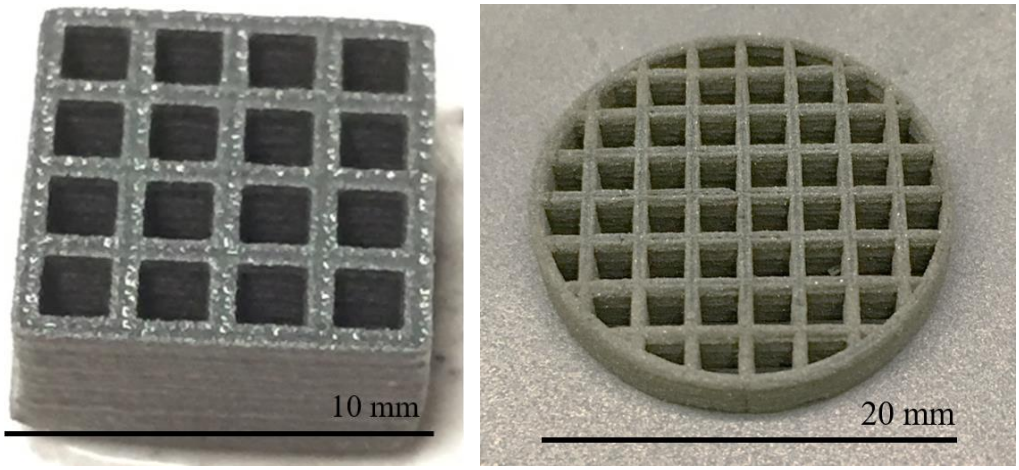


Figure 6.5. Sintered sample of Si-SiC-C with 50 layers of 100 µm layer thickness.

The SEM images taken from the polished surface of the sintered parts were processed the same way as in Chapter 3 to calculate the porosity and the average pore size of the sintered part as shown in Figure 6.6. The resulting porosity of the sintered parts was measured to be 30 - 40% with average pore size of 10 – 20 µm according to the processed images in different resolutions.

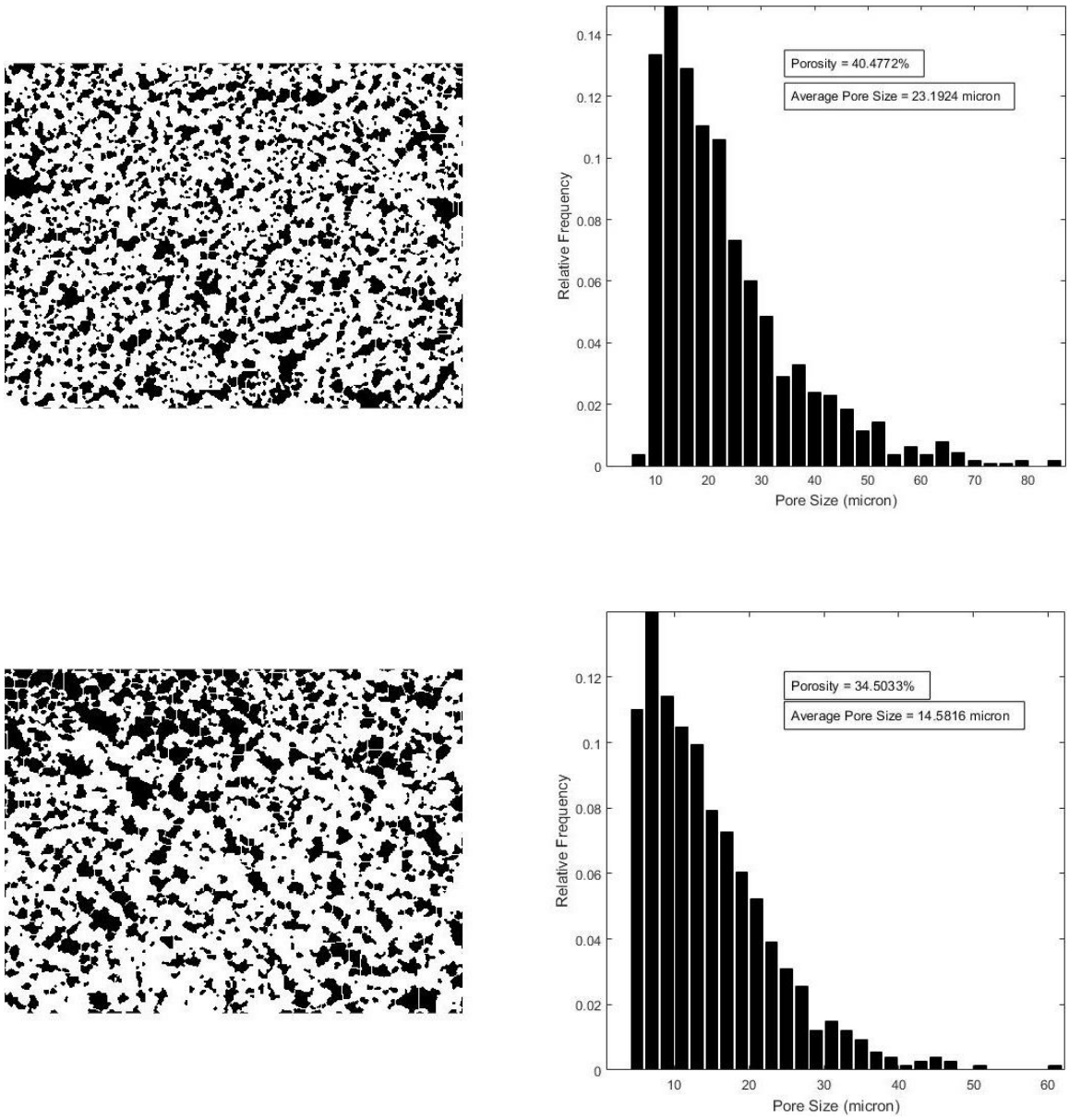


Figure 6.6. Pixel-classified SEM images to estimate the porosity of the sintered part.

Black areas indicate pores.

In the course of this feasibility study, selective laser sintering has been applied to the Si-SiC-C matrix composites, where silicon and carbon function as sintering aids. Application of high-power-intensity, high-frequency laser pulses onto the Si-SiC-C powder mixture led to the formation of solid Si-SiC-C composite. Effect of silicon and carbon as sintering aids for selective laser sintering of SiC was investigated. Lower content of silicon resulted in weak bonding whereas excessive presence of carbon led to severe oxidation and higher porosity. Due to the large energy input from the laser and the interaction with micro size particles, problems like balling, sublimation, and layer deformation occurred in different levels. The process parameters were optimized to minimize these detrimental effects. Powder compaction system was applied to increase the packing density of the powder bed, and thus reduce porosity. Direct SLS of multiple layers has also been achieved with a layer thickness of 100 μm. Microstructure of the sintered parts showed liquid-phase bonding by silicon among SiC particles through-out the sintered region. Porosity of the resulting parts obtained from the optimized processing parameters was measured to be 30 – 40% with average pore size of 10 – 20 μm using enhanced SEM images with pixel-classification.

Based on the above processes and features, selective laser sintering of Si-SiC-C matrix composites is promising for the generation of near net-shape parts with 3D complexity. It also provides an easier way for the fabrication of SiC parts with various materials to improve sinterability. The main weakness of the process resides in the inherent high level of porosity that may require post-processing such as furnace sintering or

metal/ceramic infiltration. For rapid prototyping and manufacturing of SiC composites, production time and porosity control have to be significantly enhanced to enable the direct additive manufacturing of end-products in large scale.

# Chapter 7: Conclusions

This dissertation presents the study of micro selective laser sintering of SiC using different approaches. The main idea was to apply selective laser sintering technology to achieve freeform fabrication of SiC parts with complex geometry and micro scale resolution. It was focused on the development of a new micro SLS system as well as the investigation of different binding mechanisms and sintering aids for the additive manufacturing of SiC precision components.

A simulation model was developed to analyze the interaction between laser radiation and micron-sized powders in microscopic scale. Particle dynamics was used to create a 2D and 3D models of the powder bed. Ray tracing method coupled with inter-particle heat conduction was applied to model the laser-particle and particle-particle interactions during the SLS process. For a predefined laser power and scan period, the relationship between heat-affected regions in all three directions and the particle size was obtained. Monte Carlo algorithm was used by creating multiple powder beds with different particle sizes and configurations in order to numerically find the relationship between the featuring resolution and the average particle size. This model was used to estimate the optimal laser power, scan speed and deposition layer thickness based upon the particle size range of the processing powder.

A new micro selective laser sintering system with micro scale featuring resolution and a new powder coating and compaction system was developed. Ytterbium fiber laser

coupled with the beam expander and the F-theta lens was able to provide pulsed laser beams with high power intensity, high beam quality, and focusable spot size down to 10 μm. Powder coating and compaction system was able to deliver a more compact and coherent powder layer, resulting in lower porosity of the final parts.

A material-specific micro SLS process was developed for the generation of SiC preforms with complex geometry and micro-scale resolution while maintaining structural integrity. Moderate laser power with low scanning speed leads to melting and partial crosslinking of polymer binders, which eliminates the need for heated powderbed, inert gas or vacuum environment, and post-curing processes for binder materials. Structural resolution of 100 μm and featuring resolution of 50 μm have been achieved with optimized system parameters acquired from the model and the experimental results. Smallest featuring resolution was found to be at least 2 – 3 times larger than average particle size of the structural material. Silicone has been successfully used as a transient binder, which could maintain structural integrity during phenolic softening as well as provide additional silicon for the formation of secondary SiC during high-temperature furnace sintering. Post-processing silicon infiltration was able to produce reaction-bonded Si-SiC composites with full density.

Micro selective laser sintering process has also been applied to the Si-SiC-C matrix composites, where silicon and carbon function as sintering aids. Application of moderate laser power (< 5W) and low scan speed (< 50 mm/s) to the Si-SiC-C powder mixture led

to the formation of the Si-SiC-C composite. Effect of silicon and carbon as sintering aids for selective laser sintering of SiC was studied. Lower content of silicon resulted in weak bonding whereas excessive presence of carbon led to severe oxidation and higher porosity. Due to the large energy input from the laser and the interaction with micro size particles, problems like balling, sublimation, and layer deformation occurred in different levels. The process parameters were optimized to minimize these detrimental effects. Powder compaction system was applied to increase the packing density of the powder bed, and thus reduce porosity. Direct SLS of multiple layers has also been achieved with a layer thickness of 100 μm. Microstructure of the sintered parts showed liquid-phase bonding by silicon as well as self-diffusion among SiC particles through-out the sintered region. Porosity of the resulting parts obtained from the optimized processing parameters was measured to be 30 – 40% with the average pore size of 10 – 20 μm.

Due to simplified, cost-effective design with the capability of micro-size featuring, the micro SLS system can be versatile tool for the generation of ceramic preforms that can be further processed to high-resolution microparts.

## 7.1 Future Work

This dissertation focuses on the design of the micro SLS system and the feasibility of the system for the freeform fabrication of SiC preforms and composites with high resolution and structural integrity. The remaining tasks require substantial work to investigate the post-processing methods including furnace sintering and silicon infiltration.

More experimental study on the high-temperature furnace sintering is needed in order to find the ideal processing parameters such as decomposition time, rate of heat flow, and sintering temperature that can affect the properties of the final parts. Proper design for the infiltration process can minimize the porosity and prevent over-fill of the parts. Mechanical testing such as tensile test and three-point bending test can provide more information to the suitability of the post-processed SiC parts on the specified application. Production time and porosity control need to be significantly enhanced to achieve the additive manufacturing of SiC end products in a large scale.

# Appendices

# Appendix – A. Matlab Code for SLS Simulation

## SLS_3D_Main.m

```
clear all; close all; clc;
set(0,'defaultaxesfontsize',12);
set(0,'defaultaxesfontname','times');
set(0,'defaultaxeslinewidth',1);
set(0,'defaultaxesbox','on');
set(0,'defaulttextfontname','times');
set(0,'defaulttextfontsize',12);
set(0,'defaulttextlinewidth',1);
set(0,'defaultlinelinewidth',2);
set(0,'defaultlinemarkersize',10);
warning off;

global Np Esi vsi Ec x1 x2 y1 y2 z1 z2 rho_si grav
%parameters
%min and max powder size in um
tic;
Dpmin = 2;
Dpmax = 2;
Dpavg = 2;
rpmin =Dpmin/2;
rpmax = Dpmax/2;
rpavg = Dpavg/2;
grav = 9.81; % gravity
rho_si = 2.329; %density of Silicon
Np = 10000; %number of particles
psic = 0.8; % volume percentage of SiC particles in the mixture
pcarbon = 0.1; % volume percentage of carbon in the mixture
psilicon = 0.1; % volume percentage of silicon in the mixture
Nsic = floor(Np*psic); % number of SiC particles
Ncarbon = floor(Np*pcarbon); % number of carbon particles.
Nsilicon = Np - Nsic - Ncarbon; % number of silicon particles.

% square boundary:
x1 = 0; y1 = 0; z1 = 0;
x2 = 40; y2 = 40; z2 = 40;
kk = 1.5;
phi = 0:0.1:2*pi;
% create constrained cube
nspace = 500;
X = linspace(x1, x2, nspace);
Y = linspace(y1, y2, nspace);
Z = linspace(z1, z2, nspace);
rx = ones(1,nspace);
nmesh = 20;
% meshes of spheres:
Xs = zeros(nmesh+1,nmesh+1,Np);
Ys = zeros(nmesh+1,nmesh+1,Np);
Zs = zeros(nmesh+1,nmesh+1,Np);
```

```
% Centers of spheres:
r = rpmin + (rpmax-rpmin)*rand([Np,1]); % radius of spheres
xc = x1+r+(x2-x1-2*r).*rand([Np,1]);
yc = y1+r+(y2-y1-2*r).*rand([Np,1]);
zc = (z2-z1)*ones(Np,1);
zc(1) = r(1);
dd = 0.01; % increment of drop
[x,y,z] = sphere(nmesh); % create a 3d mesh of a unit sphere
%transfrom from Cartesian to Spherical Coordinates to define radius
[alpha, beta, rs] = cart2sph(x,y,z);


%{
%Initial Plot before drop in 2D
Xs2d = zeros(Np,length(phi));
Ys2d = zeros(Np,length(phi));
Zs2d = zeros(Np,length(phi));

figure1 = figure (1);
plot(X,z1*ones(1,nspace),'b',x1*ones(1,nspace)...
    ,Z,'b',x2*ones(1,nspace),Z,'b','linewidth',2);
xlabel('X');
ylabel('Z');
hold on;
for c = 1:Np
    r(c) = Dpmin/2+(Dpmax-Dpmin)*rand/2;
    xc(c) = x1+c*(x2-x1)/(Np+1); %Center of sphere:
    Xs2d(c,:) = xc(c)+r(c)*cos(phi);
    Zs2d(c,:) = zc(c)+r(c)*sin(phi);
    fill(Xs2d(c,:),Zs2d(c,:),'g');
end
%}

% Initial plot in 3D
figure1 = figure(1);
plot3(X,y1*rx,z1*rx,'k', X,y1*rx,z2*rx,'k', X,y2*rx,z2*rx,'k', ...
    X,y2*rx,z1*rx,'k', x1*rx,Y,z1*rx,'k', x2*rx,Y,z1*rx,'k',...
    x1*rx,Y,z2*rx,'k', x2*rx,Y,z2*rx,'k', x1*rx,y1*rx,Z,'k',...
    x2*rx,y1*rx,Z,'k', x2*rx,y2*rx,Z,'k', x1*rx,y2*rx,Z,'k', 'linewidth',4)
axis ([x1 x2 y1 y2 z1 kk*(z2-z1)]);
grid off; hold all;

for c=1:Np
  [xn,yn,zn] = sph2cart(alpha, beta, r(c));
  Xs(:,:,c) = xn+ xc(c);
  Ys(:,:,c) = yn+ yc(c);
  Zs(:,:,c) = zn+ zc(c);
  sphere_mesh = surf(Xs(:,:,c),Ys(:,:,c),Zs(:,:,c));
  set(sphere_mesh,'FaceColor',[0 1 0],'FaceAlpha',1,'EdgeAlpha',0.03);
end

%{
% Particle Dynamics in 2D
Xs2d = zeros(Np,length(phi));
Ys2d = zeros(Np,length(phi));
```

```
Zs2d = zeros(Np,length(phi));
Esi = 0.5*(130+185)*10^-3; % average Young's modulus of silicon
vsi = 0.28; % Poisson's ratio of silicon
Ec = Esi/(2*(1-vsi^2)); % equivalent Young's modulus in one direction
% new coordinates and velocities of the particles
vx = zeros(Np,1);
vy = zeros(Np,1);
vz = zeros(Np,1);
tfinal = toc;
disp(['Particle #',num2str(1),' created. Time elapsed: ',num2str(tfinal)]);
for i=2:Np
 r0 = [xc(i),yc(i),zc(i),vx(i),vy(i),vz(i)];
 ti = 0;
 tf = 2;
 while true
  [t,Rtemp]= ode45(@SLS_3D_Fun,[ti,tf],r0,[],r(1:i),xc(1:i-1),yc(1:i-1),zc(1:i-
1));
  if max(abs(Rtemp(end,4:6)))<0.001
     break;
  else
     r0= Rtemp(end,:);
  end
 end
 xc(i) = Rtemp(end,1);
 yc(i) = Rtemp(end,2);
 zc(i) = Rtemp(end,3);
 vx(i) = Rtemp(end,4);
 vy(i) = Rtemp(end,5);
 vz(i) = Rtemp(end,6);
 tfinal = toc;
 disp(['Particle #',num2str(i),' created. Time elapsed: ',num2str(tfinal)]);
end
%}


%{
%Initial Plot before drop
figure2 = figure (2);
plot(X,z1*ones(1,nspace),'b',x1*ones(1,nspace)...
    ,Z,'b',x2*ones(1,nspace),Z,'b','linewidth',2);
xlabel('X');
ylabel('Z');
hold on;
for c = 1:Np
    r(c) = Dpmin/2+(Dpmax-Dpmin)*rand/2;
    xc(c) = x1+c*(x2-x1)/(Np+1); %Center of sphere:
    Xs2d(c,:) = xc(c)+r(c)*cos(phi);
    Zs2d(c,:) = zc(c)+r(c)*sin(phi);
    fill(Xs2d(c,:),Zs2d(c,:),'g');
end
%}

%{
% Particle Arrangement without Particle Dynamics in 3D
nx = floor((x2-x1)/Dpavg);
ny = floor((y2-y1)/Dpavg);
```

```
nz = floor(((z2-z1)/Dpavg)/2);
Np = nx*ny*nz;
r = rpavg*ones(Np,1);
xc = r; yc = r; zc = r;
ii = 1;
for k = 1:nz
   for j = 1:ny
      for i = 1:nx
         xc(ii) = rpavg + Dpavg*(i-1);
         yc(ii) = rpavg + Dpavg*(j-1);
         zc(ii) = rpavg + Dpavg*(k-1);
         ii = ii+1;
      end
   end
end

% create spheres from coordinates.
for c = 1:Np
   [xn,yn,zn] = sph2cart(alpha, beta, r(c));
   Xs(:,:,c) = xn + xc(c);
   Ys(:,:,c) = yn + yc(c);
   Zs(:,:,c) = zn + zc(c);
 end

figure2 = figure(2);
set(figure2,'Position',[500,500,1000,700]);
plot3(X,y1*rx,z1*rx,'k', X,y1*rx,z2*rx,'k', X,y2*rx,z2*rx,'k', ...
   X,y2*rx,z1*rx,'k', x1*rx,Y,z1*rx,'k', x2*rx,Y,z1*rx,'k',...
   x1*rx,Y,z2*rx,'k', x2*rx,Y,z2*rx,'k', x1*rx,y1*rx,Z,'k',...
   x2*rx,y1*rx,Z,'k', x2*rx,y2*rx,Z,'k', x1*rx,y2*rx,Z,'k', 'linewidth',3)
axis ([x1 x2 y1 y2 z1 (z2-z1)]);
grid off;hold on;

for c = 1:Np
   sphere_mesh = surf(Xs(:,:,c),Ys(:,:,c),Zs(:,:,c));
   set(sphere_mesh,'FaceColor',[0 1 0],'FaceAlpha',1,'EdgeAlpha',0.03);
   %{
   if c <= Nsic
      set(sphere_mesh,'FaceColor',[0 1 0],'FaceAlpha',1,'EdgeAlpha',0.03);
   elseif c > Nsic && c <= Nsic+Ncarbon
      set(sphere_mesh,'FaceColor',[0 0 0],'FaceAlpha',1,'EdgeAlpha',0.03);
   elseif c > Nsic + Ncarbon
      set(sphere_mesh,'FaceColor',[1 0 1],'FaceAlpha',1,'EdgeAlpha',0.03);
   end
   %}
end
%}
%-------------------------------------------------------------------------

%-------------------------------------------------------------------------
%
% Particle Dynamics in 3D
Esi = 0.5*(130+185)*10^-3; % average Young's modulus of silicon
vsi = 0.28; % Poisson's ratio of silicon
Ec = Esi/(2*(1-vsi^2)); % equivalent Young's modulus in one direction
% new coordinates and velocities of the particles
```

```
vx = zeros(Np,1);
vy = zeros(Np,1);
vz = zeros(Np,1);
tfinal = toc;
disp(['Particle #',num2str(1),' created. Time elapsed: ',num2str(tfinal)]);
for i=2:Np
 r0 = [xc(i),yc(i),zc(i),vx(i),vy(i),vz(i)]; % initial position and velocity of
particle i.
 ti = 0;
 tf = 2;
 while true
  [t,Rtemp]= ode45(@SLS_3D_Fun,[ti,tf],r0,[],r(1:i),xc(1:i-1),yc(1:i-1),zc(1:i-
1));
  if max(abs(Rtemp(end,4:6)))<0.01
     break;
  else
     r0= Rtemp(end,:);
  end
 end
 xc(i) = Rtemp(end,1);
 yc(i) = Rtemp(end,2);
 zc(i) = Rtemp(end,3);
 vx(i) = Rtemp(end,4);
 vy(i) = Rtemp(end,5);
 vz(i) = Rtemp(end,6);
 tfinal = toc;
 disp(['Particle #',num2str(i),' created. Time elapsed: ',num2str(tfinal)]);
end

 for c = 1:Np
    [xn,yn,zn] = sph2cart(alpha, beta, r(c));
    Xs(:,:,c) = xn + xc(c);
    Ys(:,:,c) = yn + yc(c);
    Zs(:,:,c) = zn + zc(c);
 end

figure2 = figure(2);
set(figure2,'Position',[500,500,1000,700]);
plot3(X,y1*rx,z1*rx,'k', X,y1*rx,z2*rx,'k', X,y2*rx,z2*rx,'k', ...
    X,y2*rx,z1*rx,'k', x1*rx,Y,z1*rx,'k', x2*rx,Y,z1*rx,'k',...
    x1*rx,Y,z2*rx,'k', x2*rx,Y,z2*rx,'k', x1*rx,y1*rx,Z,'k',...
    x2*rx,y1*rx,Z,'k', x2*rx,y2*rx,Z,'k', x1*rx,y2*rx,Z,'k', 'linewidth',3)
axis ([x1 x2 y1 y2 z1 (z2-z1)]);
grid off;hold on;

for c = 1:Np
    sphere_mesh = surf(Xs(:,:,c),Ys(:,:,c),Zs(:,:,c));
    set(sphere_mesh,'FaceColor',[0 1 0],'FaceAlpha',1,'EdgeAlpha',0.03);
    %{
    if c <= Nsic
        set(sphere_mesh,'FaceColor',[0 1 0],'FaceAlpha',1,'EdgeAlpha',0.03);
    elseif c > Nsic && c <= Nsic+Ncarbon
        set(sphere_mesh,'FaceColor',[0 0 0],'FaceAlpha',1,'EdgeAlpha',0.03);
    elseif c > Nsic + Ncarbon
        set(sphere_mesh,'FaceColor',[1 0 1],'FaceAlpha',1,'EdgeAlpha',0.03);
    end
```

```
    %}
end

print(figure2,'-djpeg','-r300',['SLS_3DSim_',num2str(Np),'_p_',datestr(now,'mm-
dd-yyyy-HH-MM-AM'),'.jpg']);
save (['SLS_Result_',num2str(Np),'_p_',datestr(now,'mm-dd-yyyy-HH-MM-
AM'),'.mat']);
%}
%--------------------------------------------------------------------------

%--------------------------------------------------------------------------
% Ray Tracing Method for Laser Beam
% line = [xo yo zo dx dy dz]
A = 0.6; % Absorption rate
R = 1-A; % Reflection rate
%Create parallel beams in Simplified Gaussian profile:
No = 2000; % initial number of laser beams at r=0
Po = 5; % Average laser power W/sec
tlaser = 0.1; % lasing period
Csi = 710; % Specific heat capacity of silicon J/(kg*K).
To = 300; % Initial temperature of particles
Tmelt = 1414; % melting temperature of silicon in Celsius
f_laser = 50e3; % repetition rate
rbeam = 25; % outer Gaussian radius of the laser beam
lambda = 1064e-3; %wavelength of laser beam
D_lens = 6e3; %(microns) Diameter illuminated on the lens
F_lens = 22e3; %effective focal length of the lens
theta_div = D_lens/F_lens; % Full angle of divergence
wo = 2*lambda/(pi*theta_div); %radius of the beam waist
nc = 25; % number of beam circles
drc = rbeam/nc;
rc = drc:drc:rbeam;
N = zeros(length(rc),1);
for i = 1:length(rc)
   N(i) = floor(No*exp(-rc(i)^2/wo^2));
end
Nbeam = sum(N); % total number of parallel beams
po = zeros(Nbeam,6); %beam profile
Co = [(x2-x1)/2, (y2-y1)/2, z2]; %center of beam circles
theta = [];
rcc = [];
for i = 1:length(rc)
   theta = [theta, 0:2*pi/N(i):2*pi*(N(i)-1)/N(i)];
   rcc = [rcc, rc(i)*ones(1,N(i))];
end

for i = 1:Nbeam
   po(i,:) = [Co(1)+rcc(i)*cos(theta(i)), Co(2)+rcc(i)*sin(theta(i)), kk*z2, 0,
0, -1];
end

Pb = Po/Nbeam*ones(Nbeam,1); % Power carried by each beam
Pbo = Pb;
Pp = zeros(Np,1); %initial power on each particle

figure4 = figure (4);
```

```
set(figure4,'Position',[500,500,1000,800]);
plot3(X,y1*rx,z1*rx,'k', X,y1*rx,z2*rx,'k', X,y2*rx,z2*rx,'k', ...
    X,y2*rx,z1*rx,'k', x1*rx,Y,z1*rx,'k', x2*rx,Y,z1*rx,'k',...
    x1*rx,Y,z2*rx,'k', x2*rx,Y,z2*rx,'k', x1*rx,y1*rx,Z,'k',...
    x2*rx,y1*rx,Z,'k', x2*rx,y2*rx,Z,'k', x1*rx,y2*rx,Z,'k', 'linewidth',3)
axis ([x1 x2 y1 y2 z1 kk*(z2-z1)]);
grid off; hold all;
for k = 1:Nbeam
is = zeros(Np,3);
for j = 1:Np
  is(j,:)= Intersectlinesph(po(k,:),[xc(j) yc(j) zc(j) r(j)]);
end
ztouch1 = is(:,3);
% case 1: beam does not hit any particles
if max(ztouch1) == 0
    ispoint = [po(k,1), po(k,2),z1];
    xtouch = linspace(po(k,1),ispoint(1,1));
    ytouch = linspace(po(k,2),ispoint(1,2));
    ztouch = linspace(po(k,3),ispoint(1,3));
    plot3(xtouch,ytouch,ztouch,'r','linewidth',1);

else %caese 2: initial beam hit particles
[maxpt, tpoint] = max(ztouch1);
ispoint = is(tpoint,:);
Pp(tpoint) = Pp(tpoint)+ A*Pb(k); % the particle absorb A*Pb(k) amount of power
Pb(k) = R*Pb(k); % the power of that beam reduces to R*Pb(k)
xtouch = linspace(po(k,1),ispoint(1,1));
ytouch = linspace(po(k,2),ispoint(1,2));
ztouch = linspace(po(k,3),ispoint(1,3));
plot3(xtouch,ytouch,ztouch,'r','linewidth',1);

% beam profile after first reflection:
po(k,:) = Sphereereflect(po(k,1:3), ispoint, [xc(tpoint) yc(tpoint)
zc(tpoint)]);
is = zeros(Np,3);
for j = 1:Np
  is(j,:)= Intersectlinesph(po(k,:),[xc(j) yc(j) zc(j) r(j)]);
end

dist = zeros(length(is(:,1)),1);
for i = 1:length(is(:,1))
    if is(i,:) == [0 0 0]
        dist(i) = 10e4;
    elseif i == tpoint
        dist(i) = 10e4;
    else
        dist(i) = (is(i,1)-po(k,1))^2+(is(i,2)-po(k,2))^2+(is(i,3)-po(k,3))^2;
    end
end


if min(dist) == 10e4 % No hitting after first reflection
   if po(k,6)>0
   dd = (1.5*z2 - po(k,3))/po(k,6);
   elseif po(k,6)==0
   di = max([x2-po(k,1), y2-po(k,2)]);
```

```
   else
   dd = po(k,3)-z1;
   end
   ispoint =[po(k,1)+dd*po(k,4), po(k,2)+dd*po(k,5), po(k,3)+dd*po(k,6)];
   xtouch = linspace(po(k,1),ispoint(1,1));
   ytouch = linspace(po(k,2),ispoint(1,2));
   ztouch = linspace(po(k,3),ispoint(1,3));
%   plot3(xtouch,ytouch,ztouch,'r','linewidth',1);
else
[maxpt, tpoint] = min(dist);
ispoint = [is(tpoint,1) is(tpoint,2) is(tpoint,3)];

Pp(tpoint) = Pp(tpoint)+ A*Pb(k); % the particle absorb A*Pb(k) amount of power
Pb(k) = R*Pb(k); % the power of that beam reduces to R*Pb(k)

dxtouch = ispoint(1,1) - po(k,1);
dytouch = ispoint(1,2) - po(k,2);
dztouch = ispoint(1,3) - po(k,3);
xtouch = linspace(po(k,1),ispoint(1,1));
ytouch = linspace(po(k,2),ispoint(1,2));
ztouch = linspace(po(k,3),ispoint(1,3));
plot3(xtouch,ytouch,ztouch,'r','linewidth',1);

% Beam profile after second reflection:
po(k,:) = Sphereereflect(po(k,1:3), ispoint, [xc(tpoint) yc(tpoint)
zc(tpoint)]);
is = zeros(Np, 3);
for j = 1:Np
  is(j,:)= Intersectlinesph(po(k,:),[xc(j) yc(j) zc(j) r(j)]);
end
dist = zeros(length(is(:,1)),1);
for i = 1:length(is(:,1))
    if is(i,:) == [0 0 0]
        dist(i) = 10e4;
    elseif i == tpoint
        dist(i) = 10e4;
    else
        dist(i) = (is(i,1)-po(k,1))^2+(is(i,2)-po(k,2))^2+(is(i,3)-po(k,3))^2;
    end
end

if min(dist) == 10e4
   if po(k,6)>0
   dd = (1.5*z2 - po(k,3))/po(k,6);
   elseif po(k,6)==0
   di = max([x2-po(k,1), y2-po(k,2)]);
   else
   dd = po(k,3)-z1;
   end
   ispoint =[po(k,1)+dd*po(k,4), po(k,2)+dd*po(k,5), po(k,3)+dd*po(k,6)];
   xtouch = linspace(po(k,1),ispoint(1,1));
   ytouch = linspace(po(k,2),ispoint(1,2));
   ztouch = linspace(po(k,3),ispoint(1,3));
%   plot3(xtouch,ytouch,ztouch,'r','linewidth',1);

else
```

```
[maxpt, tpoint] = min(dist);
ispoint = [is(tpoint,1) is(tpoint,2) is(tpoint,3)];

Pp(tpoint) = Pp(tpoint)+ A*Pb(k); % the particle absorb A*Pb(k) amount of power
Pb(k) = R*Pb(k); % the power of that beam reduces to R*Pb(k)

dxtouch = ispoint(1,1) - po(k,1);
dytouch = ispoint(1,2) - po(k,2);
dztouch = ispoint(1,3) - po(k,3);
xtouch = linspace(po(k,1),ispoint(1,1));
ytouch = linspace(po(k,2),ispoint(1,2));
ztouch = linspace(po(k,3),ispoint(1,3));
plot3(xtouch,ytouch,ztouch,'r','linewidth',1);

% Beam profile after third reflection:
po(k,:) = Sphereereflect(po(k,1:3), ispoint, [xc(tpoint) yc(tpoint)
zc(tpoint)]);
is = zeros(Np, 3);
for j = 1:Np
  is(j,:)= Intersectlinesph(po(k,:),[xc(j) yc(j) zc(j) r(j)]);
end
dist = zeros(length(is(:,1)),1);
for i = 1:length(is(:,1))
    if is(i,:) == [0 0 0]
        dist(i) = 10e4;
    elseif i == tpoint
        dist(i) = 10e4;
    else
        dist(i) = (is(i,1)-po(k,1))^2+(is(i,2)-po(k,2))^2+(is(i,3)-po(k,3))^2;
    end
end

if min(dist) == 10e4
   if po(k,6)>0
   dd = (1.5*z2 - po(k,3))/po(k,6);
   elseif po(k,6)==0
   di = max([x2-po(k,1), y2-po(k,2)]);
   else
   dd = po(k,3)-z1;
   end
   ispoint =[po(k,1)+dd*po(k,4), po(k,2)+dd*po(k,5), po(k,3)+dd*po(k,6)];
   xtouch = linspace(po(k,1),ispoint(1,1));
   ytouch = linspace(po(k,2),ispoint(1,2));
   ztouch = linspace(po(k,3),ispoint(1,3));
%    plot3(xtouch,ytouch,ztouch,'r','linewidth',1);

else
[maxpt, tpoint] = min(dist);
ispoint = [is(tpoint,1) is(tpoint,2) is(tpoint,3)];
Pp(tpoint) = Pp(tpoint)+ A*Pb(k); % the particle absorb A*Pb(k) amount of power
Pb(k) = R*Pb(k); % the power of that beam reduces to R*Pb(k)
dxtouch = ispoint(1,1) - po(k,1);
dytouch = ispoint(1,2) - po(k,2);
dztouch = ispoint(1,3) - po(k,3);
xtouch = linspace(po(k,1),ispoint(1,1));
ytouch = linspace(po(k,2),ispoint(1,2));
```

```
ztouch = linspace(po(k,3),ispoint(1,3));
plot3(xtouch,ytouch,ztouch,'r','linewidth',1);

% Beam profile after fourth reflection:
po(k,:) = Sphereereflect(po(k,1:3), ispoint, [xc(tpoint) yc(tpoint)
zc(tpoint)]);
is = zeros(Np, 3);
for j = 1:Np
  is(j,:)= Intersectlinesph(po(k,:),[xc(j) yc(j) zc(j) r(j)]);
end
dist = zeros(length(is(:,1)),1);
for i = 1:length(is(:,1))
    if is(i,:) == [0 0 0]
        dist(i) = 10e4;
    elseif i == tpoint
        dist(i) = 10e4;
    else
        dist(i) = (is(i,1)-po(k,1))^2+(is(i,2)-po(k,2))^2+(is(i,3)-po(k,3))^2;
    end
end

if min(dist) == 10e4
   if po(k,6)>0
   dd = (1.5*z2 - po(k,3))/po(k,6);
   elseif po(k,6)==0
   di = max([x2-po(k,1), y2-po(k,2)]);
   else
   dd = po(k,3)-z1;
   end
   ispoint =[po(k,1)+dd*po(k,4), po(k,2)+dd*po(k,5), po(k,3)+dd*po(k,6)];
   xtouch = linspace(po(k,1),ispoint(1,1));
   ytouch = linspace(po(k,2),ispoint(1,2));
   ztouch = linspace(po(k,3),ispoint(1,3));
%    plot3(xtouch,ytouch,ztouch,'r','linewidth',1);

else
[maxpt, tpoint] = min(dist);
ispoint = [is(tpoint,1) is(tpoint,2) is(tpoint,3)];

Pp(tpoint) = Pp(tpoint)+ A*Pb(k); % the particle absorb A*Pb(k) amount of power
Pb(k) = R*Pb(k); % the power of that beam reduces to R*Pb(k)

dxtouch = ispoint(1,1) - po(k,1);
dytouch = ispoint(1,2) - po(k,2);
dztouch = ispoint(1,3) - po(k,3);
xtouch = linspace(po(k,1),ispoint(1,1));
ytouch = linspace(po(k,2),ispoint(1,2));
ztouch = linspace(po(k,3),ispoint(1,3));
plot3(xtouch,ytouch,ztouch,'r','linewidth',1);

% Beam profile after fifth reflection:
po(k,:) = Sphereereflect(po(k,1:3), ispoint, [xc(tpoint) yc(tpoint)
zc(tpoint)]);
is = zeros(Np, 3);
for j = 1:Np
  is(j,:)= Intersectlinesph(po(k,:),[xc(j) yc(j) zc(j) r(j)]);
```

```
end
dist = zeros(length(is(:,1)),1);
for i = 1:length(is(:,1))
    if is(i,:) == [0 0 0]
        dist(i) = 10e4;
    elseif i == tpoint
        dist(i) = 10e4;
    else
        dist(i) = (is(i,1)-po(k,1))^2+(is(i,2)-po(k,2))^2+(is(i,3)-po(k,3))^2;
    end
end

if min(dist) == 10e4
   if po(k,6)>0
   dd = (1.5*z2 - po(k,3))/po(k,6);
   elseif po(k,6)==0
   di = max([x2-po(k,1), y2-po(k,2)]);
   else
   dd = po(k,3)-z1;
   end
   ispoint =[po(k,1)+dd*po(k,4), po(k,2)+dd*po(k,5), po(k,3)+dd*po(k,6)];
   xtouch = linspace(po(k,1),ispoint(1,1));
   ytouch = linspace(po(k,2),ispoint(1,2));
   ztouch = linspace(po(k,3),ispoint(1,3));
%    plot3(xtouch,ytouch,ztouch,'r-','linewidth',1);

else
[maxpt, tpoint] = min(dist);
ispoint = [is(tpoint,1) is(tpoint,2) is(tpoint,3)];

Pp(tpoint) = Pp(tpoint)+ A*Pb(k); % the particle absorb A*Pb(k) amount of power
Pb(k) = R*Pb(k); % the power of that beam reduces to R*Pb(k)

dxtouch = ispoint(1,1) - po(k,1);
dytouch = ispoint(1,2) - po(k,2);
dztouch = ispoint(1,3) - po(k,3);
xtouch = linspace(po(k,1),ispoint(1,1));
ytouch = linspace(po(k,2),ispoint(1,2));
ztouch = linspace(po(k,3),ispoint(1,3));
plot3(xtouch,ytouch,ztouch,'r-','linewidth',1);
end
end
end
end
end
end
end

% Plot particles
for c = 1:Np
    sphere_mesh = surf(Xs(:,:,c),Ys(:,:,c),Zs(:,:,c));
    set(sphere_mesh,'FaceColor',[0 1 0],'FaceAlpha',1,'EdgeAlpha',0.03);
end
```

```
print(figure4,'-djpeg','-
r300',['SLS_3DSim_withBeam_',num2str(Np),'_p_',datestr(now,'mm-dd-yyyy-HH-MM-
AM'),'.jpg']);
Ep = Pp*tlaser; %Energy absorbed by each powder
Ppowder = sum(Pp); % total power absorbed by the powders
Etotal = Ppowder*tlaser; % Total energy absorbed by the powders
eff = Ppowder/Po;
Pbeam = sum(Pb);   % total power scattered out of the powders
Pd = (4/3)*pi*sum(r.^3)/((x2-x1)*(y2-y1)*(z2-z1)); %Packing density of powders
mp = rho_si*(4/3)*pi*r.^3*1e-15;
T = To + Ep./(Csi*mp);
Epulse = Ep;
Emelt = Csi*mp*(1414-To);
dsqr = zeros(Np,Np);
Acc = zeros(Np,Np);
peri = zeros(Np,Np);
Acontact = zeros(Np,Np);
hcontact = zeros(Np,Np);

for i = 1:Np
   for j = 1:Np
      dsqr(i,j) = ((xc(i)-xc(j))^2 + (yc(i)-yc(j))^2 + (zc(i)-zc(j))^2)^0.5;
      peri(i,j) = 0.5*(r(i)+r(j)+dsqr);
       if i~=j && dsqr(i,j)<rc(i)+rc(j)
         Acc(i,j) = (peri*(peri-r(i))*(peri-r(j))*(peri-dsqr(i,j)))^0.5;
         hcontact(i,j) = 2*Acc(i,j)/dsqr(i,j);
         Acontact(i,j) = pi*hcontact(i,j)^2;
       else
          Acontact(i,j) = 0;
       end
   end
end

tcon = 0:0.01:1;
tdd = 0.01;
Ntt = length(tcon);
Kcon = 120;
for nt = 1:Ntt
   for i=1:Np
      for j = 1:Np
         if Acontact(i,j)~=0
           T(i) = Kcon*Acontact(i,j)*(T(j)-T(i))*tdd/(m(i)*Csi)+T(i);
         end
      end
   end
end

% Plot of particles in different energy level
figure5 = figure (5);
set(figure5,'Position',[500,500,1000,700]);
plot3(X,y1*rx,z1*rx,'k', X,y1*rx,z2*rx,'k', X,y2*rx,z2*rx,'k', ...
   X,y2*rx,z1*rx,'k', x1*rx,Y,z1*rx,'k', x2*rx,Y,z1*rx,'k',...
   x1*rx,Y,z2*rx,'k', x2*rx,Y,z2*rx,'k', x1*rx,y1*rx,Z,'k',...
   x2*rx,y1*rx,Z,'k', x2*rx,y2*rx,Z,'k', x1*rx,y2*rx,Z,'k', 'linewidth',3)
axis ([x1 x2 y1 y2 z1 kk*(z2-z1)]);
grid on; hold all;
```

```
for c = 1:Np
    if T(c)>= Tmelt
    sphere_mesh = surf(Xs(:,:,c),Ys(:,:,c),Zs(:,:,c));
    set(sphere_mesh,'FaceColor',[1 0 0],'FaceAlpha',1,'EdgeAlpha',0.03);

    %elseif T(c) < Tmelt & T(c)>= 0.5*Tmelt
    %sphere_mesh = surf(Xs(:,:,c),Ys(:,:,c),Zs(:,:,c));
    %set(sphere_mesh,'FaceColor',[1 1 0],'FaceAlpha',0.5,'EdgeAlpha',0.03);

    else
    sphere_mesh = surf(Xs(:,:,c),Ys(:,:,c),Zs(:,:,c));
    set(sphere_mesh,'FaceColor',[0 1 0],'FaceAlpha',0.1,'EdgeAlpha',0.03);
    end
end
print(figure5,'-djpeg','-
r300',['SLS_3DSim_Elevel_',num2str(Np),'_p_',datestr(now,'mm-dd-yyyy-HH-MM-
AM'),'.jpg']);
%}
%--------------------------------------------------------------------------

%--------------------------------------------------------------------------
% Plot energy distribution versus X,Y,Z-axis and plane.
figure6 = figure (6)
marker_size = 3;
set(figure6,'Position',[500,500,1000,700]);
subplot(2,2,1)
plot(xc,Epulse,'ro','markerfacecolor','r', 'markersize',marker_size);
hold on; grid on;
plot(xc, Emelt,'b-','markerfacecolor','b','markersize',marker_size);
xlabel('X(um)'); ylabel('Energy (J)');
legend('Energy of particles','Energy sufficient to melt particles')

subplot(2,2,2)
plot(yc,Epulse,'ro','markerfacecolor','r', 'markersize',marker_size)
hold on; grid on;
plot(yc, Emelt,'b-','markerfacecolor','b','markersize',marker_size);
xlabel('Y(um)'); ylabel('Energy (J)');
legend('Energy of particles','Energy sufficient to melt particles')


subplot(2,2,3)
plot(zc,Epulse,'ro','markerfacecolor','r', 'markersize',marker_size)
hold on; grid on;
plot(zc, Emelt,'b-','markerfacecolor','b','markersize',marker_size);
xlabel('Z(um)'); ylabel('Energy (J)');
legend('Energy of particles','Energy sufficient to melt particles')

subplot(2,2,4)
plot3(xc,yc,Epulse,'ro','markerfacecolor','r','markersize',marker_size);
hold on; grid on;
plot3(xc,yc,Emelt,'b-','markerfacecolor','b','markersize',marker_size);
xlabel('X(um)'); ylabel('Y(um)'); zlabel('Energy (J)');
legend('Energy of particles','Energy sufficient to melt particles')
print(figure2,'-djpeg','-
r300',['SLS_3DSim_Exyz_',num2str(Np),'_p_',datestr(now,'mm-dd-yyyy-HH-MM-
AM'),'.jpg']);
```

```
%}
```

## SLS_3D_Fun.m

```
function dRp = SLS_3D_Fun( t, rp, rcenter,xcc,ycc,zcc )
global Ec x1 x2 y1 y2 z1 z2 rho_si grav

x = rp(1);
y = rp(2);
z = rp(3);
dx = rp(4);
dy = rp(5);
dz = rp(6);
r = rcenter(end); % radius of particle i
rc = rcenter;
ni = length(rc);
D = zeros(1,ni-1);
R = D;
d = R;
m = rho_si*4/3*pi*r^3;

for j=1:ni-1
   % Distance between any two particles
   D(j)= ((x-xcc(j))^2+(y-ycc(j))^2+(z-zcc(j))^2)^0.5;
   % Equivalent radius between i and j particle
   R(j)= r*rc(j)/(r+rc(j));
   % normal displacement by contact force
   d(j)= abs(D(j)-r-rc(j));
end

% Contact force
Fcx = 0;
Fcy = 0;
Fcz = 0;
alpha = 1e8;
for j=1:ni-1
    if D(j)<r+rc(j)
    Fcx = Fcx+alpha*(D(j)-(r+rc(j)))/(r+rc(j))*(xcc(j)-x)/D(j);
    Fcy = Fcy+alpha*(D(j)-(r+rc(j)))/(r+rc(j))*(ycc(j)-y)/D(j);
    Fcz = Fcz+alpha*(D(j)-(r+rc(j)))/(r+rc(j))*(zcc(j)-z)/D(j);
    end
end

cwall = 100;
if x-r<=x1
  Fcx = Fcx+cwall*alpha*(x1+r-x)/r;
end
if x+r>=x2
  Fcx = Fcx+cwall*alpha*(x2-x-r)/r;
end

if y-r<=y1
  Fcy = Fcy+cwall*alpha*(y1+r-y)/r;
end
if y+r>=y2
  Fcy = Fcy+cwall*alpha*(y2-y-r)/r;
```

```
end

if z-r<=z1
  Fcz = Fcz+cwall*alpha*(z1+r-z)/r;
end
if z+r>=z2
  Fcz = Fcz+cwall*alpha*(z2-z-r)/r;
end

% Friction Force
us = 1; % friction coefficient
nx = zeros(Np,Np);
ny = nx; nz = nx;
Ffx = zeros(1,Np);
Ffy = zeros(1,Np);
Ffz = zeros(1,Np);
for i=1:Np
   for j = 1:Np
      if i==j
          Ffx(i)=Ffx(i);
          Ffy(i)=Ffy(i);
          Ffz(i)=Ffz(i);
      else
          if D(i,j)<=rc(i)+rc(j)
    nx(i,j)= (x(j)-x(i))/sqrt((x(j)-x(i))^2+(y(j)-y(i))^2+(z(j)-z(i))^2);
    ny(i,j)= (y(j)-y(i))/sqrt((x(j)-x(i))^2+(y(j)-y(i))^2+(z(j)-z(i))^2);
    nz(i,j)= (z(j)-z(i))/sqrt((x(j)-x(i))^2+(y(j)-y(i))^2+(z(j)-z(i))^2);
    n = [nx(i,j);ny(i,j);nz(i,j)];
    vi = [dx(i);dy(i);dz(i)];
    vj = [dx(j);dy(j);dz(j)];
    vti = vi-dot(vi,n)*n;
    vtj = vj-dot(vj,-n)*-n;
    tij = (vtj-vti)/sqrt(sum((vti-vtj).^2));
    Ffx(i) = Ffx(i)+us*Fcx(i)*tij(1);
    Ffy(i) = Ffy(i)+us*Fcy(i)*tij(2);
    Ffz(i) = Ffz(i)+us*Fcz(i)*tij(3);
          end
      end
   end
end

Ffx = 0;
Ffy = 0;
Ffz = 0;

% Environmental damping force
Cdamp = 3; %Damping coefficient
Fex = -Cdamp*dx*m;
Fey = -Cdamp*dy*m;
Fez = -Cdamp*dz*m;
% Gravitational force
Fgz = -grav*m;
xdot = dx;
ydot = dy;
zdot = dz;
dxdot= 1/m*(Fcx+Fex+Ffx);
```

```
dydot= 1/m*(Fcy+Fey+Ffy);
dzdot= 1/m*(Fcz+Fez+Ffz+Fgz);
dRp = [xdot,ydot,zdot,dxdot,dydot,dzdot]';
% disp(['time:',num2str(t),'seconds']);
end
```

## Intersectlinesph.m

```
function point = Intersectlinesph(line, sphere, varargin)
%   Return intersection points between a line vector and a sphere
%   Direction of the line matters, line doesn't go [-dx -dy -dz)] direction
%   GC = intersectLineSphere(LINE, SPHERE);
%   Returns the two points which are the intersection of the given line and
%   sphere.
%   LINE   : [x0 y0 z0  dx dy dz]
%   SPHERE : [xc yc zc  R]
%   GC     : [x1 y1 z1 ; x2 y2 z2]

% check if user-defined tolerance is given
tol = 1e-14;
if ~isempty(varargin)
   tol = varargin{1};
end
%convert to unit directional vector
K = (line(4)^2+line(5)^2+line(6)^2)^0.5;
line(4) = line(4)/K;
line(5) = line(5)/K;
line(6) = line(6)/K;
% difference between centers
dc = line(1:3) - sphere(1:3);
% equation coefficients
a = sum(line(:, 4:6) .* line(:, 4:6), 2);
b = 2*sum(dc.*line(4:6), 2);
c = sum(dc.*dc, 2) - sphere(:,4).*sphere(:,4);
% solve equation
delta = b.*b - 4*a.*c;

if delta > tol
   % delta positive: find two roots of second order equation
   u1 = (-b -sqrt(delta)) / 2 / a;
   u2 = (-b +sqrt(delta)) / 2 / a;
   if u1 <0 % in case the beam goes the opposite direction of the initial one
      point = zeros(1,3);
   else
   % convert into 3D coordinate
   %point = [line(1:3)+u1*line(4:6) ; line(1:3)+u2*line(4:6)];
   point = [line(1:3)+u1*line(4:6)]; %return only the nearer intersection point
   end
elseif abs(delta) < tol
   % delta around zero: find unique root, and convert to 3D coord.
   u = -b/2./a;
   if u <0 % in case the beam goes the oppositve directioin of the inital one
      point = zeros(1,3);
   else
   point = line(1:3) + u*line(4:6);
   end
else
   % delta negative: no solution
   point = zeros(1, 3); % Set large number for "point" if not existing
end
```

## Sphereреflect.m

```
function reflectionpoint = Sphereреflect(startpt, interpt, center)
% input: startpt = starting point coordinates, interpt = intersection point
% coordinates: [x y z]
% return dpoint = [ x y z dx dy dz]

uv = startpt - interpt;
rv = interpt - center;
dpoint = 2*dot(uv,rv)*rv - uv;
reflectionpoint = [interpt, dpoint];
end
```

# Appendix – B. Matlab Code for Porosity Estimation

```
clc; clear; close all;
% INPUTS
A=imread('image04.jpg');
Resolution=2.5; % micron/pixel of the image
Nc=30; %Number of pore size categories

%Porosity size and deviation
A=im2bw(A,graythresh(A));
Conn=8;
[s1,s2]=size(A);
A=bwmorph(A,'majority',10);
Poro=sum(sum(~A))/(s1*s2);
D=-bwdist(A,'cityblock');
B=medfilt2(D,[3 3]);
B=watershed(B,Conn);
Pr=zeros(s1,s2);

for I=1:s1
    for J=1:s2
        if A(I,J)==0 && B(I,J)~=0
            Pr(I,J)=1;
        end
    end
end
Pr=bwareaopen(Pr,9,Conn);
[Pr_L,Pr_n]=bwlabel(Pr,Conn);
V=zeros(Pr_n,1);
for I=1:s1
    for J=1:s2
        if Pr_L(I,J)~=0
            V(Pr_L(I,J))=V(Pr_L(I,J))+1;
        end
    end
end
R=Resolution.*(V./pi).^.5; % Pore radius

% Porosity Percentage
Pr_L = bwlabel(Pr_L);
Pr_L = imcomplement(Pr_L);
whitepix = 0;
blackpix = 0;
for j = 1:s2
    for i = 1:s1
        if Pr_L(i,j) == 1
            whitepix = whitepix + 1;
        else
            blackpix = blackpix + 1;
        end
    end
end
totalpix = whitepix + blackpix;
porosity = 100*blackpix/totalpix
```

```
%Outputs
poremean = mean(R)
porestd = std(R)
figure('units','normalized','outerposition',[0 0 1 1])
subplot(1,2,1)
imshow(Pr_L)
imwrite(Pr_L,'Output.png')
subplot(1,2,2)
Rel_Frequencies=hist(R,[1:round(max(R)/Nc):round(max(R))])./sum(sum(hist(R,[1:r
ound(max(R)/Nc):round(max(R))])));
bar([1:round(max(R)/Nc):round(max(R))],Rel_Frequencies);
xlabel('Pore Size (micron)');
ylabel('Relative Frequency');
axis([1 max(R) 0 max(Rel_Frequencies)]);
axis square;
annotation('textbox',[.7 .7 .1 .1], 'String', ['Porosity = ' num2str(porosity)
'%'])
annotation('textbox',[.7 .65 .1 .1], 'String', ['Average Pore Size = '
num2str(poremean) ' micron' ])
```

# Appendix – C. Numerical Solution of Particle Balling

## Main.m

```
close all; clear all; clc;
global a b P R
st = 0.732; % Surface Tension N/m
grav = 9.81; % gravity
den_si = 2329; %density of Silicon
R = 1e-3;
a = sqrt(st/(den_si*grav));
b = R;
P = 2*a/b;
%initial condition
thetaspan = [0 pi];
xzo = [0.01*R 0.01*R];

[theta,XZ] = ode45(@SphereMeltFun,thetaspan,xzo);
rms = a*XZ(:,1);
zms = -a*(XZ(:,2)- max(XZ(:,2)));
rang = 0:0.05:2*pi;
xm = R*cos(rang);
ym = R*sin(rang)+R;

nms = length(rms);
phi = 0:2*pi/(nms-1):2*pi;

[RMS, PHI] = meshgrid(rms,phi);
XMS = RMS.*cos(PHI);
YMS = RMS.*sin(PHI);
ZMS = meshgrid(zms);

[ang1,ang2] = meshgrid(linspace(0,pi,30),linspace(0,2*pi,30));
xrs = R*sin(ang1).*cos(ang2);
yrs = R*sin(ang1).*sin(ang2);
zrs = R*cos(ang1);

%2D plot of liguid sphere
figure(1)
plot(xm,ym,'r--','linewidth',3)
hold on;
plot(rms,zms,'linewidth',2);
plot(-rms,zms,'linewidth',2);
xlabel('x(m)');
ylabel('z(m)');
axis tight;

%3D plot of liquid sphere
figure(2)
grid ON; hold on;
droplet_after = surf(XMS,YMS,ZMS);
set(droplet_after,'FaceColor',[0 0 1],'FaceAlpha',1,'EdgeAlpha',0.05);
```

```
axis tight; grid on;
```

**Function.m**

```
function dP = SphereMeltFun(theta, xz)
global a b P R
x = xz(1);
z = xz(2);
dx = x*cos(theta)/(x*z+x*P-sin(theta));
dz = x*sin(theta)/(x*z+x*P-sin(theta));
dP = [dx; dz];
end
```

# Bibliography


[1] Jiang, L. and Cheung, R., 2009. A review of silicon carbide development in MEMS applications. *International Journal of Computational Materials Science and Surface Engineering*, *2*(3-4), pp.227-242.

[2] Zorman, C.A. and Parro, R.J., 2008. Micro-and nanomechanical structures for silicon carbide MEMS and NEMS. *physica status solidi (b)*, *245*(7), pp.1404-1424.

[3] Inoue, K., Nippon Pillar Packing Co. Ltd. and Nippon Steel Corporation, 2000. *Semiconductor wafer holder with CVD silicon carbide film coating*. U.S. Patent 6,135,054.

[4] Cheung, R., 2006. *Silicon carbide microelectromechanical systems for harsh environments*. World Scientific.

[5] Kingery, W.D., Bowen, H.K. and Uhlmann, D.R., Introduction to ceramics, 1976. *Jhon Willey & Sons, New York*.

[6] Rice, P.M., Kingery, W.D., Bowen, H.K., Uhlmann, D.R., Onoda, G.Y., Hench, L.L., Wachtman, J.B., Cannon, W.R. and Matthewson, M.J., 1997. Physical ceramics: principles for ceramic science and engineering.

[7] Philipp, H.R. and Taft, E.A., 1960. Silicon Carbide—A High Temperature Semiconductor.

[8] Harris, G.L. ed., 1995. *Properties of silicon carbide* (No. 13). Iet.

[9] Biedermann, E., 1965. The optical absorption bands and their anisotropy in the various modifications of SiC. *Solid State Communications*, *3*(10), pp.343-346.

[10] Choyke, W.J., Hamilton, D.R. and Patrick, L., 1964. Optical properties of cubic SiC: luminescence of nitrogen-exciton complexes, and interband absorption. *Physical Review*, *133*(4A), p.A1163.

[11] Solangi, A. and Chaudhry, M.I., 1992. Absorption coefficient of β–SiC grown by chemical vapor deposition. *Journal of materials research*, *7*(3), pp.539-541.

[12] Nishino, S., Matsunami, H. and Tanaka, T., 1978. Growth and morphology of 6H-SiC epitaxial layers by CVD. *Journal of Crystal Growth*, *45*, pp.144-149.

[13] Baumann, H.N., 1952. The relationship of alpha and beta silicon carbide. *Journal of The Electrochemical Society*, *99*(3), pp.109-114.

[14] Ruff, O., 1935. The formation and dissociation of silicon carbide. *Transactions of The Electrochemical Society*, *68*(1), pp.87-109.

[15] Casady, J.B. and Johnson, R.W., 1996. Status of silicon carbide (SiC) as a wide-bandgap semiconductor for high-temperature applications: A review. *Solid-State Electronics*, *39*(10), pp.1409-1422.

[16] Greskovich, C. and Rosolowski, J.H., 1976. Sintering of covalent solids. *Journal of the American Ceramic Society*, *59*(7-8), pp.336-343.

[17] Billington, S.R., Chown, J. and White, A.E.S., 1964. The sintering of silicon carbide. *Special Ceramics*, pp.19-34.

[18] Coble, R.L., 1961. Sintering crystalline solids. I. Intermediate and final state diffusion models. *Journal of applied physics*, *32*(5), pp.787-792.

[19] Clearfield, A., 1961. Inorganic Chem., 3 (1964) 146. RL Coble. *J. Appl. Phys*, *32*, p.787.

[20] Kingery, W.D. and Berg, M., 1955. Study of the initial stages of sintering solids by viscous flow, evaporation-condensation, and self-diffusion. *Journal of Applied Physics*, *26*(10), pp.1205-1212.

[21] Wilder, D.R. and Fitzsimmons, E.S., 1955. Further study of sintering phenomena. *Journal of the American Ceramic Society*, *38*(2), pp.66-71.

[22] Coble, R.L. and Cannon, R.M., 1978. Current paradigms in powder processing. In *Processing of Crystalline Ceramics* (pp. 151-170). Springer US.

[23] German, R.M., 1996. Sintering theory and practice. *Solar-Terrestrial Physics (Solnechno-zemnaya fizika)*, p.568.

[24] Meyers, M.A. and Olevsky, E.A., 1997. Sintering Theory and Practice. *Journal of Materials Engineering and Performance*, *6*(3), p.278.

[25] Hansen, J.D., Rusin, R.P., Teng, M.H. and Johnson, D.L., 1992. Combined-Stage Sintering Model. *Journal of the American Ceramic Society*, *75*(5), pp.1129-1135.

[26] Hansen, J.D., Rusin, R.P., Teng, M.H. and Johnson, D.L., 1992. Combined-Stage Sintering Model. *Journal of the American Ceramic Society*, *75*(5), pp.1129-1135.

[27] Kraft, T. and Riedel, H., 2004. Numerical simulation of solid state sintering; model and application. *Journal of the European Ceramic Society*, *24*(2), pp.345-361.

[28] Rahaman, M.N., 2007. *Sintering of ceramics*. CRC press.

[29] German, R.M., 2013. *Liquid phase sintering*. Springer Science & Business Media.

[30] Weiss, J. and Kaysser, W.A., 1983. Liquid phase sintering. In *Progress in nitrogen ceramics* (pp. 169-186). Springer Netherlands.

[31] Kingery, W.D., 1959. Densification during sintering in the presence of a liquid phase. I. Theory. *Journal of Applied Physics*, *30*(3), pp.301-306.

[32] PROCHAZKA, S. and SCANLAN, R.M., 1975. Effect of boron and carbon on sintering of SiC. *Journal of the American Ceramic Society*, *58*(1-2), pp.72-72.

[33] Stobierski, L. and Gubernat, A., 2003. Sintering of silicon carbideI. Effect of carbon. *Ceramics international*, *29*(3), pp.287-292.

[34] Stobierski, L. and Gubernat, A., 2003. Sintering of silicon carbide II. Effect of boron. *Ceramics international*, *29*(4), pp.355-361.

[35] Rijswijk, W.V. and Shanefield, D.J., 1990. Effects of carbon as a sintering aid in silicon carbide. *Journal of the American Ceramic Society*, *73*(1), pp.148-149.

[36] PROCHAZKA, S. and SCANLAN, R.M., 1975. Effect of boron and carbon on sintering of SiC. *Journal of the American Ceramic Society*, *58*(1-2), pp.72-72.

[37] Noviyanto, A. and Yoon, D.H., 2013. Metal oxide additives for the sintering of silicon carbide: Reactivity and densification. *Current Applied Physics*, *13*(1), pp.287-292.

[38] Perevislov, S.N., 2013. Mechanism of liquid-phase sintering of silicon carbide and nitride with oxide activating additives. *Glass and ceramics*, *70*(7-8), pp.265-268.

[39] Zhang, B.R., Marino, F. and Ferraris, M., 1994. Liquid-phase hot-pressing and WC-particle reinforcement of SiC-Si composites. *Journal of the European Ceramic Society*, *14*(6), pp.549-555.

[40] Lee, J.S., Lee, S.H., Nishimura, T., Hirosaki, N. and Tanaka, H., 2009. A ternary compound additive for vacuum densification of β-silicon carbide at low temperature. *Journal of the European Ceramic Society*, *29*(16), pp.3419-3423.

[41] Datta, M.S., Bandyopadhyay, A.K. and Chaudhuri, B., 2002. Sintering of nano crystalline α silicon carbide by doping with boron carbide. *Bulletin of Materials Science*, *25*(3), pp.181-189.

[42] She, J.H. and Ueno, K., 1999. Effect of additive content on liquid-phase sintering on silicon carbide ceramics. *Materials Research Bulletin*, *34*(10), pp.1629-1636.

[43] Omori, M. and Takei, H., 1982. Pressureless sintering of SiC. *Journal of the American Ceramic Society*, *65*(6).

[44] Lee, S.P., Shin, Y.S., Bae, D.S., Min, B.H., Park, J.S. and Kohyama, A., 2006. Fabrication of liquid phase sintered SiC materials and their characterization. *Fusion engineering and design*, *81*(8), pp.963-967.

[45] Lin, B., 1986. HOT-PRESSING OF@-SIC POWDER WITH AL-B-C ADDITIVES. *J. AM. CERAM. SOC. J. Am. Ceram. Soc.*, *69*(4).

[46] Zhou, Y., Tanaka, H., Otani, S. and Bando, Y., 1999. Low-Temperature Pressureless Sintering of alpha-SiC with Al4C3-B4C-C Additions. *Journal of the American Ceramic Society*, *82*(8), pp.1959-1964.

[47] Lee, S.G., Shim, W.H., Kim, J.Y., Kim, Y.W. and Kwon, W.T., 2001. Effect of sintering-additive composition on fracture toughness of liquid-phase-sintered SiC ceramics. *Journal of materials science letters*, *20*(2), pp.143-146.

[48] Yonathan, P., Lee, J.H., Yoon, D.H., Kim, W.J. and Park, J.Y., 2009. Improvement of SiC f/SiC density by slurry infiltration and tape stacking. *Materials Research Bulletin*, *44*(11), pp.2116-2122.

[49] Huang, Z.H., Jia, D.C., Zhou, Y. and Liu, Y.G., 2003. A new sintering additive for silicon carbide ceramic. *Ceramics International*, *29*(1), pp.13-17.

[50] Yang, H., Zhang, L., Guo, X., Zhu, X. and Fu, X., 2011. Pressureless sintering of silicon carbide ceramics containing zirconium diboride. *Ceramics International*, *37*(6), pp.2031-2035.

[51] Sacks, M.D., Bozkurt, N. and Scheiffele, G.W., 1991. Fabrication of mullite and mullite-matrix composites by transient viscous sintering of composite powders. *Journal of the American Ceramic Society*, *74*(10), pp.2428-2437.

[52] Kumar, S., Kumar, A., Devi, R., Shukla, A. and Gupta, A.K., 2009. Capillary infiltration studies of liquids into 3D-stitched C–C preforms: Part B: Kinetics of silicon infiltration. *Journal of the European Ceramic Society*, *29*(12), pp.2651-2657.

[53] Messner, R.P. and Chiang, Y.M., 1990. Liquid-Phase Reaction-Bonding of Silicon Carbide Using Alloyed Silicon-Molybdenum Melts. *Journal of the American Ceramic Society*, *73*(5), pp.1193-1200.

[54] Gern, F.H. and Kochendörfer, R., 1997. Liquid silicon infiltration: description of infiltration dynamics and silicon carbide formation. *Composites Part A: Applied Science and Manufacturing*, *28*(4), pp.355-364.

[55] Evans, R.S., Bourell, D.L., Beaman, J.J. and Campbell, M.I., 2003. Reaction bonded silicon carbide: SFF, process refinement and applications. In *14th Solid Freeform Fabrication Symposium*(pp. 414-22).

[56] Deckard, C.R., Board of Regents and System, 1989. *Method and apparatus for producing parts by selective sintering*. U.S. Patent 4,863,538.

[57] Beaman, J.J. and Deckard, C.R., Board of Regents and System, 1990. *Selective laser sintering with assisted powder handling*. U.S. Patent 4,938,816.

[58] Deckard, C.R., Beaman, J.J. and Darrah, J.F., Deckard Carl R, Beaman Joseph J and Darrah James F, 1992. *Method for selective laser sintering with layerwise cross-scanning*. U.S. Patent 5,155,324.

[59] Nelson, J.C., Vail, N.K., Barlow, J.W., Beaman, J.J., Bourell, D.L. and Marcus, H.L., 1995. Selective laser sintering of polymer-coated silicon carbide powders. *Industrial & engineering chemistry research*, *34*(5), pp.1641-1651.

[60] Evans, R.S., Bourell, D.L., Beaman, J.J. and Campbell, M.I., 2005. Rapid manufacturing of silicon carbide composites. *Rapid Prototyping Journal*, *11*(1), pp.37-40.

[61] Evans, R.S., Bourell, D.L., Beaman, J.J. and Campbell, M.I., 2003. Reaction bonded silicon carbide: SFF, process refinement and applications. In *14th Solid Freeform Fabrication Symposium*(pp. 414-22).

[62] Stevinson, B.Y., Bourell, D.L. and Beaman, J.J., 2006. *Support Free Infiltration of Selective Laser Sintered (SLS) Silicon Carbide Preforms* (Doctoral dissertation, University of Texas at Austin).

[63] Stevinson, B., Bourell, D.L. and Beaman, J.J., 2008. Over-infiltration mechanisms in selective laser sintered Si/SiC preforms. *Rapid Prototyping Journal*, *14*(3), pp.149-154.

[64] Stierlen, P. and Eyerer, P., 1999. SilSiC.. Cerantic Prototypes via LS21.. Process (Liquid SiliconInfiltration of LaserSintered C.. SiC Parts).

[65] Meyers, S., Kruth, J.P. and Vleugels, J., 2015, January. Direct Selective Laser Sintering of Reaction Bonded Silicon Carbide. In *Solid Freeform Farbication Symposium Proceedings* (pp. 1750-1758).

[66] Exner, H., Horn, M., Streek, A., Ullmann, F., Hartwig, L., Regenfuß, P. and Ebert, R., 2008. Laser micro sintering: A new method to generate metal and ceramic parts of high resolution with sub-micrometer powder. *Virtual and physical prototyping*, *3*(1), pp.3-11.

[67] Regenfuss, P., Streek, A., Hartwig, L., Klötzer, S., Brabant, T., Horn, M., Ebert, R. and Exner, H., 2007. Principles of laser micro sintering. *Rapid Prototyping Journal*, *13*(4), pp.204-212.

[68] Kruth, J.P., Wang, X., Laoui, T. and Froyen, L., 2003. Lasers and materials in selective laser sintering. *Assembly Automation*, *23*(4), pp.357-371.

[69] Tolochko, N.K., Khlopkov, Y.V., Mozzharov, S.E., Ignatiev, M.B., Laoui, T. and Titov, V.I., 2000. Absorptance of powder materials suitable for laser sintering. *Rapid Prototyping Journal*, *6*(3), pp.155-161.

[70] Streek, A., Regenfuss, P., Ullmann, F., Hartwig, L., Ebert, R., Exner, H. and Laserapplikationszentrum, F.M., 2006. Processing of silicon carbide by laser micro sintering. In *The Proceedings of the 17th Annual SFF Symposium* (Vol. 349).

[71] Kruth, J.P., Mercelis, P., Van Vaerenbergh, J., Froyen, L. and Rombouts, M., 2005. Binding mechanisms in selective laser sintering and selective laser melting. *Rapid prototyping journal*, *11*(1), pp.26-36.

[72] Margiotta, J.C., Zhang, D., Nagle, D.C. and Feeser, C.E., 2008. Formation of dense silicon carbide by liquid silicon infiltration of carbon with engineered structure. *Journal of Materials Research*, *23*(5), pp.1237-1248.

[73] Chiang, Y.M., Messner, R.P., Terwilliger, C.D. and Behrendt, D.R., 1991. Reaction-formed silicon carbide. *Materials Science and Engineering: A*, *144*(1-2), pp.63-74.

[74] Messner, R.P. and Chiang, Y.M., 1990. Liquid-Phase Reaction-Bonding of Silicon Carbide Using Alloyed Silicon-Molybdenum Melts. *Journal of the American Ceramic Society*, *73*(5), pp.1193-1200.

[75] Zhou, H. and Singh, R.N., 1995. Kinetics model for the growth of silicon carbide by the reaction of liquid silicon with carbon. *Journal of the American Ceramic Society*, *78*(9), pp.2456-2462.

[76] Favre, A., Fuzellier, H. and Suptil, J., 2003. An original way to investigate the siliconizing of carbon materials. *Ceramics International*, *29*(3), pp.235-243.

[77] Margiotta, J.C., Zhang, D. and Nagle, D.C., 2010. Microstructural evolution during silicon carbide (SiC) formation by liquid silicon infiltration using optical microscopy. *International Journal of Refractory Metals and Hard Materials*, *28*(2), pp.191-197.

[78] Dezellus, O., Jacques, S., Hodaj, F. and Eustathopoulos, N., 2005. Wetting and infiltration of carbon by liquid silicon. *Journal of materials science*, *40*(9-10), pp.2307-2311.

[79] Fang, H.T., Jeon, J.H., Zhu, J.C. and Yin, Z.D., 2002. Inhibition of liquid Si infiltration into carbon–carbon composites by the addition of Al to the Si slurry pre-coating: mechanism analysis. *Carbon*, *40*(14), pp.2559-2565.

[80] Gern, F.H. and Kochendörfer, R., 1997. Liquid silicon infiltration: description of infiltration dynamics and silicon carbide formation. *Composites Part A: Applied Science and Manufacturing*, *28*(4), pp.355-364.

[81] Einset, E.O., 1998. Analysis of reactive melt infiltration in the processing of ceramics and ceramic composites. *Chemical Engineering Science*, *53*(5), pp.1027-1039.

[82] Bashforth, F. and Adams, J.C., 1883. *An attempt to test the theories of capillary action*. University Press.

[83] Millot, F., Sarou-Kanian, V., Rifflet, J.C. and Vinet, B., 2008. The surface tension of liquid silicon at high temperature. *Materials Science and Engineering: A*, *495*(1), pp.8-13.

[84] Shishkin, A.V. and Basin, A.S., 2004. Surface tension of liquid silicon. *Theoretical Foundations of Chemical Engineering*, *38*(6), pp.660-668.

[85] Kolossov, S., Boillat, E., Glardon, R., Fischer, P. and Locher, M., 2004. 3D FE simulation for temperature evolution in the selective laser sintering process. *International Journal of Machine Tools and Manufacture*, *44*(2), pp.117-123.

[86] Marcu, T., Todea, M., Gligor, I., Berce, P. and Popa, C., 2012. Effect of surface conditioning on the flowability of Ti6Al7Nb powder for selective laser melting applications. *Applied Surface Science*, *258*(7), pp.3276-3282.

# Vita

Nanzhu Zhao was born in Yanji, China. He enrolled in the Mechanical Engineering program at the Brigham Young University in Provo, Utah in Spring 2007, receiving the Bachelor of Science degree in Spring 2011. He enrolled in the Mechanical Engineering Graduate program at the University of Texas at Austin in the Fall 2011 and received a Master's degree in 2013. This dissertation was typed by the author.

Permanent email address: znz@utexas.edu